2020

Realization of the true 3D printing using multi directional wire and arc additive manufacturing

Lei Yuan
University of Wollongong

Realization of the true 3D printing using multi-directional wire and arc additive manufacturing

Lei Yuan

Supervisors:
Prof Zengxi Pan
Prof Weihua Li
Prof Donghong Ding

This thesis is presented as part of the requirement for the conferral of the degree:

Doctor of philosophy

University of Wollongong

School of Mechanical, Materials, Mechatronics and Biomedical Engineering

Faculty of Engineering and Information Sciences

November, 2020

Abstract

Robotic wire and arc based additive manufacturing has been used in fabricating of metallic parts owing to its advantages of lower capital investment, higher deposition rates, and better material properties. Although many achievements have been made, the build direction of Wire Arc Additive Manufacturing (WAAM) is still limited in the vertical-up direction, resulting in extra supporting structure usage while fabricating metallic parts with overhanging features. Thus, the current WAAM technology should be also called 2.5D printing rather than 3D printing. In order to simplify the deposition set-up and increase the flexibility of the WAAM process, it is necessary to find an alternative approach for the deposition of 'overhangs' in a true 3D space. This dissertation attempts to realize true 3D printing by developing a novel multi-directional WAAM system using robotic Gas Metal Arc Welding (GMAW) to additively manufacture metal components in multiple directions. Several key steps including process development, welding defect investigation and avoidance, and robot path generation are presented in this study.

The research was the first attempt to develop a fabrication method of producing metallic parts with overhanging structures using the multi-directional wire arc additive manufacturing. Firstly, based on the metal droplet kinetics and weld bead geometry, two different Gas Metal Arc Welding (GMAW) metal transfer modes, namely short circuit transfer and free flight transfer, were evaluated for the multi-directional wire arc additive manufacturing.

Subsequently, the effects of process parameters, including wire feed speed (WFS), torch travel speed (TS), nozzle to work distance (NTWD) and torch angle, on the stability of positional deposition were investigated. Finally, the effectiveness of the proposed strategy was verified by fabricating three complex samples with overhangs.

Moreover, the dimensional quality of the overhanging parts may however deteriorate due to the humping effect, which appears as a series of periodic beadlike protuberances on the weld deposits. There has been significant research on the humping phenomenon in the downhand welding, but it is doubtful whether the existing theories of humping formation can be applied in the positional deposition during WAAM process. This study has therefore provided an experimental work to investigate the formation of the humping phenomena in the positional deposition during additive manufacturing with the gas metal arc welding. Firstly, the mechanism of humping formation was analysed to explain humping occurrence for positional deposition. Then, the mechanism was validated through experiments with different welding parameters and positions. Finally, a series of guidelines are summarised to assist the path planning and process parameter selection processes in multi-directional WAAM.

The widespread adoption of multi-directional WAAM is yet to occur, primarily due to the complexity of the programming process. In this work, we present a robot path planning algorithm which can automatically plan the complete multi-directional WAAM process. Compared to a common WAAM process which only deposits parts along the fixed vertical-up direction layer upon layer, the programming process becomes more complicated due to the following two reasons. (i) Most existing WAAM system plans torch trajectories based on CAD model and assuming robot/machine can always reach those trajectories, which is true when part size is not huge and the welding torch is always kept down hand. However, the collision-free robot motion for multiple torch orientations usually includes searching for an optimal reachable solution from multiple robot configurations, which is new in the WAAM research field. (ii) The deposition sequence is no longer from the bottom to the top as the overhanging structure can be built at different stage of the manufacturing. The optimization of weld sequence plays a critical role to avoid collision between the torch and partially deposited component. The proposed algorithmic system consists of four key modules relating to a) robot motion planning, b) initial collision processing, c) layer sequence optimization, and d) weld torch pose adjustment. In the first stage, the required robot motions to deposit each layer of the part is obtained through an automated robot offline programming (AOLP) engine. From these robot motions, a collision matrix C is generated to guide later steps of the planning process. After this, layer sequence optimization is performed to eliminate identified collision between the robot system and the part. If collision still exists, adjustments to the torch pose are made to avoid the remaining collision.

Finally, a process planning algorithm for the multi-directional WAAM based positional process is developed. The proposed multi-directional WAAM process would therefore significantly reduce the manufacturing time and cost.

Acknowledgments

This thesis was written at the University of Wollongong, under the main supervision of Prof. Zengxi Pan. Thus, First and foremost, I would like to express my sincere appreciation Prof. Zengxi Pan who helps start my research and guides me during all my study at the University of Wollongong.

Many thanks to my associate supervisor Prof. Weihua Li, he helped we award scholarship from china scholarship council (CSC), which keeps free of financial worries and provided the much needed assistance in my master and PhD studies. I would also like to Prof. Huijun Li who gives me valuable recommendations and suggestions to advance my research progress.

I would like to express my warmest thanks to Prof. Donghong Ding who gives me a lot of meaningful discussion of my project and help to finish my thesis. He shared a lot research experiences with me and give me valuable comments through completing this thesis.

Thanks to Prof. Stephen van Duin, Joseph Polden and other colleges and students in UOW. The assistance they provided in my studies over the last four years is the key factor for the successful completion of this work,

Finally, I wish to express my special thanks to my father, to my mother, and to my girlfriend Dr. Doan for their support and encouragement during the hard time of my life. I can not have the

achievement without them.

Certification

I, Lei Yuan, declare that this thesis submitted in fulfilment of the requirements for the conferral of the degree Doctor of philosophy, from the University of Wollongong, is wholly my own work unless otherwise referenced or acknowledged. This document has not been submitted for qualifications at any other academic institution.

Lei Yuan

Date (21st November 2020)

List of names or abbreviations

AM	additive manufacturing
AOLP	automated offline programming
BD	build direction
CAD	computer-aided design
CCD	charge coupled device
CM	collision matrix
CMT	cold metal transfer
CMT-P	cold metal transfer- pulse
CMT-ADV	cold metal transfer- advanced
C-Space	Cartesian Space
CO_2	carbon dioxide
CTWD	contact to work distance
DoF	Degree of Freedom
GTAW	gas tungsten arc welding
GMAW	gas metal arc welding

HI	heat input
MIG	metal inert gas
NTWD	Nozzle to work distance
STL	Standard Template Library
TIG	tungsten inert gas
TS	Travel speed
TSMPD	Task-Space Motion Planning Decomposition
T-Space	task space
UOW	University of Wollongong
WAAM	Wire Arc Additive Manufacturing
WFS	wire feed speed
3D	3-dimensional

Table of contents

List of figures

Chapter 1

Chapter 2

Chapter 3

Chapter 4

Chapter 5

Chapter 6

List of tables

Chapter 2

Chapter 3

Chapter 4

Chapter 5

Chapter 6

Chapter 1

Introduction

1.1 Background

Additive manufacturing, also known 3D printing [1], has been developing for more than 30 years since the first attempt to fabricate polymer as communication or inspection tools in 1980s [2]. ASTM standards define additive manufacturing (AM) as the "process of joining materials to make objects from 3D model data, usually layer upon layer, as opposed to subtractive manufacturing methodologies" [3]. In Wohlers's report, they predicted that the market value would be growing up to 6.5 billion US dollars, especially the applications of creating models and prototyping [4]. Recently, the focus of AM has changed to fabricate expensive metal components such as titanium [5] and nickel alloys [6] in the aerospace industry where such components often suffer an extremely high buy-to-fly ratio [7].

Many applications have been carried out for fabricating metallic component in AM, including directed energy deposition, powder bead fusion, sheet lamination and binder jetting [8]. The typical consumables are metal powder and metal wire. Thus, the AM technology can be also classified as either powder or wire supplied process [9]. In practices, the AM process using powder is employed to fabricate small components with a high geometrical accuracy requirement [10], while the wire-feed technology is normally used to produce large size parts with a relatively rough surface and thereby a post-machining process is necessary. However, the higher efficiency and lower material cost make wire-feed technology more cost-competitive than power-feed process in practical industrial environment. Regarding to the different energy sources used to melt raw metal material, wire-feed AM process is categorized as three types: weld arc based, laser based and electron beam based [11]. Among them, the wire and arc based AM (WAAM), which uses the weld process including Gas Metal Arc Welding (GMAW) or Gas Tungsten Arc Welding (GTAW), becomes a more promising technology due to its higher efficiency (the deposition rate of WAAM is 50–130 g/min, compared to 2–10 g/min for laser or electron beam deposition [12]), lower cost and the capability to manufacturing medium to large-scale components [13].

Robotics based Wire Arc Additive Manufacturing (WAAM) process has drawn interests from both research and industry in recent years. Fig.1.1 shows the number of publications with the keywords “wire arc additive manufacturing”, searched in article titles, abstracts or keywords in Scopus, considering all documents published since 2010. It can be seen a dramatic increase of pubilications on WAAM process. The WAAM is a rapid manufacturing process that firstly slices the input 3D model into a set of 2.5D layer models along the vertical direction, and then builds up the model by depositing materials layer-by-layer from the bottom to the top [14]. However, the monotonous vertical-up fabrication paradigm makes it impossible to deposit parts with overhanging features beyond the overhang angle thresholds [15]. Supports or scaffolds are normally required to print parts with geometrical overhanging features, resulting in an increased cost due to extra post-removal process and lower material utilization rate [16, 17]. For example, As shown in Fig.1.2, to produce a part with an 'overhang' structure (in red), a temporary support structure (in yellow) would be required if being deposited in the fixed vertical up direction, resulting in the deposition of extra material, and the additional cost of a post-machining process to remove it.

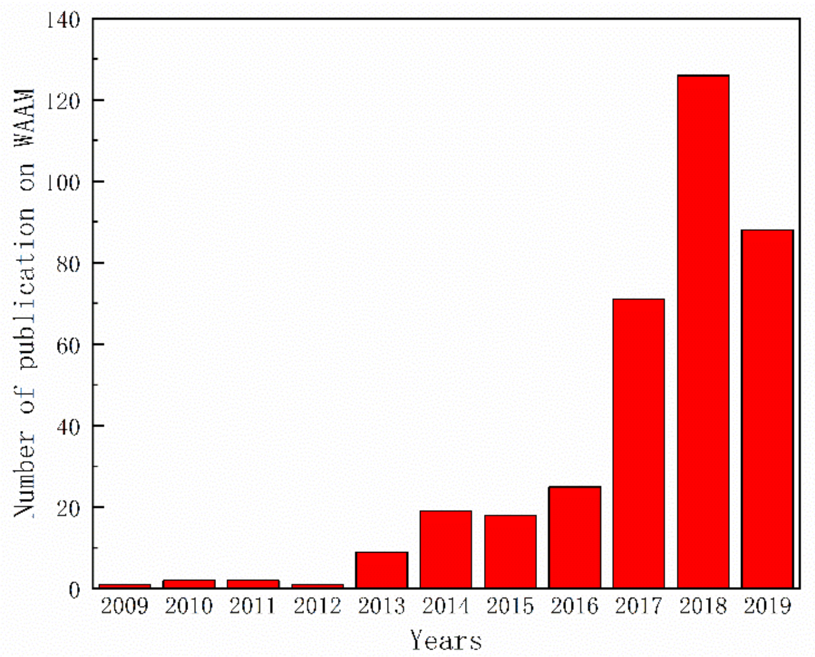

Fig.1. 1 WAAM publications per year

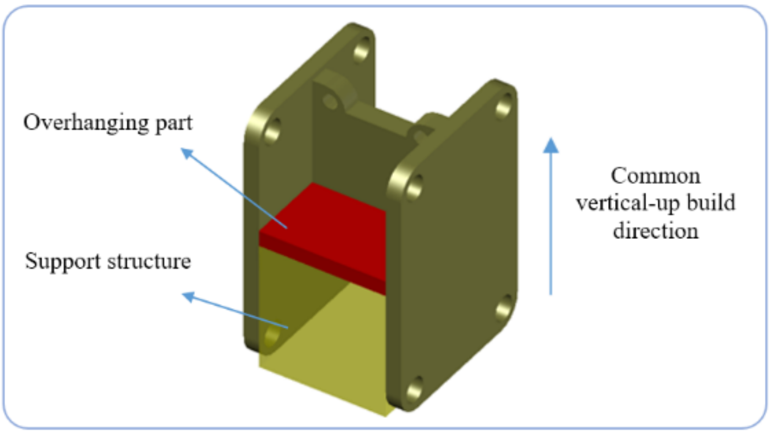

Fig.1. 2 A part with overhangs (in red) and its support for conventional vertical-up deposition

Multi-directional Additive Manufacturing, or Multi-orientational Additive Manufacturing, has the potential to build up overhangs without extra support to improve the efficiency of the AM process. Yang, et al. [18] describes in the multi-directional additive manufacturing system, a deposition nozzle is mounted on a multi-axis actuator, such as the Computer Numerical Control (CNC) machine or the industrial robot, to deposit materials in multiple directions. This positional variant of the process has been developed for various materials over the past 20 years. Polymers were initially studied for multi-orientational deposition due to their low density and large surface tension force. Yang, et al. [18] presented a new deposition method to minimise or avoid the use of support structure. Compared to the maximum inclined angle of 45° reported in previous studies, the proposed method was claimed to be able to deposit plastics in an arbitrary direction. It was also shown that the surface quality of the parts and the efficiency of the AM process were greatly improved. In a study by Singh and Dutta [19], the authors reported that polymers based AM has the ability to deposit part along multiple directions to improve the surface quality and reduce the support usage. An algorithm was developed first to determine how much of a part should be deposited in a particular direction. By employing the method, a few parts were successfully fabricated to demonstrate the effectiveness of the new multi-directional AM system. In addition, Allen and Dutta [20] proposed a wall thickness control strategy for producing the thin-walled polymer parts. The proposed method enables manufacturers to build up objects with less support material and overall manufacturing time.

In terms of WAAM process, taking advantages of positional welding, which means welding at any positions, the overhangs can be deposited using the inherent overhang capability of the weld-bead. Although it is possible to fabricate overhanging parts along any direction, a comprehensive WAAM based positional deposition study has yet to be developed for a practical additive manufacturing system.

1.2 Objective of current research

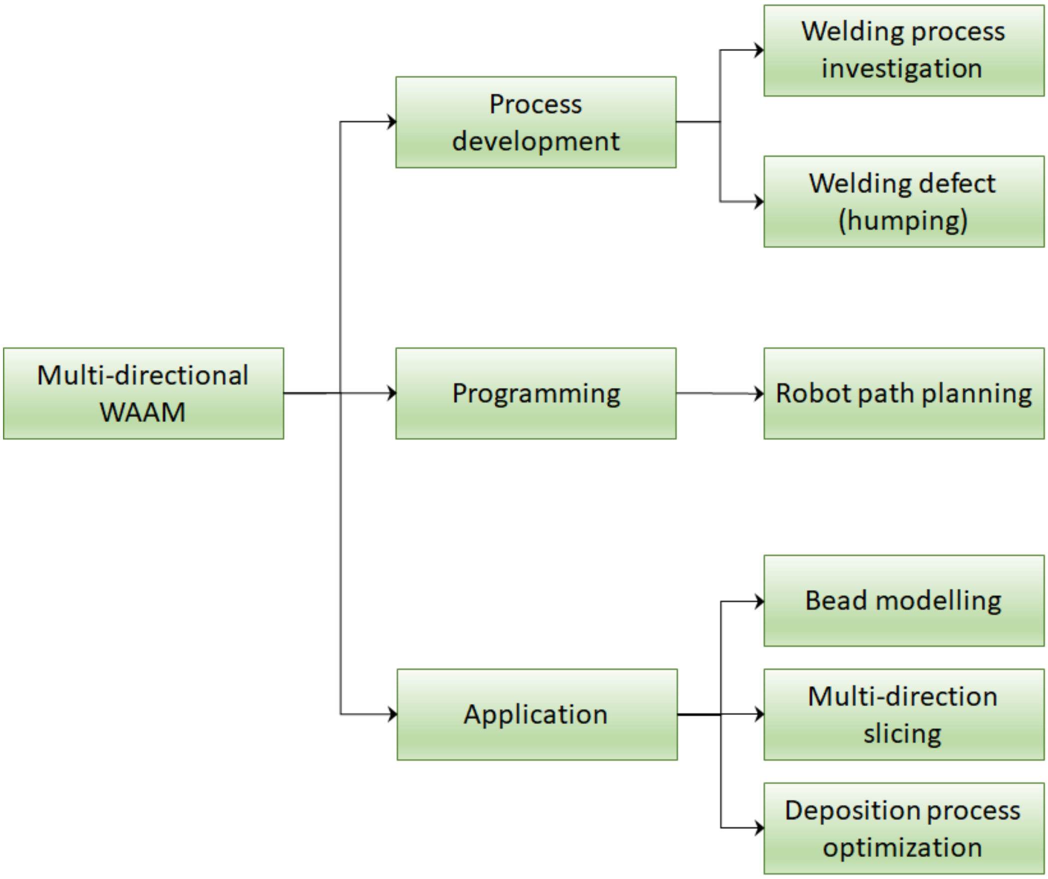

Fig.1. 3 Scope of this study

This study aims to realize a true 3D printing by developing a GMAW-based robotic multi-directional WAAM system which can deposit parts along multiple directions in the 3D space.

To develop the multi-directional WAAM process, process development, programming, and application development for practical use are the three major challenges. As shown in Fig.1.3, lack of investigation on any of these three aspects will result in a practically useless system. While under the influence of the gravitational force, it is difficult to deposit weld bead with an acceptable geometry, the molten metal may sag before solidification, an elaborate process optimization strategy is helpful for forming weld beads with good geometries. Secondly, the robot path planning is more difficult due to (i) the orientation of the torch angle does not only remain vertically, the variations of the torch angle increase the difficulty of the programming. (ii) the layer deposition sequence is not fixed. It needs to be optimized to reduce the complexity of the programming process. Finally, a practical software package is expected to be developed The research objectives completed in this thesis are listed below.

1) Review current literature on WAAM process to identify the research gap between common deposition strategy and the proposed multi-directional WAAM strategy.

2) Obtaining a process optimization strategy. One of the critical requirements for GMAW-based multi-directional WAAM process optimize the deposition process for a better geometry quality of deposits. Due to the downflow of liquid metal under unfavorable force of gravity [23]. In this step, the metal transfer and molten pool formation behavior are analyzed first and the effects of various process parameters on the stability of positional deposition are investigated.

3) Analysing welding defects in positional deposition. The geometrical quality of the overhanging parts may however deteriorate due to a humping effect, which appears as a series of periodic beadlike protuberances on the weld deposits. The current study has therefore investigated the formation of the humping phenomena in the positional

deposition during additive manufacturing with the gas metal arc process. A new inclined metal-flow based model is proposed to explain humping occurrence. Based on experimental studies, the model was validated by using different process parameters and welding positions.

4) Programming. Compared to the traditional WAAM process, the programming work becomes more complicated for the multidirectional WAAM. In this study, a new algorithm is developed to obtain a set of 2.5D layers through a multi-direction slicing method. Then, A complete path planning algorithm is developed for the multi-directional WAAM process, which enables the novel manufacturing technology to be widely adopted for practical industrial use.

5) Verification of the performance of the proposed system. To test the effectiveness of the proposed strategy, several sample parts with different overhanging features are fabricated in each chapter.

1.3 Outline of thesis

This thesis is organized as follows:

Chapter 1 identifies the issue of current WAAM process and initially introduces the conception of true 3D printing using WAAM. Then, the objectives of this study is presented. Followed by chapter 1, the rest of this thesis is divided into 6 sections.

Chapter 2 reviews the development of current WAAM process to identify the research gap. Next, the identified gaps between current WAAM and multi-directional WAAM are investigated through each sub-section.

Chapter 3 explores the positional deposition process for developing the multi-directional process. Different GMAW transfer modes were evaluated based on the metal droplet kinetic and the weld bead geometry and effects of process parameters on bead formation and process stability were quantitatively investigated.

Chapter 4 investigates the humping phenomenon during multi-layer multi-directional WAAM using GMAW/CMT welding. The mechanism of humping phenomenon was analysed for welding in the horizontal position. The proposed humping mechanism was validated for welding different process parameters in different positions. Several guidelines were proposed in order to avoid humping for the multi-layer multi-directional WAAM process.

Chapter 5 develops a complete path planning algorithm for the multi-directional WAAM process, which enables the novel manufacturing technology to be widely adopted for practical industrial use.

Chapter 6 presents a process planning algorithm including bead modelling, multi-direction slicing and process optimization, for multi-directional WAAM based positional process.

Chapter 7 concludes the proposed true 3D printing, namely multi-directional WAAM process of this study and makes recommendations for the future work.

1.4 Original research contributions

The main contributions of the dissertation are threefold.

1) The concept of true 3D is firstly carried to increase the flexibility and reduce the cost of current WAAM process.

2) The positional deposition process is initially investigated in this study. A series of guides are summarized to help form a good appearance of the weld bead in the off-position deposition.

3) For practical industrial use, a process planning algorithm is developed including a few essential modules. Based on the algorithm, a software package is programmed for fabricating parts with complex geometries. The case studies show a good performance of the proposed system.

Chapter 2

Literature review

WAAM technology have been developed for a decade, many researchers have spent effort on how to optimize the WAAM process. In this chapter, current literature regarding how to realize true 3D printing using WAAM process were reviewed. Firstly, the general knowledge of WAAM was provided. Secondly, the current statues of fabricating parts with overhanging features are reviewed and discussed. Then, based on the current WAAM process, a few steps are identified to be challenging for developing multi-directional WAAM process. Those key steps including process development and optimization, welding defect investigation and avoidance, and robot path planning were reviewed subsequently. Finally, a discussion was given on developing the multi-directional WAAM process and the specific tasks of this work.

2.1 Wire arc additive manufacturing (WAAM) process

Among many AM applications that are used to fabricate metallic component, WAAM, a directed energy deposition method, is normally employed to produce parts with medium to large scale due to its high efficiency (the deposition rate of WAAM is 50–130 g/min, compared to 2–10 g/min for laser or electron beam deposition [12]), lower cost and the capability to manufacturing medium to large-scale components [13]. Depending on the nature of the heat source, there are commonly three types of WAAM processes: Gas Metal Arc Welding (GMAW)-based[21], Gas Tungsten Arc Welding (GTAW)-based[22] and Plasma Arc Welding (PAW)-based[23]. Fig.2.1 illustrates a schematic diagram of GMAW (a), GTAW (b) and PAW (c) [8]. As shown in Fig.2.1(a), in GMAW process, the electric arc is formed between a consumable welding wire, which is normally perpendicular to the base metal, and the substrate. The basic metal transfer modes of GMAW can be classified into free flight and short-circuiting [24]. Free flight transfer can be further divided into Spray, Globular and Repelled modes. In addition, cold metal transfer (CMT), a variant of short-circuiting transfer has been carried out for depositing parts with a high depostion rate and low heat input. On the other hand, in both GTAW and PAW processes, the electric arc is formed between a non-consumable tungsten electrode and the substrate. The wire feed angle can be adjusted which has a significant impact on the weld quality.

The features of three WAAM power sources are different, for example, the deposition rate of GMAW process 2-3 times higher than that of GTAW and PAW processes. However, in GMAW process, the GMAW-based WAAM is less stable and generates more weld fume and spatter due to the electric current acting directly on the feedstock [25]. Besides, the part surface quality of the GMAW-based process is relatively low which a post machining process is normally required. Thus, the different WAAM methods have significant on the final products, the choice of WAAM method largely depends on the specific task requirements.

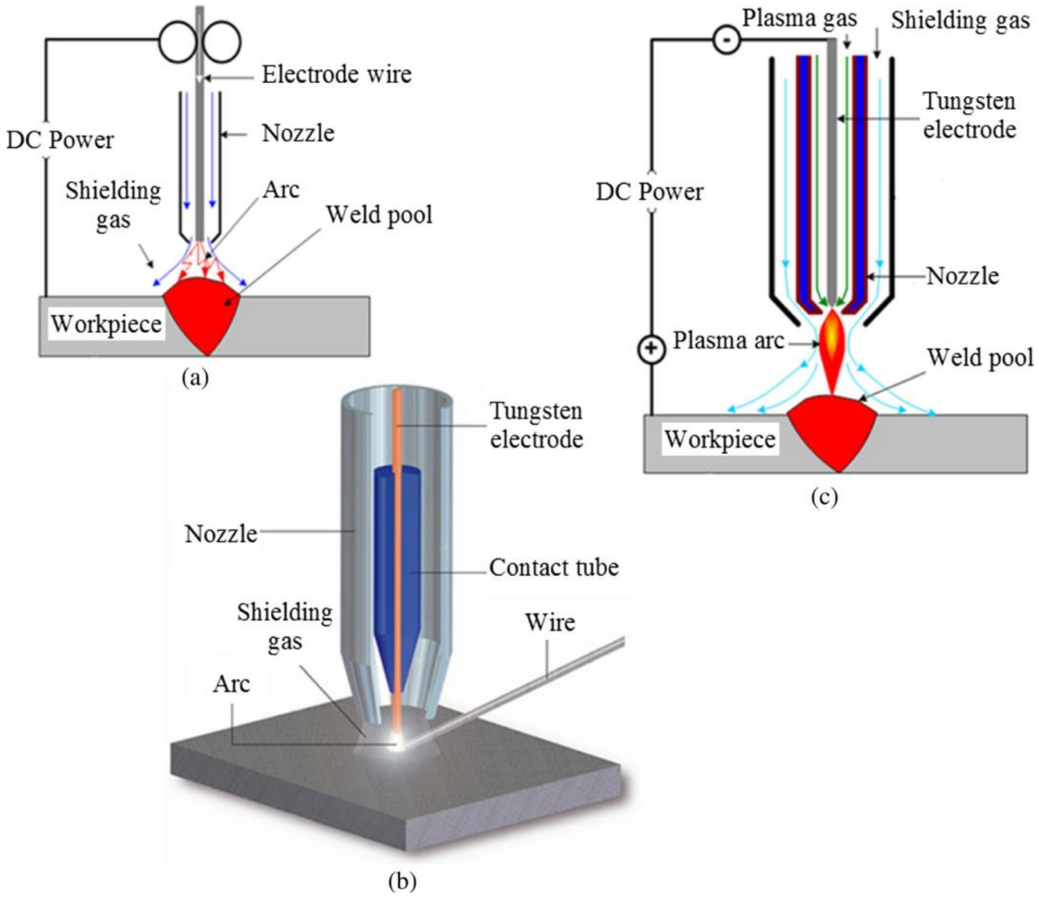

Fig.2. 1 The schematic diagram of (a) GMAW, (b) GTAW, and (c) PAW [8]

2.2 Current research work on fabricating overhanging structure

To improve the efficiency of the WAAM process, many strategies are proposed to reduce the usage of supports, various strategies have been developed for metallic additive manufacturing (AM) process. Some researchers explored multi-direction deposition through integrating extra rotations into the AM system. Fig.2.2 describes the concept of a multi-axis AM deposition system [26]. The overhanging features could be eliminated through suitably orienting the part during the deposition process, and therefore support structures are unnecessary. Ding, et al. [27] developed an 8-axis robotized AM system combining a 6-axis robot arm and an external 2-axis tilt and a rotatory positioning system. With the aid of additional 2-axis rotation system, the reported algorithm optimizes the multi-directional deposition process and its production time was reduced significantly. In the study of Panchagnula and Simhambhatla [28], an additional rotation table was employed to tilt the substrate at an angle equals to the angle from the growth direction of thin-walled parts. The results showed a better geometry quality and more stable deposition process were achieved.

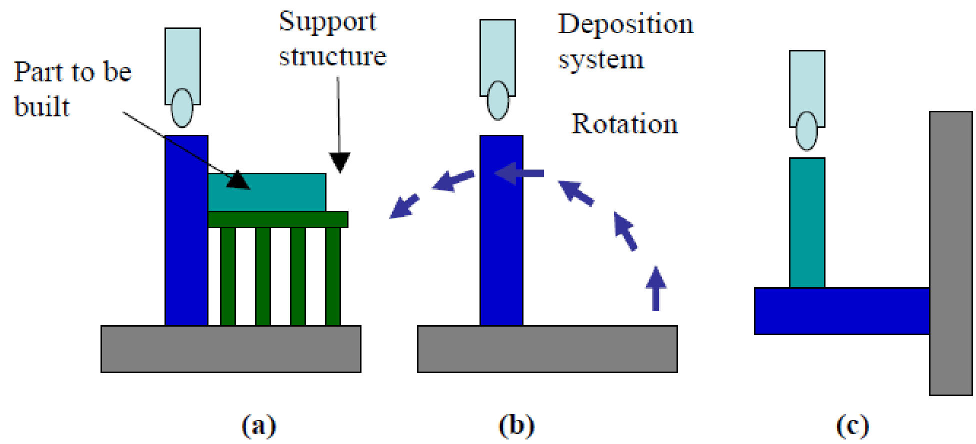

Fig.2. 2 (a) Build part with support structure; (b) The table was rotated; (c) Continue to build the component along another direction [26].

In addition, multi-direction slicing of a CAD model is another challenge associated with the use of rotational table approach. Ding, et al. [29] developed a new decomposition-regrouping method for multi-direction slicing. After decomposing the CAD model into sub-volumes, a depth-tree structure based on topology information is introduced to regroup them into new orders for slicing. In addition, the proposed method is proven to simple and efficient on various tests parts with large number of holes. More existing multi-direction slicing methods can be found in Ruan, et al. [30] (Centroid Axis Extraction Method), Yang, et al. [18] (Transition WallMethod), and Dwivedi and Kovacevic [31] (Skeleton Method), etc.

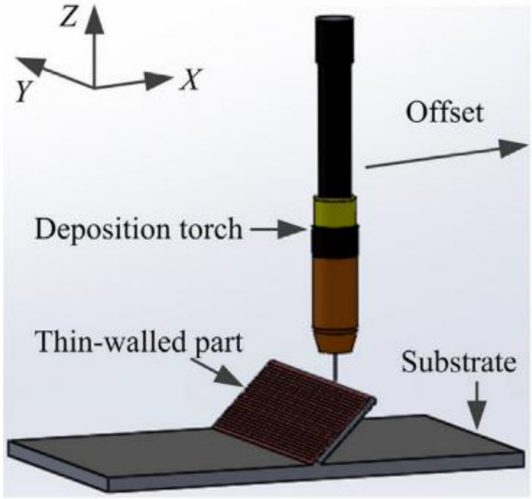

Fig.2. 3 Demonstration of fabricating parts with inclined angle in flat position [32].

Instead of using a positioner to adjust the orientation of the object, some researchers focus on fabrication of overhangs with inclined features directly in a flat position, as shown in Fig.2.3. GMAW-based welding process is considered as a mature process which can be done in any direction or orientation with proper control, because the surface tension force is able to bear the weight of the weld bead. This inherent overhanging ability of weld-deposition beads is used to produce small overhangs easily in WAAM process [28]. Xiong, et al. [32] studied the influence of process parameters on the formation of the inclined wall in a GWAM-based WAAM process. In the experiment, the influences of offset distance, wire feed speed, and welding torch travel speed on the inclination angle were examined and discussed. The experimental results showed that the higher travel speed and the lower wire feed speed benefited a larger inclination angle. The maximum inclination angle was extended to be more than 45˚with proper weld settings. In the research of Li, et al. [33], a mathematical model of the inclined multi-layer multi-bead parts is initially established for GWAM-based WAAM process. Additionally, the authors mentioned that the material shortage areas are found at the edges of the parts with inclined features and thereby extra material should be deposited to form a better parts geometry. However, although several advancements have been made, the inclination angle of the overhangs is still limited to a small range.

To deposit overhanging structure at arbitrary direction without extra rotational mechanical system, Kazanas, et al. [34] reported a feasibility study of fabrication of overhanging structure directly without supports using WAAM process. The authors explained that taking advantages of positional welding, which means weld at any positions, the overhangs can be deposited directly in WAAM process. In the experiment, a few horizontal and inclined walls were deposited, and several process control strategies were presented. Although the capability of WAAM process to deposit at any direction was primarily testified, a comprehensive WAAM based positional deposition system has yet to be developed in a practical additive manufacturing system.

2.3 Challenges in multi-directional WAAM

A common WAAM process aims at fabricating defect-free metallic parts defect-free fabrication with high geometrical accuracy [7, 35, 36]. Fig.2.4 illustrates architecture of a common WAAM process from CAD model to the final near-net product [29]. It consists of several essential modules including 2.5D slicing, bead modelling, 2D path planning, welding process setups, robot code generation, and post-machining process.

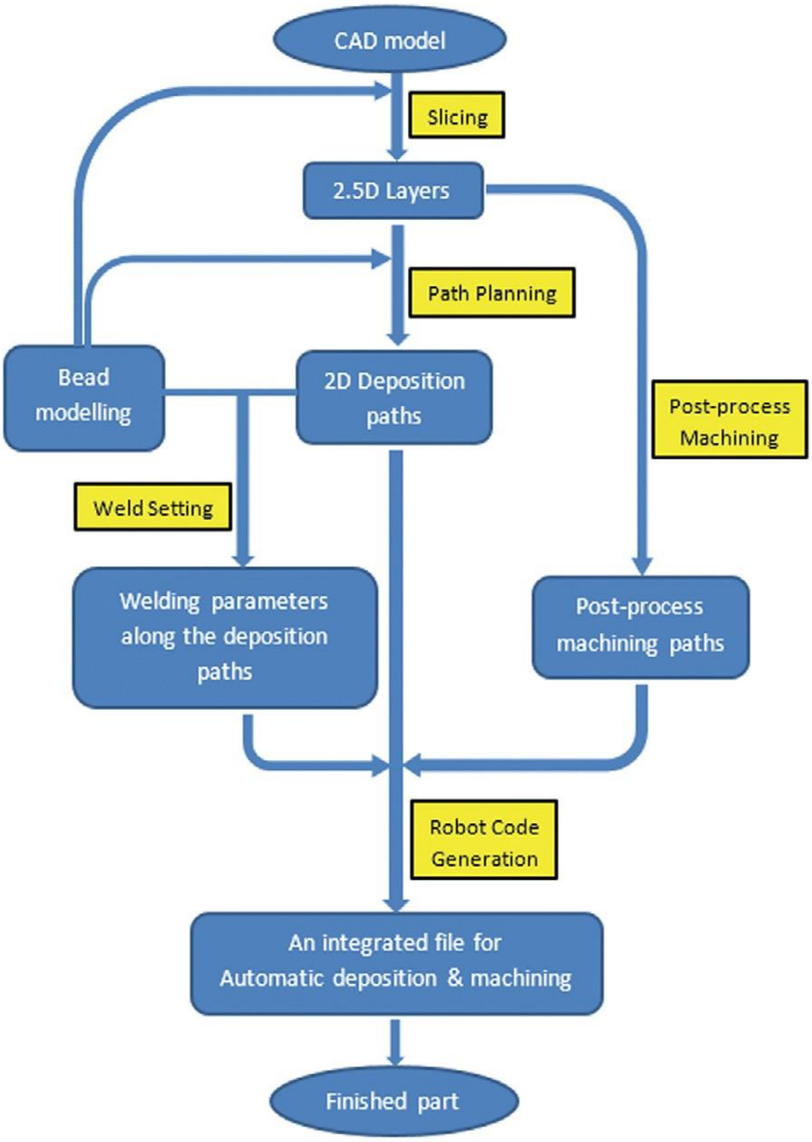

Fig.2. 4 The general process of WAAM

- Welding process control. In terms of positional deposition, the first issue coming with positional welding is the sagged weld bead. In conventional WAAM process, the deposition is always conducted in the downhand position. Thus, weld bead is always regular as long as the process parameters are selected in the welding parameter range. However, the story is totally different in positional deposition. Due to the impact of gravitational force, the molten pool may sag excessively when welding with improper parameters, this results in a poor bead profile. To enhance the appearance of the weld bead, it is necessary to identify the proper welding parameters to control deposition process for the multi-directional WAAM. Thus, the most important step of constructing a multi-directional WAAM process is to develop a welding process control strategy for a stable deposition process and acceptable bead profiles.

- 2D slicing. Currently, the 3D CAD model is sliced into a set of 2.5Dlayer with one or a group of predetermined values for layer thickness along the build orientation, which is the vertical-up direction in most of cases [37, 38]. However, to fabricate parts with geometrical features in WAAM process, the supporting structure is usually required to deposit overhangs when using the monotonous vertical-up slicing strategy. Once the overhanging structure can be deposited in multiple directions, a key step in multi-directional WAAM process is to develop a robust algorithm to identify the overhangs and slicing the 3D model along multiple directions. Currently, many multi-direction slicing strategies have been proposed. In this study, the multi-direction slicing strategy reported in [29] is developed for fabricating complex structures. The slicing method firstly decomposes 3D model into a set of optimal sub-volumes and then generate sliced layers along the most suitable deposition directions of the sub-volumes.

- Robot code generation. Path planning in robotic welding originally concerned the problems of moving welding torch along the predetermined weld trajectory without any clash. Hence, the collision avoidance is a fundamental issue when programming robot motion for welding tasks. Compared to common WAAM process which only deposit parts along the fixed vertical-up direction, the programming process becomes more complicated due to the following two reasons. (i)Most existing WAAM systems plan torch trajectories based on the part CAD model and assuming robot/machine can always reach those trajectories, which is true when part size is not large and the welding torch is always kept down hand. However, the collision-free robot motion for multiple torch orientations, which usually includes searching for an optimal reachable solution from multiple robot configurations, is new to the WAAM research field. (ii) The deposition sequence is no longer from the bottom to the top as the overhanging structure can be built at different stages of the manufacturing. The optimisation of weld sequence plays a critical role to avoid collision between the torch and partially deposited component.

- 2D path planning and post machining. Path planning module generates the paths to fill up the 2D layers representing the cross-sectional geometry by controlling the motion the welding torch [39]. In multi directional WAAM, the 3D model is sliced into sets of 2.5D layers along multiple directions rather than single vertical-up direction in current WAAM process. As listed in Table 2.1, Many 2D path planning algorithms, raster [40], zig-zag [41, 42], Spiral [43, 44], Continuous [39, 45-47], Contour [48-50], hybrid [37, 51], medial axis transformation (MAT) [36], can be applied to the proposed multi-directional WAAM process directly. In addition, post machining process is used to remove the unnecessary volume and improve the surface quality of the parts. In this study, these two modules will be also integrated into the proposed system, although the 2D path planning and post-machining strategy is not the scope of this study.

Table 2. 1 The current path planning strategies.

Path planning pattern	Literature	Illustration
Raster	[40]	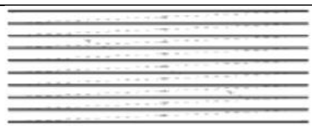
Zig-zag	[41, 42]	
Spiral	[43, 44]	
Continuous	[39, 45-47]	
Contour	[48-50]	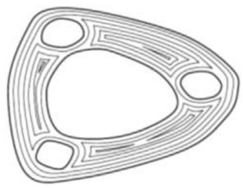
Hybrid	[37, 51]	
MAT	[36]	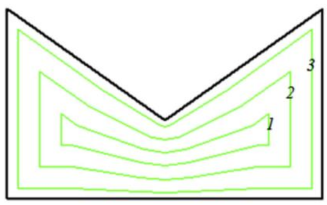

2.4 Current methods for quality improvement in WAAM process

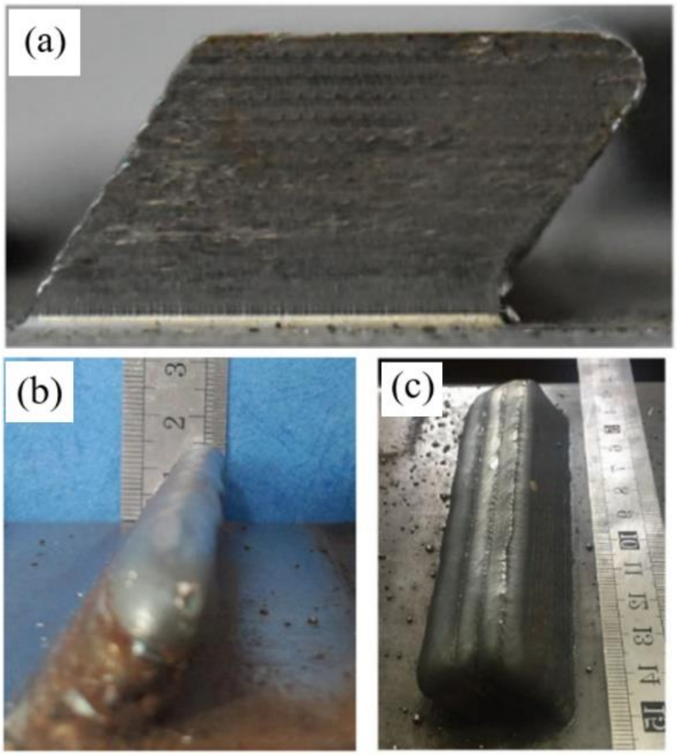

Fig.2. 5 Some inclined parts fabricated by WAAM.

For multi-directional WAAM, the downward flow of the molten metal, induced by the force of gravity, makes it difficult to properly control the deposition process. Shirali and Mills [52] addresses some several inherent defects formed during deposition, such as irregular bead shape, lack of penetration, porosity, undercut and formation of the humped bead, which are difficult to avoid. To fabricate parts with overhanging features, initially, researchers have investigated the process control strategies to deposit parts with an inclination angle. The fabrication methods of two kinds of inclined overhanging structures have been proposed, they are: (a) layers are deposited in the same vertical planar with different starting and ending positions, and (b) layers are deposited with different horizontal positions the layer toes. In the study by Panchagnula and Simhambhatla [16], a small overhanging part was successfully manufactured in planar deposition without extra support by employing the inherent overhanging capability of arc welding, as shown in Fig.2.5(a). To explore the maximum inclination angle of the self-support capability, a set of thin-walled parts has been deposited with, a set of discrete inclination angle values, the experimental results demonstrate a maximum of 30° can be achieved with proper welding setups. Nevertheless, the authors did not provide the detailed process control method to extend the overhanging capability. Xiong, et al. [32] studied the influence of process parameters on the formation of the inclined wall in a GWAM-based WAAM process, as shown in Fig.2.5(b). In the experiment, the influences of offset distance, wire feed speed, and welding torch travel speed on the inclination angle were examined and discussed. The experimental results showed that the higher travel speed and the lower wire feed speed benefited a larger inclination angle using GMAW in spray mode. The maximum inclination angle was extended to be more than 45˚with proper weld settings. Finally, a thin-walled cylinder part with geometrical feature was produced by the proposed process control strategy, as shown in Fig.2.6. However, the geometrical error on layer width and height were identified in the deposition process. The authors explain that the errors are inevitable due to the different heat dissipation in each layer. Inspired by this single bead overhanging deposition, Li, et al. [33] investigated fabrication of inclined multi-layer multi-bead parts using GMAW-based WAAM, as shown in Fig.2.5(c). According to the proposed mathematical model of the layers-overlapping process, the authors initially categorized inclined components into four groups: (a) parts with two negative slops, (b) parts with two positive slopes, (c) parts with a positive slope and a vertical slope, and (d) parts with a positive slope and a negative slope, as shown in Fig.2.7. It was found that material shortage always exists at the edge of the parts, to produce inclined parts with better geometry quality, more materials should be deposited to optimize the deposition process. Through the experimental results, it was found that the compensated amount of the filler material is depend on (a) the deigned inclination angle of the parts, (b) the profile of the initial bead, and (c) the step over distance between adjacent beads.

Fig.2. 6 Sample fabricated by [32].

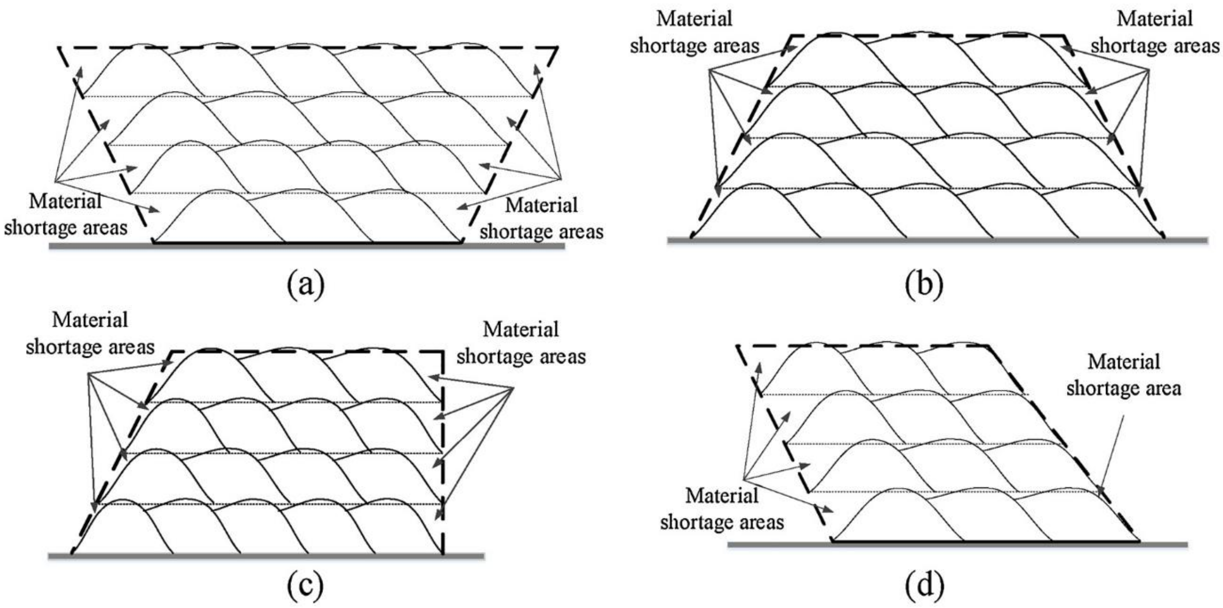

Fig.2. 7 Typical examples of inclined MLMB components.

To further extend the extend the inclination angle, Kazanas, et al. [34] conducted a preliminary study of the GMAW based multi-directional WAAM. The authors firstly stated that the Cold Metal Transfer (CMT), a variant of in short arc mode of GMAW, should be selected for the multidirectional process due to its low heat input. A set of horizontal thin-walled structures have been fabricated to examine the impacts of material ration, welding speed, and shielding gas on the weld bead formation, as shown in Fig.2.8(a). Then, through fabricating a few sample components with geometrical feature, the feasibility of this new strategy was validated, the successful fabrication of the sample demonstrates that the proposed method can significantly reduce the manufacturing time and cost. In addition, the authors claimed that humped weld beads are always formed in the horizontal deposition with improper weld settings, as shown in Fig.2.8(b). However, no further investigation of the humping issue in their study. It is necessary to conduct more studies on humping formation in positional deposition.

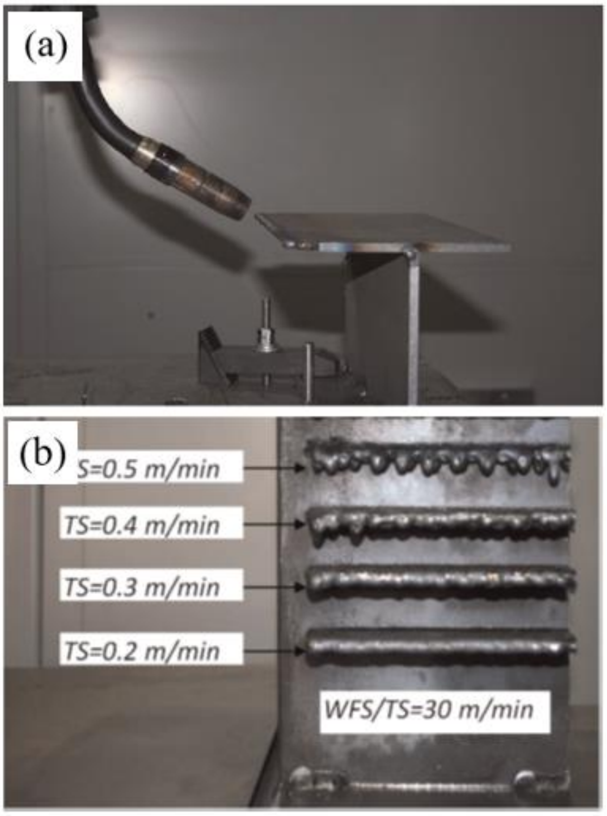

Fig.2. 8 horizontal parts by [34].

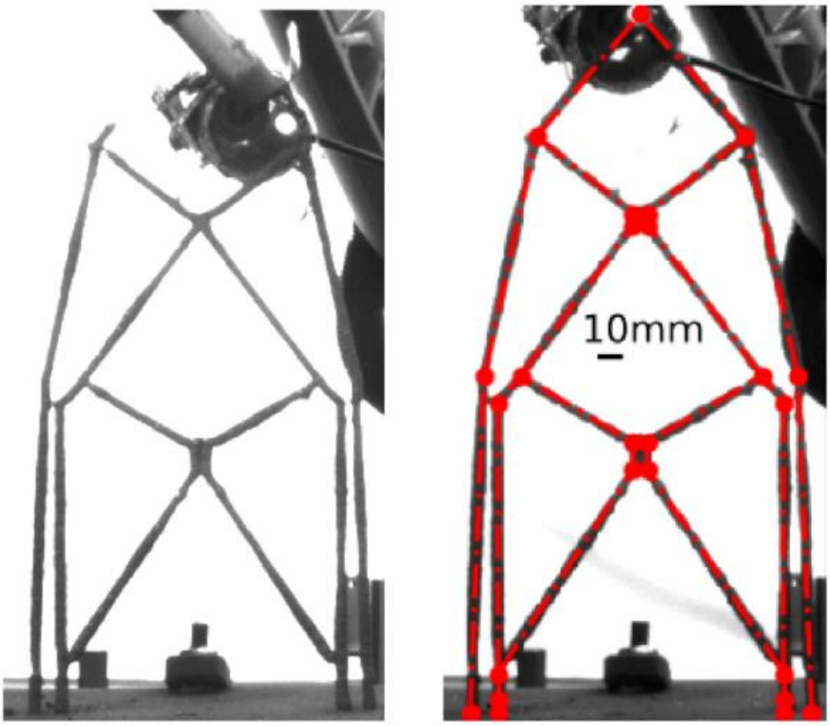

Fig.2. 9 Wire structures by WAAM.

In addition to traditional WAAM, Radel, et al. [53] presented an approach to automatically manufacture complex truss structures without any support using WAAM, as shown in Fig.2.9. To against the downward gravity, the surface tension force was identified as the major holding force that retains the molten metal on the parent layer in positional deposition. For a molten pool in the vertical direction, the effect of the weight of the molten weld metal compared to the surface tension can be calculated by Bond Number in (2.1) [54]

$$B_O = \frac{(g\rho)l^2}{\gamma} \qquad (2.1)$$

where g is the gravitational acceleration, ρ is the density difference of the weld metal and the gas. l is the characteristic length of the liquid part. A small Bond Number indicates that the molten metal flow is almost affected by surface tension force, the effect of the gravitational force can be ignored. Conversely, a high Bond Number normally above 1 means the gravitational force dominates. Thus, the molten pool size should be controlled to prevent weld bead sagging. In addition, to optimise the bead geometry, an image based closed-loop control strategy was developed to monitor the bead shape and computer-aided manufacturing (CAM) software was used to corrects the geometry of the bead for future deposition.

2.5 Humping phenomenon in GMAW

As aforementioned, humping phenomenon is a critical issue in positional deposition of the proposed strategy. It is necessary to investigate the humping formation and avoidance for the better geometry. According to Nguyen, et al. [55], humping can be described as the series of periodic undulation of the weld bead. Over the last 35 years, a considerable amount of literature has been published on humping phenomenon in conventional downhand welding[56]. Studies have covered several different welding processes, such as GMAW [57], GTAW [58-61], laser welding [62-65], electron beam [66, 67], and Submerged arc welding (SAW) [68]. Bradstreet [57] reported the mechanism of humped welds using plain carbon steel in the GMAW process. He suggested that the defect was produced by surface tension force and fluid flow patterns during GMAW. Mendez [58, 59] proposed a forehand technique to enhance the productivity in the GTAW process. To suppress humping occurrence, the welding torch can be rotated according to the established model. In such way, the plasma jet has a velocity component in the direction of motion of the torch. In laser welding, weld pool dynamic behaviours were investigated to gain a better understanding of humping in the study by Ai, et al. [63]; the experimental results demonstrated that humping formation is related to the tilted angle of keyhole, narrow and long molten pool and collision of fluid flow.

For applying to the GMAW-WAAM process, the rest of this subsection will concentrate mostly on humping during GMAW process. However, humping for different fusion welding processes will also be mentioned if it is applicable to GMAW.

The previous humping studies on GMAW referred to above fall into three groups; experimental observation, modelling, and numerical simulation. Originally the studies mainly relied on the experimental observation of the weld bead profile in high-speed GMAW. One well-known study that is often cited in research on humping is that of Bradstreet [57], who found that the defect was produced by surface tension force and fluid flow patterns during GMAW. He found that the humped weld bead can be produced by improper welding process parameters including system energy input, welding speed, the surface condition, and chemical composition of the parent metal. Although his preliminary study provided a better understanding of humping in GMAW, the mechanism was still unclear. Since the occurrence of humping limits the welding speed of conventional downhand WAAM. Adebayo, et al. [69] investigated humping formation in WAAM using the CMT welding process. The authors examined the effects of wire feed speed and travel speed on bead geometries and the experimental results showed that under the test conditions uesd, there exists a limiting speed of 600 mm/min at which humping starts to take place. However, the universality of these findings was limited to a fixed welding trial. Other researchers have applied an external magnetic field to control the welding process and suppress the humping formation [70-72]. The auxiliary magnetic field has significant influences on the weld pool flow dynamics, arc column and the metal transfer. Base on those findings, the optimised excitation currents were experimentally determined for GMAW.

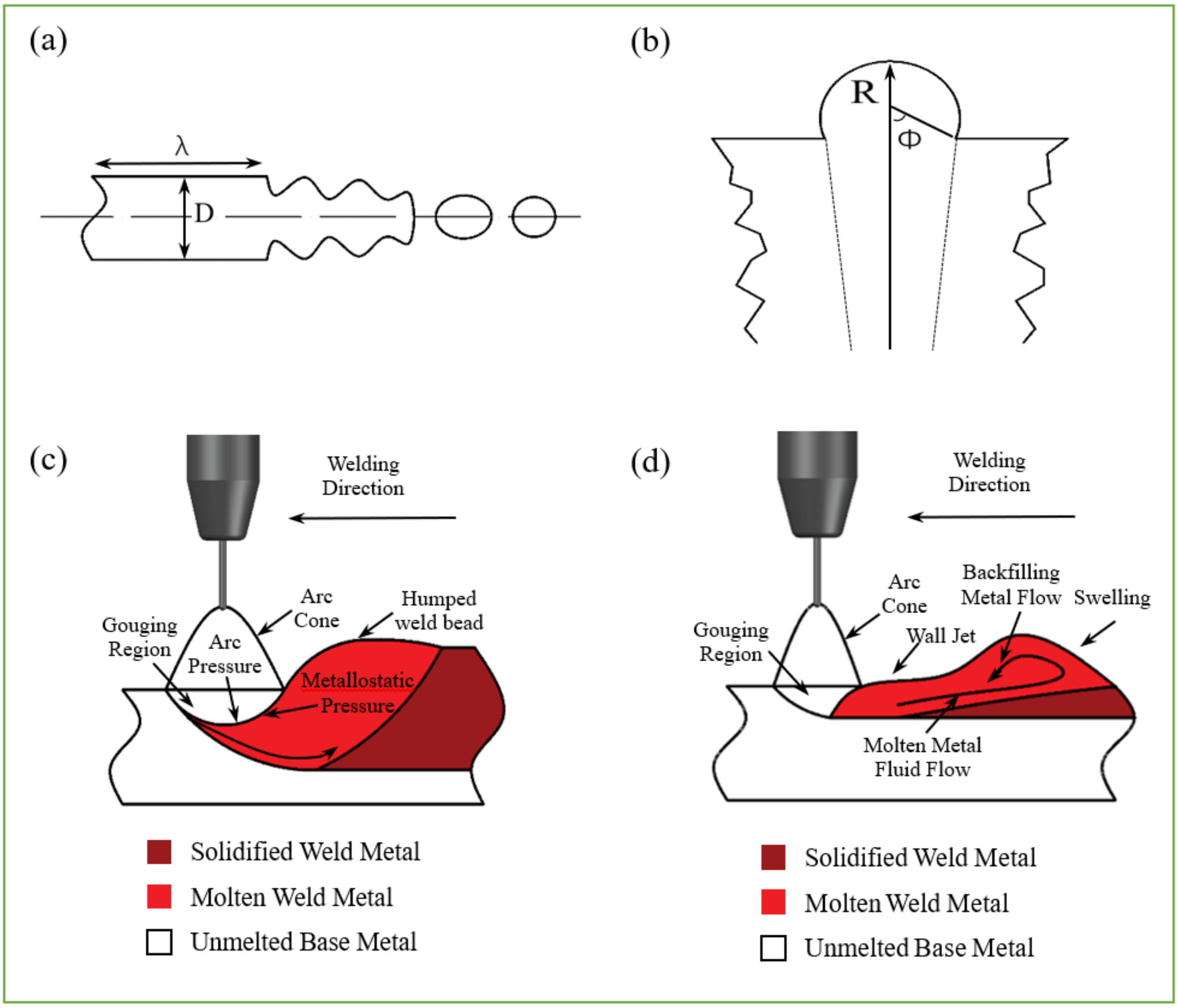

Fig.2. 10 Existing humping models.

To further study the humping formation in GMAW, the fundamental mechanisms of humping were investigated through establishing physical models. Based on the Rayleigh instability model [73], the molten metal pool is considered to have a cylindrical shape, As shown in Fig.2.10(a). Gratzke, et al. [74] modified the Rayleigh instability model to a Capillary instability model to explain driving forces responsible for humping. As shown in Fig.2.10(b), the molten metal pool was assumed to be partially bounded liquid cylinder. They suggested that the humping commenced when the width/length ratio of the weld pool is less than 1/2 π. Some studies considered the strong arc force was the main reason for the onset of humping [75-77]. As shown in Fig.2.10(c), Mendez, et al. [59] established an arc force model using the static force balance theory. The presented model indicates that the humping occurs when the arc pressure becomes larger than the metal pressure. To be more specific, Nguyen, et al. [55] explained when the arc force exceeded the metallostatic pressure, the weld pool underneath the arc was depressed and turned into a very thin layer of molten metal. The molten metal underneath the arc pressure was pushed toward the rear of the molten pool and the humped weld bead was produced with the extra metal solidifying while the gouging region formed due to the missing material. It is believed the arc pressure model may describe the morphology of humping qualitatively, however, what is not yet understood is the periodic behaviour of the humping phenomenon. Nguyen, et al. [78] obtained experimental results and observations using a LaserStrobe video system. They developed a new curved wall jet model to explain the generation of bead hump in the GMAW process. The authors suggested that the humping was enlarged and formed with the strong backward fluid flow of molten metal, which mainly was induced by the arc plasma force and droplet impact force, as shown in Fig.2.10(d). The molten metal backfills the gouging area when welding with a low speed. However, the wall jet becomes more prolonged and narrower with a higher welding speed, resulting in the premature solidification of the wall jet which prevents the backfilling fluid flow and thereby the humps and valleys formed.

Based on the aforementioned theoretical models, advanced computer simulation technologies have been employed to assist researchers in understanding of the temperature distributions and fluid flows behaviours of humping phenomenon during the GMAW process [79-83]. Wu, et al. [79] established three-dimensional mathematical models to simulate the convection in GMAW processes. Through simulating the fluid flow and heat transfer behaviour in normal and high-speed welding, they identified two factors are responsible for the humping generation: the strong momentum of the backward fluid flow and the capillary instability of the fluid channel. In the study of Cho and Farson [82], three-dimensional numerical simulations were also employed to study humping in GMAW. They suggested the formation of a thin liquid channel and premature solidification of the melt in the thin channel, associated with humping phenomenon.

2.6 Robot path planning

Compared to common WAAM process which only deposit parts along the fixed vertical-up direction, the programming process becomes more complicated due to the following two reasons.

(i) Most existing WAAM systems plan torch trajectories based on the part CAD model and assuming robot/machine can always reach those trajectories, which is true when part size is not large and the welding torch is always kept down hand. However, the collision-free robot motion for multiple torch orientations, which usually includes searching for an optimal reachable solution from multiple robot configurations, is new to the WAAM research field.

(ii) The deposition sequence is no longer from the bottom to the top as the overhanging structure can be built at different stages of the manufacturing. The optimisation of weld sequence plays a critical role to avoid collision between the torch and partially deposited component.

Path planning in robotic welding originally concerned the problems of moving welding torch along the predetermined weld trajectory without any clash. Hence, the collision avoidance is a fundamental issue when programming robot motion for welding tasks. In robot welding there are two main methods of robot motion programming, online programming and offline programming. Online programming requires human operation including lead-through and walk-through, it is considered as a simple programming method however the flexibility too low for WAAM process. On the other hand, offline programming is used to generate robot programs through either manual or automatic programing method [84]. So, it is suitable for an automated system. The workflow of the typical process is shown in Fig.2.11 [84]. the main steps are: (i) 3D model generation, the 3D model of the target part can be generated through various sensing technologies. (ii) Tag creation, the start and end points are identified for the robot path. (iii) Trajectory planning, the robot motions are planned and the collision between, robot and workpiece is assessed. (iv) Process planning, the welding sequence is reorganized for the most effective welding operation. (v) Post processing, the necessary communication between robot controller and welding machine and other sensors are programmed into the robot language. (vi) Calibration, the differences between the modelled data and the real manufacturing environment are compared and compensated. In WAAM process, steps (i) and (vi) are unnecessary compared to normal welding process. Step (v) can be easily completed by a translator.

Current studies attempt to develop the optimal collision-free robot motion strategies through two major steps, environment modelling and optimal path searching [85]. In the study by Gai, et al. [86], the obstacles and robot body are simulated by an external sensor and then transformed in to Configuration Space (C-Space), where the robot configuration is defined by a set of joint coordinates [87]. Finally, the proposed Artificial Potential Field was applied to generate a collision free weld path. Wang, et al. [85] also reported a welding robot collision free path optimization strategy. The environment including robot and obstacles is simulated through a simple grid method and then the optimized collision free robot motion is programmed based on the proposed Ant Colony Optimization algorithm. Simulation results demonstrate that the proposed system can automatically generate the shortest robot path without clash. In addition, Larkin, et al. [88] pointed out that the welding quality is sometimes affected when using traditional robot motion planning methods, because the welding task is not a simple pick-and-place operation using the position of the object being moved, the configuration of the welding torch will affect the appearance and quality of the weld bead. To improve the welding quality, they present a Probabilistic RoadMap motion planner for automatic welding robots motion generation concerning the operation range of the welding torch angle [88, 89]. Wang, et al. [85] also reported a method for generating a collision-free path for welding robot. Firstly, the welding environment is modelled using a grid method. Then, the ant colony algorithm is used to search the best algorithm to adjust the welding path. A secondary optimization approach is used to improve the system performance. The simulation results showed that the shortest collision-free path was obtained through optimizing the welding path. In addition, researchers also applied Genetic algorithm [90], and Artificial bee colony algorithm [91] to search the optimal path.

There are many restrictions to apply these strategies to multi-directional WAAM directly. This is due to the significant differences between traditional welding and multi-directional WAAM. In the welding process, the geometry of the part is fixed, and the motion planning is in a static environment. However, the volume of the part keeps growing in the WAAM deposition process, which makes the motion planning more complicated in a semi dynamic environment. The collision model of the workpiece needs to be updated after each layer of deposition. Since the sequence of the deposition affects the collision model for each weld, the layer sequence becomes critical for a successful collision free deposition path planning [8]. The deposition sequence and single layer path planning interwinds together and become a complicated optimisation problem.

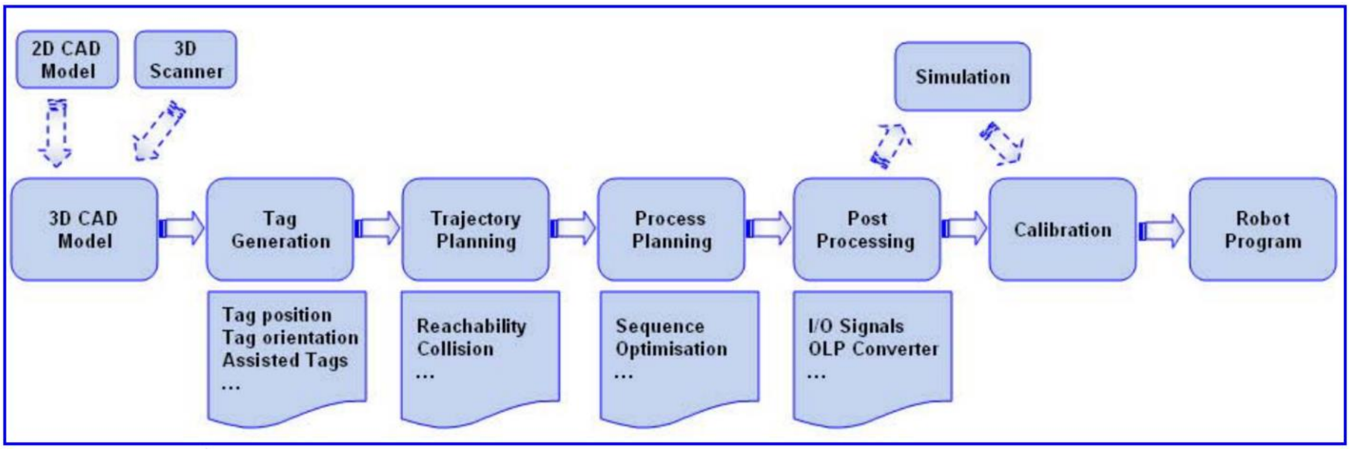

Fig.2. 11 The process of robot offline programming.

2.7 Summary and scope of this work

As the current studies reviewed in this chapter, the WAAM process is still limited to deposit parts in the vertical up direction. It only can be called as 2.5D printing. To realize the ture 3D printing, a multi-directional WAAM process is expected to be developed for significently reducing manufactring time and cost. To develep such a inovative technology for industrial practical use, a few gaps have been identified as listed below.

First, the positional deposition methods need to be developed. the gravitational force has a great negative impact on the bead formation. To deposit weld bead along multiple directions, the forming mechanism of a weld bead in various deposition directions is necessary to be explored. In addition, a set of practical guidelines for multi-directional WAAM is required to be carried out for achieving a stable deposition process.

Secondly, although some of the presented studies may provide knowledge of the humping phenomenon in a flat position, their ability to explain humping in a horizontal or vertical position has not been experimentally demonstrated, the exact mechanism is still unclear. In the vertical or horizontal deposition, the sagged beadlike shape indicates that that the downward flow of the molten metal induced by the gravitational force may be a critical driving factor of the humping. A new humping metal flow model may be required to explain the great influence of gravity in positional WAAM.

Thirdly, a practical robot path planning strategy needs to be developed. Compared to common WAAM process which only deposit parts along the fixed vertical-up direction, the programming process becomes more complicated. However, the robot path planning is important for developing a automated manufacturing system. It is necessary to develop such a system for the future application.

Finally, as a manicuring process, an elaborate process planning algorithm is required to be carried out for industrial users. The system is able to fabricate parts for CAD model to the final near-net shape product. The knowledge obtained in this study will be used to develop such a system. In addition, for some exiting WAAM algorithms that can be applied to the multi-directional system will able be integrated into the new system.

Chapter 3

Application development and process optimization

3.1 Introduction

For multi-directional WAAM, the downward flow of the molten metal, induced by the force of gravity, makes it difficult to properly control the deposition process. Shirali and Mills [52] addresses some several inherent defects formed during deposition, such as irregular bead shape, lack of penetration, porosity, undercut and formation of the humped bead, which are difficult to avoid. In the study of molten pool behaviour and mechanism of weld forming in positional GMAW welding, many researchers focused on the selection of the optimal welding parameters. In the studies of Randhawa, et al. [92] and Ghosh, et al. [93], the use of optimal welding parameters can significantly improve the weld bead geometry in vertical welding. Recently, three-dimensional numerical simulation is used to describe molten pool behaviours [94, 95]. They investigated the molten pool flow patterns for various welding positions. In addition, some molten pool control methods, such as rotating arc [96, 97], and tandem arc [98], were applied to the positional welding for a better weld bead geometry.

Kazanas, et al. [34] conducted a preliminary study of the GMAW based multi-directional WAAM. Through the conducted experiment, the feasibility of fabricating parts with overhangs using multi-directional WAAM was verified and the torch travel speed selection was claimed to be critical for the process. Recently, Radel, et al. [53] presented an approach to automatically manufacture complex truss structures without any support. To optimize the bead geometry, an image based closed-loop control strategy was developed to monitor the bead shape and computer-aided manufacturing (CAM) software was used to corrects the geometry of the bead for future deposition. Nevertheless, there are still several inherent technical challenges in the application of the GMAW-based multi-directional additive manufacturing. The forming mechanism of a weld bead in various deposition directions has not been explored for multi-directional WAAM. Therefore, it is necessary to establish a set of practical guidelines for multi-directional WAAM. In this chapter, the positional deposition process is investigated for developing the multi-directional process. Initially, different GMAW transfer modes were evaluated based on the metal droplet kinetic and the weld bead geometry. Subsequently, the effect of process parameters on bead formation and process stability were quantitatively investigated. Finally, three case studies are given in Section 5 and followed by a conclusion in Section 6.

3.2 Metal transfer in multi-directional GMAW-based WAAM

Compared to conventional GMAW-based WAAM, the multi-directional deposition process is more difficult to control mainly due to the influence of gravitational force. In this section, two major issues are addressed: (a) the transfer of metal droplets from filler wire tip to the molten pool in the proper position, and (b) weld pool geometry and formation of the desired weld bead profile.

3.2.1 Metal droplet kinetic

Generally, the basic metal transfer modes of GMAW can be classified into free flight and short circuiting [24]. Free flight transfer can be further divided into Spray, Globular and Repelled modes. During Free Flight modes, the droplet trajectory from the wire tip to the weld pool is important. Norrish [24] describes the mechanism of metal transfer in terms of the balance of forces acting on the system, which includes gravitational force, aerodynamic drag, electromagnetic forces, vapour jet forces and surface tension. In positional free flight transfer, the gravitational force may be sufficient to exceed the axial forces which would normally project the droplet across the arc resulting in displacement of the material from the target position. This is illustrated in Fig.3.1(a). In addition, the common spray transfer mode only operates above a minimum transition current, a large molten weld pool is usually formed, which is undesirable for the multi-directional deposition process.

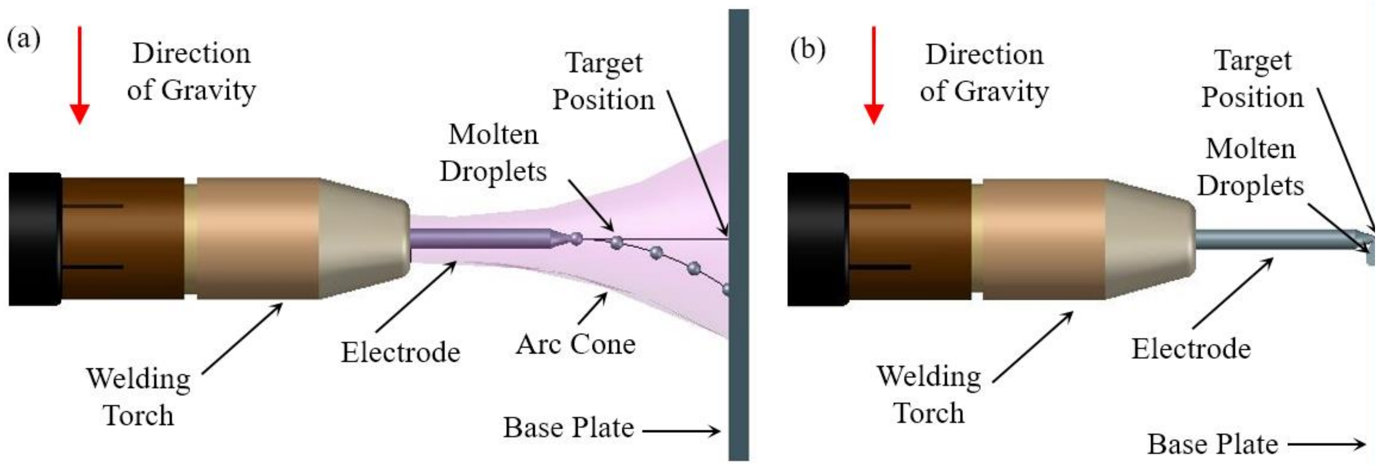

Fig.3. 1 The trajectory of the molten droplets (a) in Free flight transfer and (b) in short arc transfer

In short arc transfer, a droplet forms on the wire tip during the arcing phase, but material transfers when the wire tip contacts the base metal. Droplets transfer to the weld pool is influenced by the gravitational force less. Fig.3.1(b) indicates that the molten metal normally transfers accurately on the target position when the correct welding parameters are used. For this reason, the short arc transfer has been used to deposit material in all positions.

In addition, the positional performance of both free flight and short-circuiting transfer may be improved by using dynamic control of transient welding current and wire feeding. These techniques are now known collectively as 'waveform controlled' in GMAW. Norrish [24] also argues in the case of spray transfer, the current may be pulsed to produce a strong axial transfer of droplets at low mean current. In the case of short-circuiting mode, the 'controlled short-circuiting' processes may be used.

3.2.2 Weld pool geometry

As shown in Fig.3.2, a further issue coming with horizontal deposition is the sagged bead or downward flow of molten metal, Soderstrom and Mendez [99] and Motta, et al. [100] refer it as humping and dripping phenomenon, respectively. During the metal solidification process, the molten pool may sag before it freezes, this results in a poor bead profile. It is therefore important to investigate the influence of the forces affecting final bead quality in multi-directional GMAW based WAMM process. For simplicity, a static force balance model for a molten pool in horizontal welding is adopted, as shown in Fig.3.3. In addition to normal force N, the other three forces which influence the formation process of the molten pool are gravitational force G, arc pressure f_{arc}, and surface tension force f_{γ}.

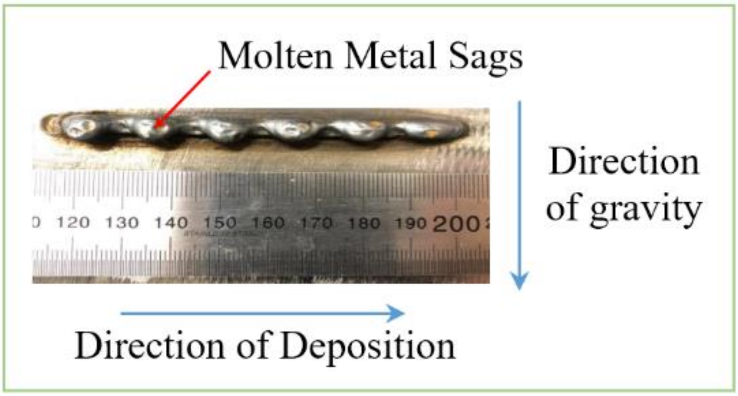

Fig.3. 3 The sagged bead geometry in the horizontal deposition.

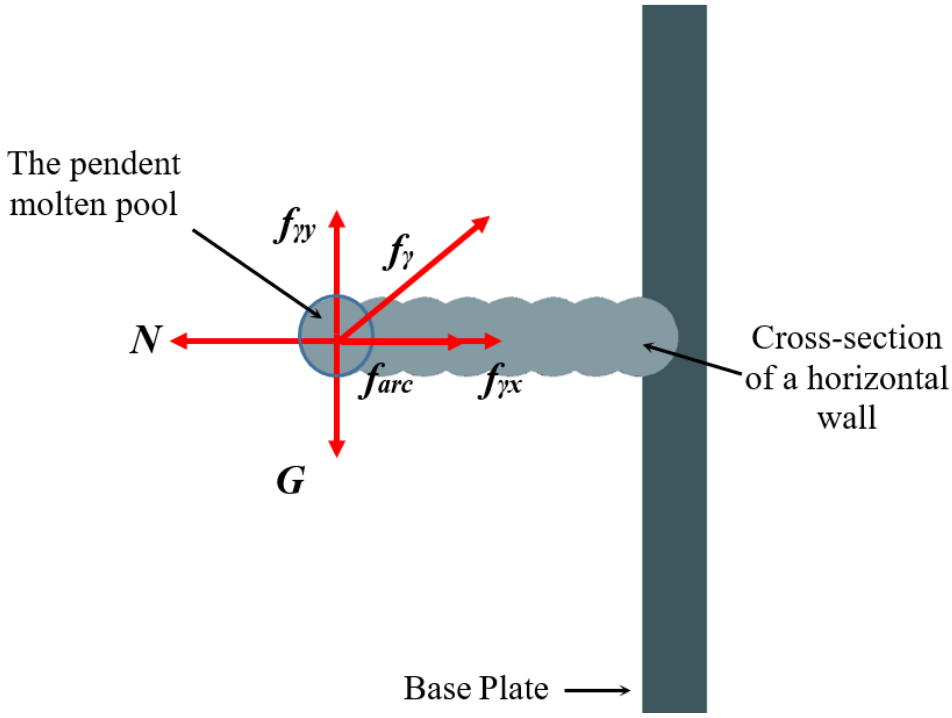

Fig.3. 2 A force model for a pendent molten pool in positional deposition.

According to [101], the static force balance theory, the molten droplet will remain balanced on the base metal in the vertical position when the static detaching forces do not exceed the holding force. The force model indicates that the surface tension force can be decomposed along vertical and horizontal directions. During horizontal or vertical welding, the component of the surface tension force along the vertical direction, $f_{\gamma y}$, acts as the holding force while the gravitational force tends to cause the detachment of the pendent molten pool. The gravitational force of molten material deposited in a unit time is given by:

$$G = \frac{\pi r^2 WFS}{TS}\rho g \tag{3.1}$$

where ρ and r are the density and radius of the electrode wire. WFS and TS are the wire feed speed and welding torch travel speed, respectively. g is the gravitational constant.

Generally, the surface tension force acts as the major force holding the pending molten pool during positional welding. The sum of surface tension, which holds and allows the molten bead to be stable, acts on the curved liquid surface at the border of the liquid and solid material region. The surface tension coefficient γ of the molten metal, which represents the surface tension force per unit length, is a critical factor that affects this force.

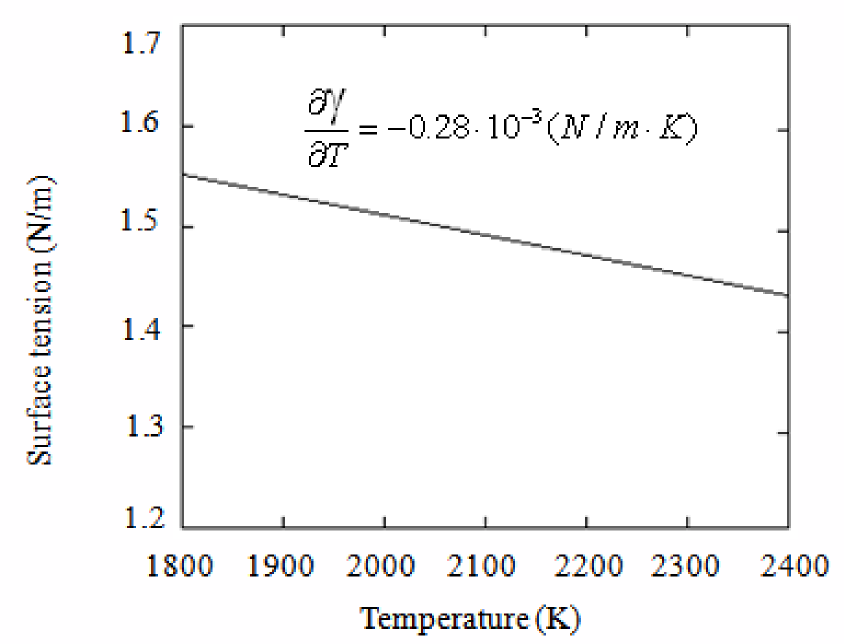

Fig.3. 4 Surface tension of steel S235 as a function of temperature.

According to Eötvös rule [102], the surface tension coefficient is significantly affected by the temperature of the liquid [103], as shown in Fig.3.4. In their model, the empirical equation to relate the surface tension coefficient γ and temperature T is:

$$\gamma V_0^{2/3} = k(T_c - T) \tag{3.2}$$

where V_0 is the molar volume of the substance. T_c is a critical temperature whose value is constant for a certain substance. k is a constant for almost all substances. Magnitis, et al. [104] calculates its value as $k = 2.1 \times 10^{-7}[JK^{-1}mol^{-2/3}]$

Moore [105] modified Eötvös equation to:

$$\gamma V_0^{2/3} = k(T_c - T - 6) \tag{3.3}$$

in this variant, the equation is more accurate at lower temperatures through employing a 6-degree kelvins temperature offset.

Besides the general expressions above, Xiong, et al. [32] presented a formula to predict the variation of the surface tension force in welding. The surface tension coefficient γ is considered to vary linearly with the temperature T, which is given by:

$$\gamma = \gamma_m^0 - A_s(T - T_m) \tag{3.4}$$

where γ_m^0 is the surface tension coefficient of pure metal at the melting point, which should be constant for filler material. A_s can be calculated as the negative of $\partial\gamma/\partial T$ for pure metal, which is also considered as a constant when the temperature is much above the melting point. T_m is the melting point of the filler material. Thus, to take advantage of surface tension for rod retention, a lower temperature weld pool is desired. In other words, the heat input should be as low as possible to increase the surface tension force.

The molten pool shape is also controlled by the freezing rate of the molten pool. If the pool freezes quickly, it will retain its shape. A fast-freezing rate is normally determined by low heat input. Based on the analysis above, the dependence of surface tension and freezing rate is verified. It reveals that the control of heat input is critical for the successful multi-directional WAAM. Besides, Norrish [24] explains the composition of shielding gas and Li, et al. [106] tests the surface active elements, such as oxygen or sulphur on steel, which also affects the surface tension. From the preceding analysis and section 2.1, it is clear that the short circuit mode of operation is most suitable for multi-directional WAAM. In addition, Norrish and Cuiuri [107] explain that the controlled short circuit process offers improved stability, lower spatter and better process tolerance.

Most commonly, these controlled short circuit processes rely on transient current control to prepare a droplet on the wire tip during the arcing period and minimise short circuit rupture current [2]. In some cases, this is combined with cyclic wire movement to assist the short circuit rupture. In the current work, the later control approach was used with a commercial "cold metal transfer (CMT)" system supplied by Fronius.

3.3 Experimental setup

The plain carbon steel ER70S-6 filler wire, with a diameter of 0.9 mm, was selected as the feedstock material in the welding system. A Q235 steel base plate was used as the substrate to support metal deposition. The dimensions of this plate were 300 mm × 300 mm × 10 mm. The chemical composition (in wt. %) of the wire electrode ER70S-6 and base metal Q235 are given in Table 3.1. A shielding gas mixture of Argon (80%) and CO2 (20%) was used at a flow rate of 18 L/min.

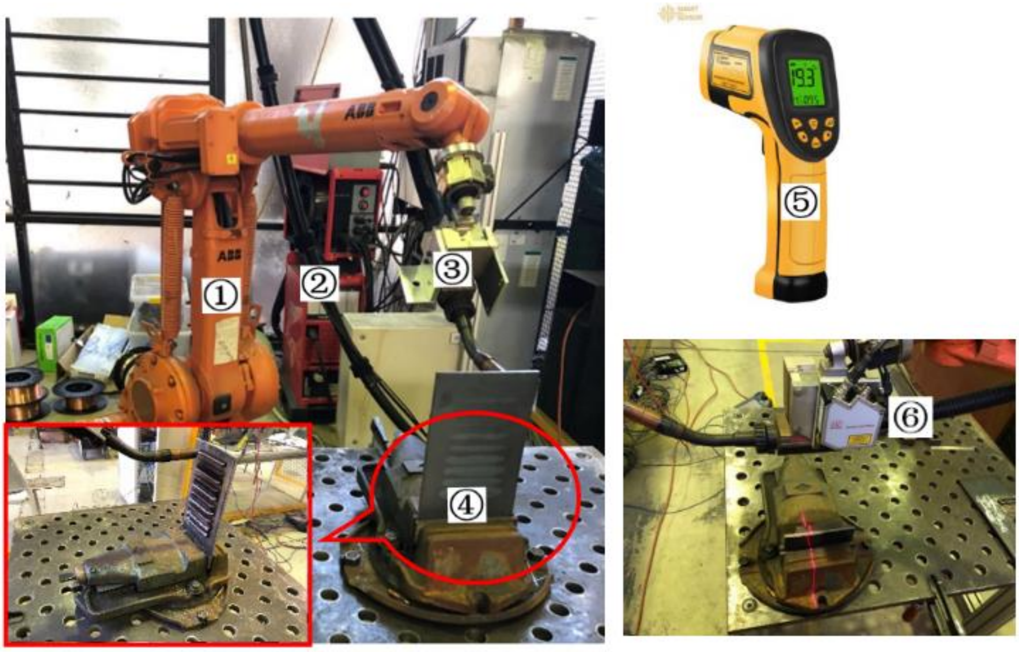

① ABB IRB 1400 Industrial Robot	② Fronius CMT Welding machine
③ Welding Torch	④ Mechanic Vice
⑤ Infrared Pyrometer	⑥ Laser Displacement Sensor

Fig.3. 5 The controlled short circuit (CMT) welding system and robot manipulator.

The tests were implemented using a robotic welding system developed at the University of Wollongong, as shown in Fig.3.5. The welding system was a Fronius TPS 4000 CMT Advanced unit consisting of a welding controller and power source, coupled to a CMT wire feeder, and the welding torch. As with similar systems, the welding parameters are automatically adjusted in response to settings of wire feed speed, using a synergic algorithm embedded in the controller. The welding torch was mounted on an ABB IRB 1400 industrial robot. The controller of the welding power source is interfaced with the robot controller, and subsequently, the RobotStudio (simulation and programming software for the ABB robot) was used to program the torch motion and coordinate the weld settings. A structured laser scanning system was integrated into the robotic welding system to measure the bead profile. In addition, to exclude the interference from temperature differences, an infrared pyrometer was used to monitor the temperature of the previous weld bead. In this study, each subsequent layer was deposited on the substrate layer after the bead cooled to room temperature.

Table 3. 1 ER70S-6 and Q235 Chemical compositions & ranges (wt.%).

Alloy	C	Mn	Si	Cu	S	P	Fe
ER70S-6	0.08	1.53	0.88	0.18	0.01	0.009	Bal
Q235	≤0.17	0.35-0.80	≤0.35	-	≤0.40	≤0.35	Bal

In this study, the basic experiments were designed to examine the performance of the controlled short circuit transfer welding technology used in the multi-directional WAAM. Also, the impact of the several process parameter and weld setting on the metal transfer and bead geometry were investigated. In the test, a steel base plate (Q235) was securely clamped in the vertical position by a mechanical vice, as shown in Fig.3.5, with the welding torch moved either horizontally or vertically perpendicular to the base plate. The experiments were divided into four phases to investigate the impacts of WFS, TS, NTWD and torch angle on the geometry variation of the weld bead.

3.4 Results and analysis

In order to produce weld beads with preferred geometry, the effects of each welding parameter on the metal transfer process are crucial to be identified. In this section, several major process parameters were studied, including WFS, TS, NTWD and welding torch angle. The results were recorded to investigate the effect of each process parameters and to give a guide for multi-directional WAAM technology.

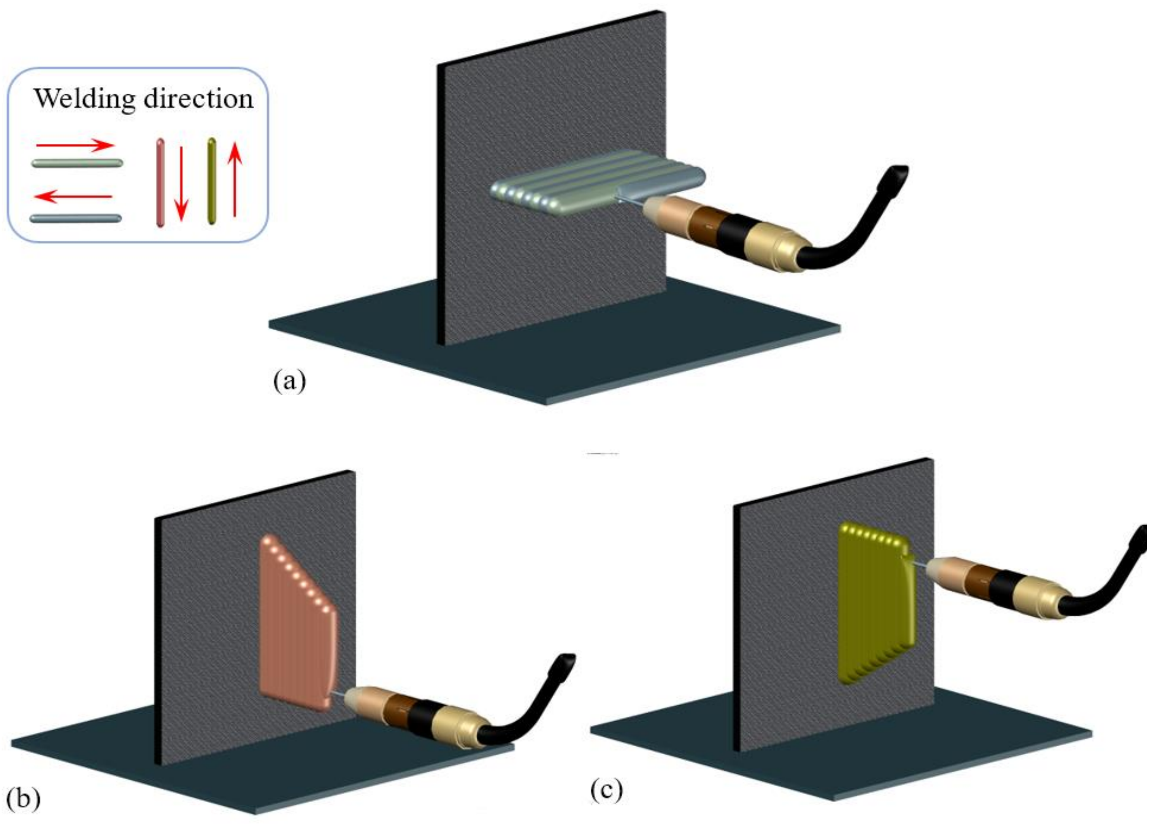

Fig.3. 6 Demonstration of fabrication approach for (a) Horizontal deposition, (b) Vertical-down deposition, and (c) Vertical-up deposition.

For the horizontal deposition process, the length of the bead was set to 120 mm. To avoid the uneven height of the bead at either the start and end of the bead, the welding direction was alternated after every layer. This resulted in the regular geometry of the entire bead, as illustrated schematically in Fig.3.6(a). However, the same deposition strategy cannot be applied to vertical welding. Alternating start-stop positions would not distinguish the geometry difference between vertical-up and vertical-down deposition. The welding strategy for vertical deposition is shown as follows: the length of first vertical deposit was set to 120 mm and the length of each subsequent bead was reduced 5 mm at the start of the bead (Weld bead geometry at the start of the weld bead is often abnormal compared with the middle region, which may affect the experimental results if the swelling keeps accumulating), as shown in Fig.3.6(b) and Fig.3.6(c). Each horizontal or vertical wall includes ten layers, the torch was perpendicular to the base plate, and the NTWD for both horizontal and vertical weld was set to 10 mm.

3.4.1 Effect of WFS

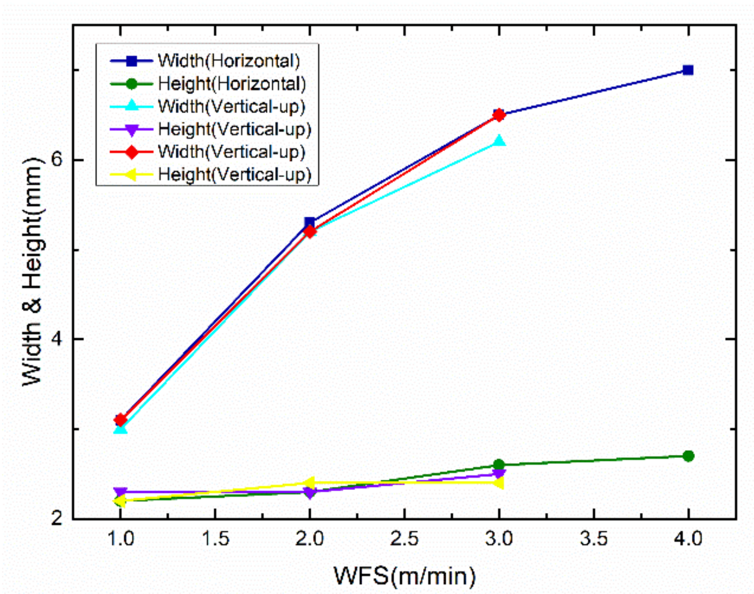

Fig.3. 7 The experimental results of bead width (w) and height (h).

Table 3. 2 Welding parameters and settings of the first test group.

Index	BD	WFS (m/min)	TS (m/min)	*w* (mm)	*h* (mm)	Geometry
1	Horizontal	1	0.1	3.1	2.2	Good
2	Horizontal	2	0.1	5.3	2.3	Good
3	Horizontal	3	0.1	6.5	2.6	Good
4	Horizontal	4	0.1	7.0	2.7	Acceptable
5	Horizontal	5	0.1	-	-	Irregular

To investigate the effect of the WFS, the TS was kept constant at 0.1m/min while the WFS was varied between 1.0 and 5.0m/min. Table 3.2 lists the welding parameters and settings for depositing thin walled structures with ten layers in the horizontal direction. The information includes build direction (BD), WFS, TS, bead with (w), bead height (h), and a visual assessment of geometry (evaluated as good, acceptable or irregular). The average weld bead height and width of each the test are shown in Fig.3.7. It can be seen that the bead width increases significantly from 3.1 to 7.0 mm with an increase in WFS. Meanwhile, the bead height remains nearly constant with the variation of WFS. This demonstrates that when keeping the TS constant, the increase of the deposited material is proportional to the increase in bead/wall width.

Fig.3.8 displays the geometry of thin-walled parts under different WFSs. The bead geometry deteriorates with an increase in WFS, and an irregular bead shape in test five. According to the force model given in Fig.3.3 and static force balance theory, there are three reasons to explain this phenomenon. Firstly, an increase in WFS causes a reduction in surface tension, which subsequently reduces the holding force. For the following, in GMAW welding, the relationship between mean welding current I_m and WFS is almost linear in the range used here. Keeping the TS constant, the increase of WFS is associated with an increase in welding current, and thereby a higher heat input for a desired limited WFS. As explained in Section 2.2, the surface tension force is inversely related to temperature. Thus, the use of high WFS decreases the surface tension making it difficult to retain weld pool stability. Secondly, excessive energy heat input also extends the metal solidification time. With a longer freezing time, the weld bead geometry deteriorates due to the downward flow of molten metal. In some instances, molten droplets fall from the base metal when using a large WFS. In addition, the volume and mass of the weld metal increase with increased WFS, thereby increasing the gravitational force.

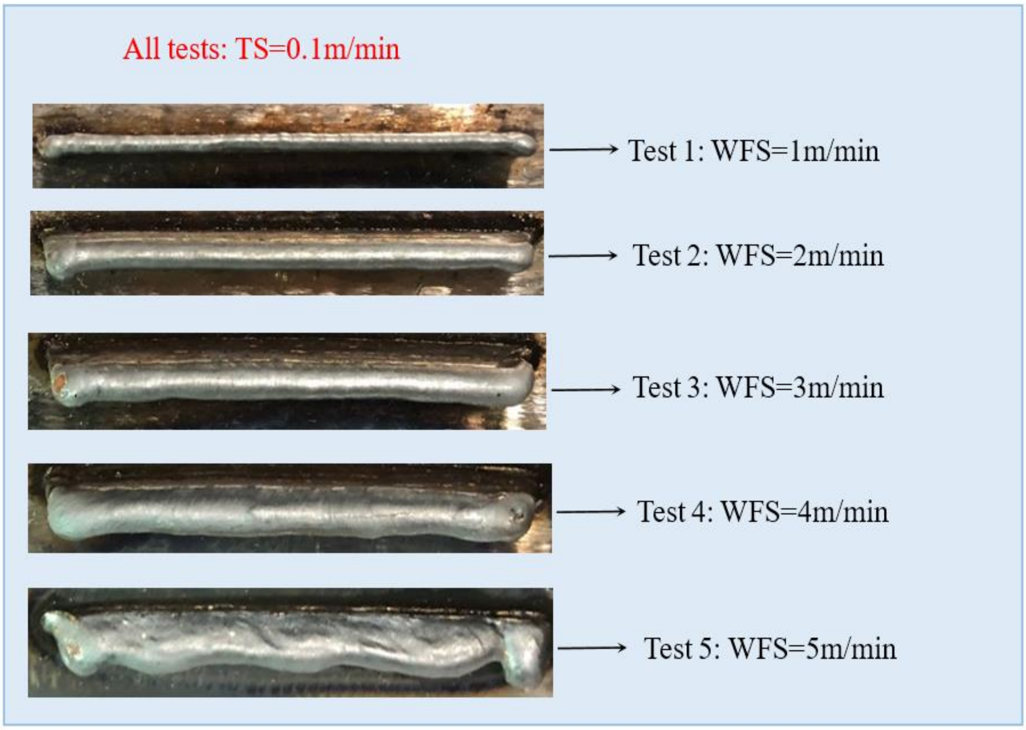

Fig.3. 8 Geometry appearance of horizontal position thin-walled parts under different WFSs.

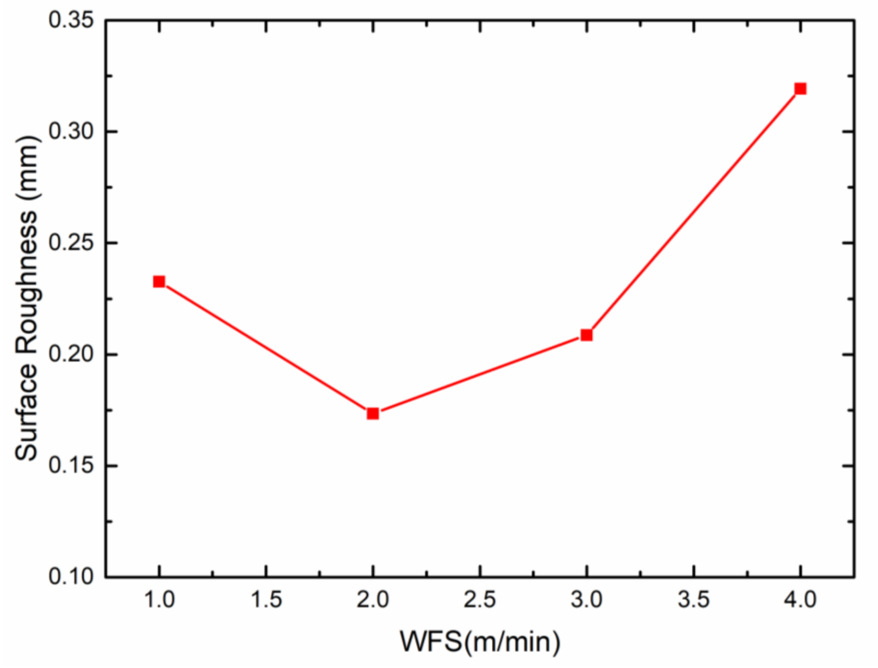

Fig.3. 9 Surface roughness with WFS varied from 1 to 4 m/min.

Table 3. 3 Welding parameters and settings of the second test group.

Index	BD	WFS (m/min)	TS (m/min)	*w* (mm)	*h* (mm)	Geometry
1	Vertical-up	1	0.1	3.0	2.3	Good
2	Vertical-up	2	0.1	5.2	2.3	Good
3	Vertical-up	3	0.1	6.2	2.5	Acceptable
4	Vertical-up	4	0.1	-	-	Irregular
5	Vertical-up	5	0.1	-	-	Irregular
6	Vertical-down	1	0.1	3.1	2.2	Good
7	Vertical-down	2	0.1	5.2	2.4	Good
8	Vertical-down	3	0.1	6.5	2.4	Acceptable
9	Vertical-down	4	0.1	-	-	Irregular
10	Vertical-down	5	0.1	-	-	Irregular

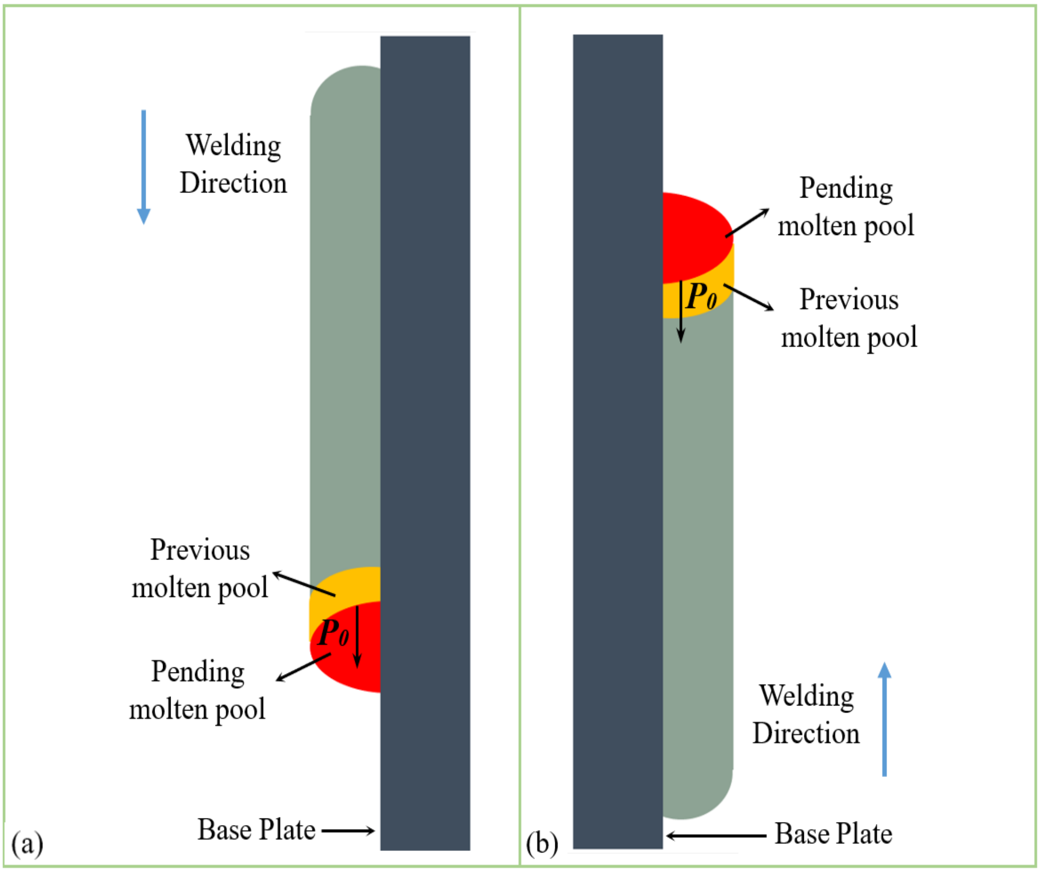

Fig.3. 10 The molten pool in the (a) vertical-down and (b) vertical-up deposition.

On the other hand, a high deposition rate with high welding current has several advantages. Firstly, the use of high welding current can provide better penetration and depth of fusion, which can improve the surface quality of the deposits. The results of the surface roughness of the deposited thin wall are given in Fig.3.9. Note that the waviness on the bottom of walls is more evident than the top side. For this reason, the bottom side was chosen to evaluate the surface quality. Yuan, et al. [108] provides the detailed surface roughness measurement method. The parabolic shaped model indicates that the surface quality improved when the WFS increased to 2m/min but soon deteriorates when WFS continues to increase up to 4m/min. The more energy is input to the welding pool with the high welding current eventually results in a decreased surface tension, and the molten pool falls downward. A properly determined WFS does improve the surface evenness, but higher deposition rates are a prominent advantage of wire-feed additive manufacture, and because the surface appearance is of less concern if a post-machining process is used, a lower surface quality and higher deposition rate may benefit the productivity of the process.

The same process parameters were used to produce thin walls in the vertical-up and vertical-down direction, with the results presented in Table 3.3. It reveals that the bead geometry variation is similar to a horizontal deposition, as shown in Fig.3.7. However, the maximum WFS of vertical welding is reduced to 3m/min compared to 4m/min in the horizontal welding. As shown in Fig.3.10, the molten pool can be divided into the previous molten pool and the pending molten pool for both vertical deposition directions. In the vertical-down deposition, the previous molten metal flows downward slightly on the pending molten pool during the solidification process. On the other hand, in the vertical-up deposition, the pending molten pool flows downward on the previous molten metal. In both cases, a larger surface tension force f_γ is required in a vertical deposition, which results in a limited operating range of WFS in the vertical deposition compared to the horizontal deposition.

3.4.2 Effect of TS

TS is another major parameter affecting positional welding. To study the effect of torch travel speed, a group of tests were conducted with TS being varied from 0.1m/min to0.6m/min, while the WFS was kept to a constant 4m/min, as shown in Table 3.4. Since the deposition TS is inversely proportional to the deposition volume, and both wall height and width reduce with the increase of TS, as the results shown in Fig.3.11. In terms of the geometrical quality of the deposits, both the filler material volume and the heat input are reduced with the increase of TS while the WFS is constant. The wall quality improved due to the low system energy input and a corresponding increase in surface tension force. However, when the TS is increased to 0.4m/min, the bead geometry starts deteriorating. Fig.3.12 shows the deposited horizontal wall, several obvious humps are seen in test 5 and 6. In GMAW welding, a discontinuous deposit is produced if the TS exceeds the limit that causes insufficient material to be deposited. Gomez Ortega, et al. [109] explains the frequency of drop deposit becomes insufficient to sustain the molten metal volume.

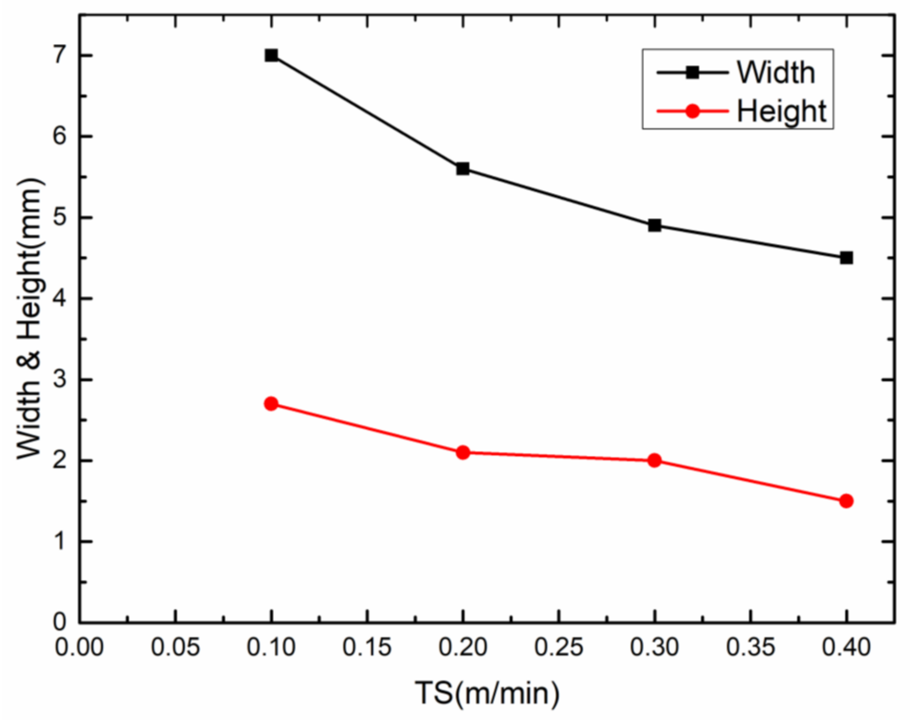

Fig.3. 11 The experimental results of bead width (w) and height (h).

To further investigate the effect of TS on multi-directional WAAM, the control variate method was employed where the volume of deposited material is set to a constant value. The volume of metal V in a unit time can be calculated as:

$$V = \frac{\pi\left(\frac{d}{2}\right)^2 WFS}{TS} \tag{3.5}$$

where d is the diameter of the welding wire. WFS/TS is the deposition ratio that determines the material volume deposited during welding. To ensure the same heat input and volume of material is deposited in each bead, the deposition ratio WFS/TS was set to 10. The TS was varied from 0.1m/min to 0.6m/min, and the WFS was adjusted accordingly. Fig.3.13 shows the deposited thin-wall and welding parameters for each test. The intermittent sphere-shaped welds, instead of continuous homogeneous beads, can be observed when the TS is more than 0.3m/min. This kind of welding defect is known as humping. It commonly occurs in the high-speed welding [69] and expresses itself by the formation of humps and valleys that prevent further weld deposition.

Table 3. 4 Welding parameters and settings of the third test group.

Index	BD	WFS (m/min)	TS (m/min)	w (mm)	h (mm)	Geometry
1	Horizontal	4	0.05	-	-	Irregular
2	Horizontal	4	0.1	7.0	2.7	Acceptable
3	Horizontal	4	0.2	5.6	2.1	Good
4	Horizontal	4	0.3	4.9	2.0	Good
5	Horizontal	4	0.4	4.5	1.5	Acceptable
6	Horizontal	4	0.5	-	-	Irregular
7	Horizontal	4	0.6	-	-	Irregular

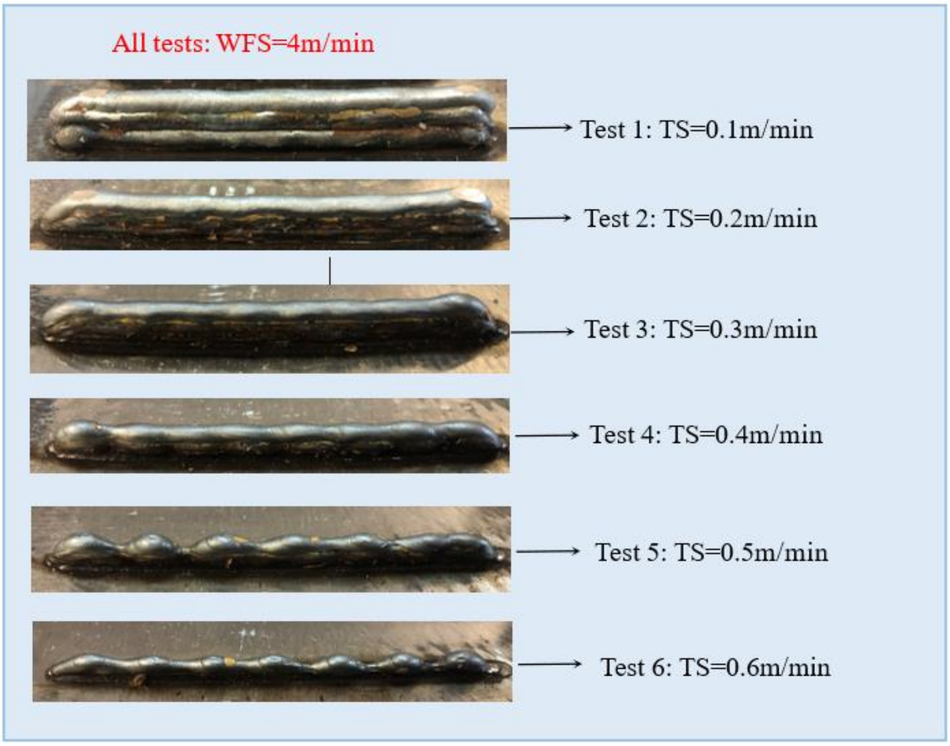

Fig.3. 12 Geometry appearance of thin-walled parts under different TSs.

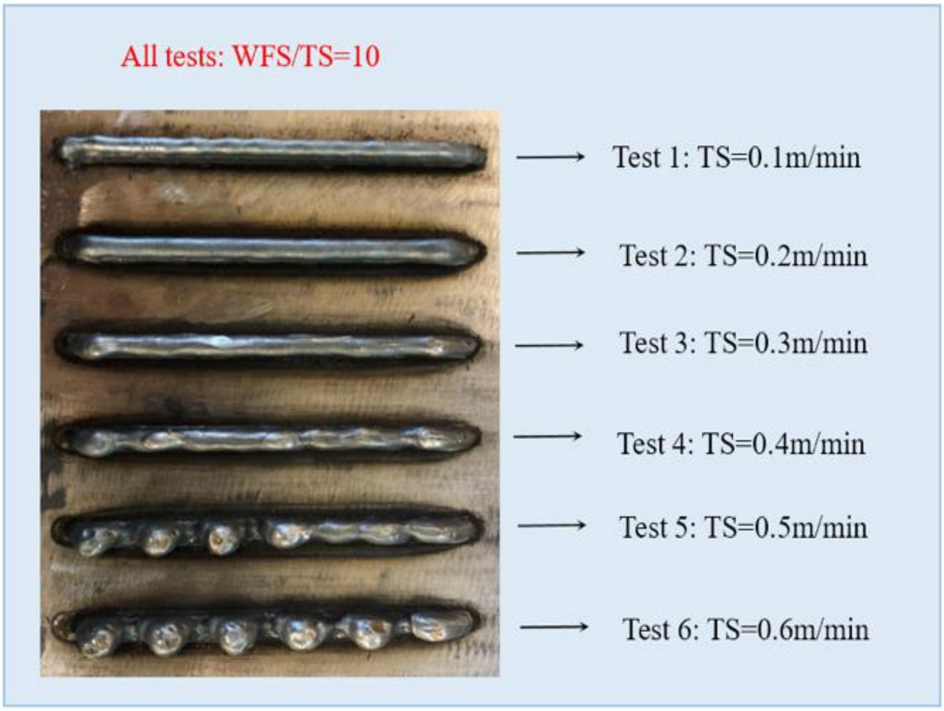

Fig.3. 13 Geometry appearance of thin-walled parts under different TSs while WFS/TS is constant.

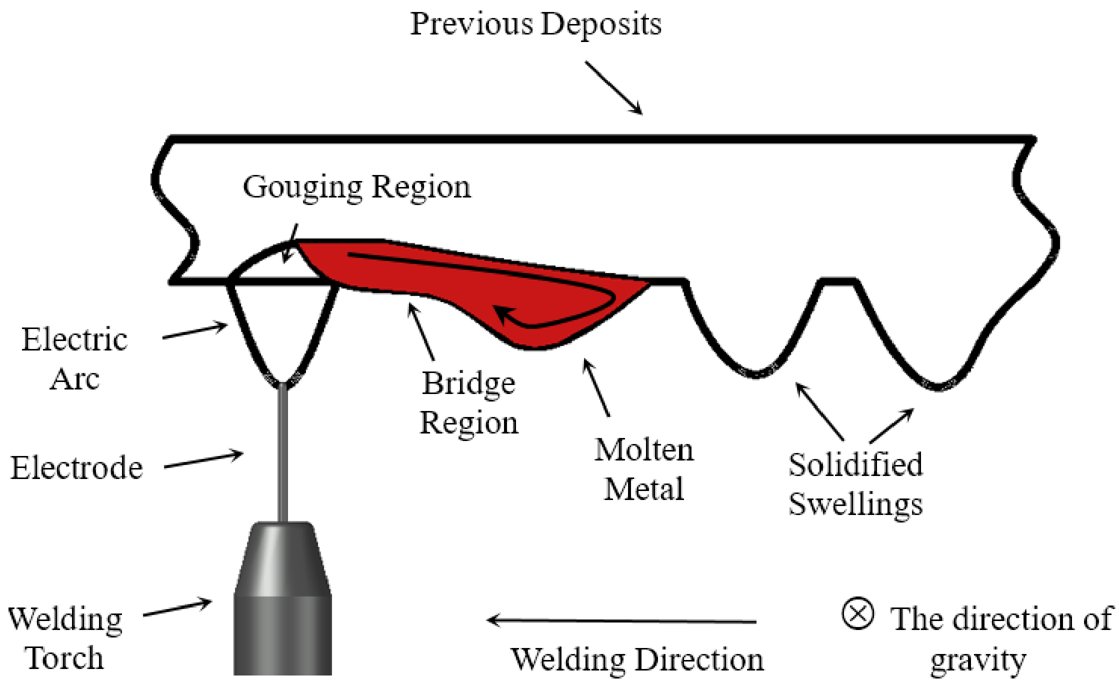

Fig.3. 14 Schematic representation of the forming mechanism of humping issue.

Fig.3.14 illustrates the mechanism of the humping phenomenon. Under the arc pressure and the impact force of the molten filler electrode, a gouging molten pool region is created on the base metal. Meanwhile, the molten metal, combining filler wire and substrate materials, continuously flows from the welding pool underneath the wire electrode to the rear of the welding pool. With a proper TS, the molten metal backfills the weld pool. At a high travel speed, the electrode is always located at the leading edge of the weld pool, resulting in the premature solidification in the bridge region. With the fall in temperature, 'swelling' of the bead is formed due to the isolation of the molten metal in the tail portions. Thus, both the deposit geometry and productivity should be considered when determines a suitable TS in multi-directional WAAM to avoid the humping issue.

3.4.3 Effect of NTWD

Table 3. 5 Welding parameters and settings of forth testing group.

Index	NTWD(mm)	WFS (m/min)	TS (m/min)	I_m(A)	V_m (V)	HI (J/mm)
1	5	5	0.1	98	9.7	7.60
2	9	5	0.1	100	10.5	8.40
3	13	5	0.1	102	11.3	9.22
4	17	5	0.1	102	12.0	9.80
5	21	5	0.1	100	12.7	10.16

To investigate the effect of NTWD on positional welding, other process parameters were set to constant values (the WFS was 6m/min and the TS was 0.1m/min). NTWD varied from 5mm to 21mm. All the process parameters, including NTWD, WFS, TS, electric current (I_m), voltage (V_m), and calculated heat input (HI), are shown in Table 3.5. The heat input was calculated by the instantaneous power determined by averaging the product of current and voltage measurements made over time at rapid intervals. According to Cong, et al. [110] The heat input P is expressed as the formula:

$$P = \eta(\sum U_i I_i)/TS \tag{3.6}$$

where U_i and I_i are the arc voltage and current for each transient welding period, respectively. TS is the travel speed of the robot-torch system. η is the arc thermal efficiency of CMT, Cong, et al. [13] assumed it as 0.8. The nominal calculated heat input is used for comparison among each deposition. NTWD can be divided into two segments, electrode stick-out and arc length, as shown in Fig.3.15. The electrical stick-out is the length from the nozzle tip to the unmelted electrode end. The arc length is the distance between the substrate material and the tip of the wire electrode.

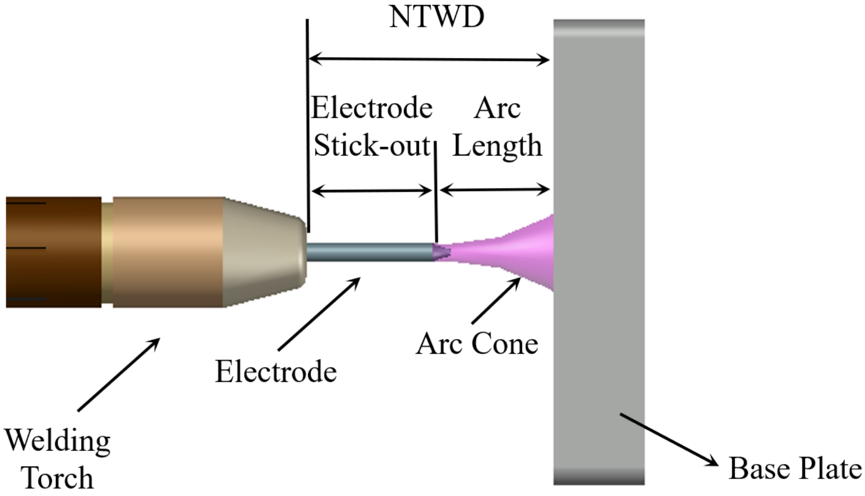

Fig.3. 15 The representation of NTWD, electrode stick-out, and arc length.

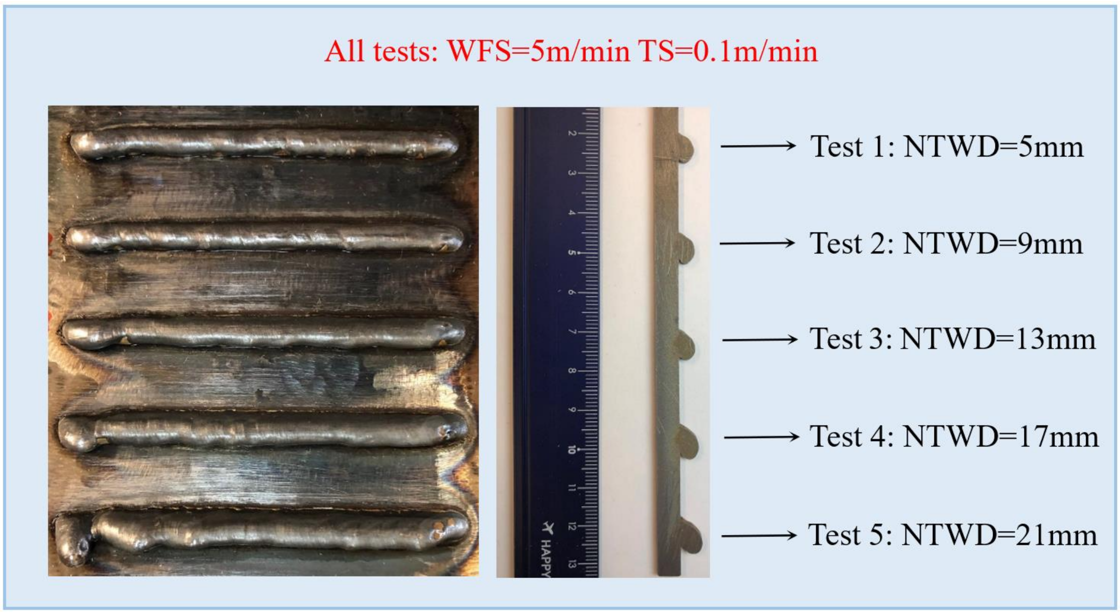

Fig.3. 16 The appearance of weld bead geometries and their cross-section with NTWD varied from 5 to 21 mm.

Fig.3.16 shows the appearance of weld bead geometry and reveals deterioration of the weld bead geometry with an increase in NTWD. Fig.3.16 also includes the cross-section of the deposits. Here, the bead profiles show that the molten metal sagged with excessive NTWD during the deposition process. This resulted in the irregular bead geometry and the prevention of further deposition. The mean welding current and voltage information was obtained and recorded by the built-in sensor in the welding power source. It can be seen that the voltage grows with an increase in NTWD whilst the welding current almost remains constant, as shown in Table 3.5. In this case, the surface tension force decreases with the increase of heat input (Fig.3.17) and is thus the main reason for bead geometry deterioration. To fully understand this phenomenon, it is necessary to investigate the relationship between NTWD and welding voltage in CMT welding.

When conducting GMAW welding in spay mode, the arc length changes with the voltage variation. Usually, a constant voltage power source is used to maintain a stable arc. The situation is different in CMT welding, where the arc length is detected and mechanically adjusted to a predefined length regardless of the initial distance between the nozzle tip and the surface of the part. In practice, the arc must remain relatively short (2–3 mm) to maintain a regular and high dip frequency [24]. According to Ohm’s law in equation (3.7), the current (I) through total electrical resistance (R) is directly proportional to the voltage (V) across the resistance.

$$\mathrm{I} = \frac{V}{R} \tag{3.7}$$

Generally, the electrical resistance of the stick-out resistance depends on the electrode diameter/cross-sectional area, electrode resistivity, and the length of the extension [24].

As shown in Fig.3.15, the increase in NTWD has an associated increase in electrode stick-out length as the arc length remains stable. Greater resistance to the flow of electricity through the electrode extension is generated due to the expanded conductor length. Although the control algorithm of CMT is complex, to retain a constant welding current, welding voltage is adjusted automatically by the power source. Therefore, it is imperative to keep a short length of NTWD for better quality in multi-directional WAAM.

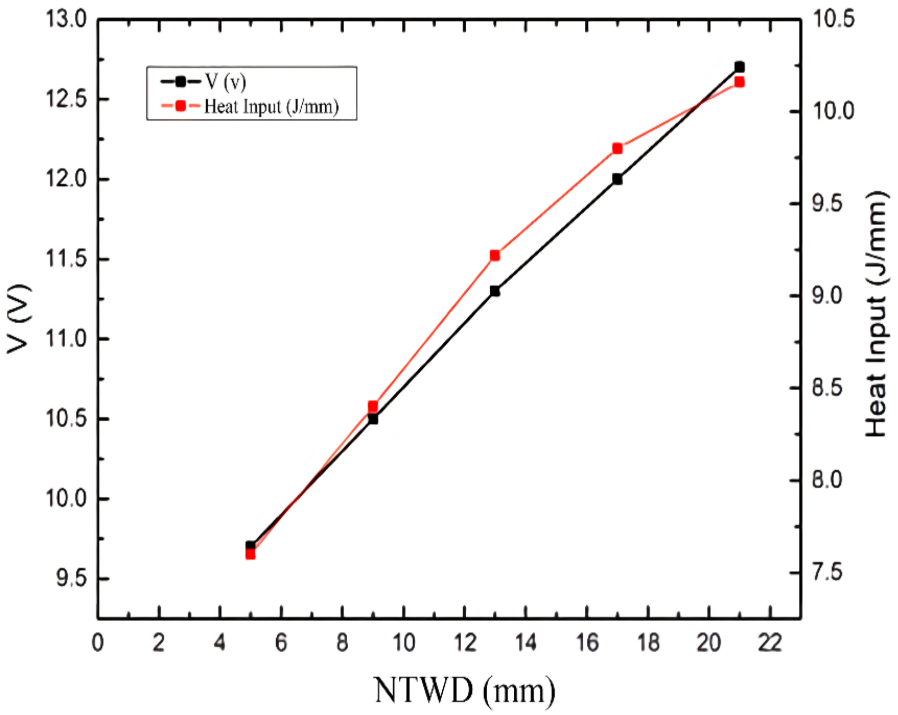

Fig.3. 17 Welding voltage and heat input with NTWD varied from 5 to 21 mm.

3.4.4 Effect of torch angle

The angle between the welding torch and the base is defined as the troch angle or welding angle in welding process, as shown in Fig.3.19. Typically, the torch angle is maintained perpendicular to the direction of wall building in WAAM. If the angle changes, the geometry of the deposit may vary due to the different force model. To identify an optimized torch angle, varying welding torch angles were set at 45°, 60°, 75°, and 90° for each test, whilst all other process parameters were kept constant, as presented in Fig.3.18. Note that the NTWD was set to 18 mm due to the reachability of torch for acute angles. The bead geometries and cross-section of each weld is presented in Fig.3.18. The experimental results reveal that the molten metal sags less with a smaller torch angle in the solidification process - meaning a better bead geometry is produced with a small torch angle.

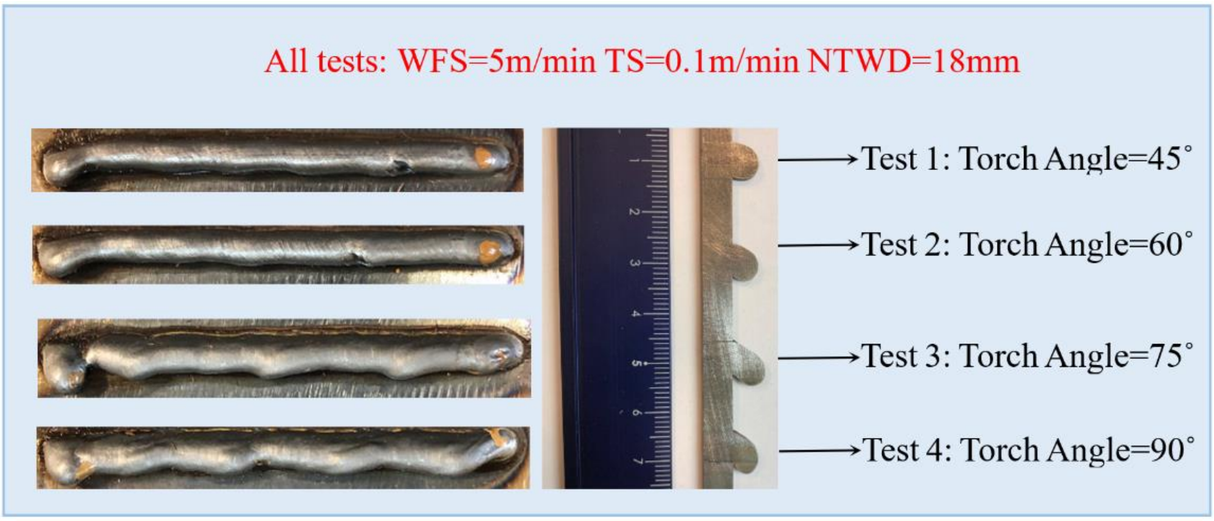

Fig.3. 18 The appearance of weld beads geometries and their cross-section with welding torch angle varied from 45° to 90°.

To explain this, an updated force model was created for a torch angle at 45°, as demonstrated in Fig.3.19. The arc pressure f_{arc}, with the inclined angle of 45°, is applied on the molten metal. Instead of sagging downward, the molten metal tends to flow upward at the beginning of the solidification process. In the vertical direction, the molten metal flows upward and then downward to suppress the sagging tendency of the weld bead. Thus, with the upward torch inclination angle, the arc force assists to improve the molten metal stability and subsequently improve the bead geometry shape.

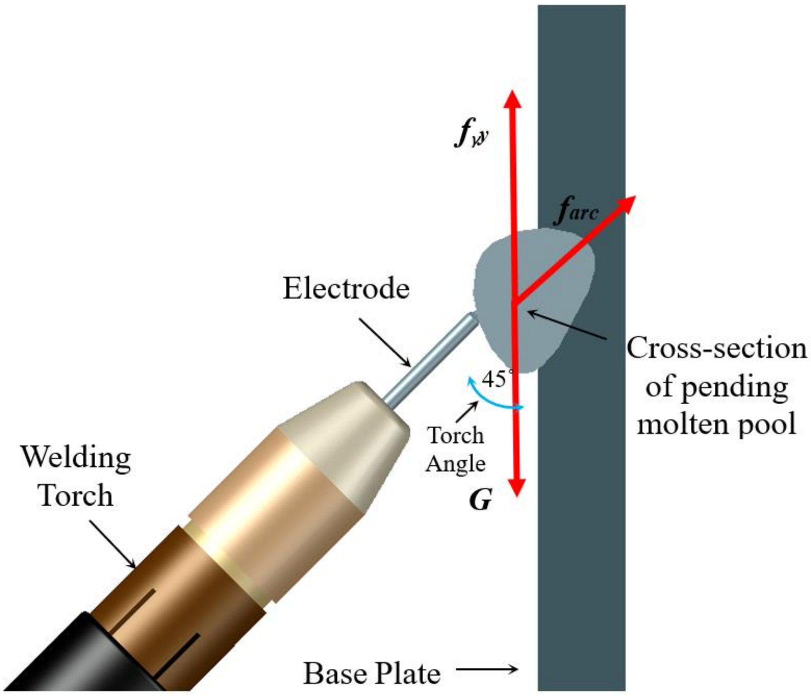

Fig.3. 19 A modified force model for a pendent molten pool with welding torch angle at 45 ˚.

3.5 Case studies

To further verify the performance of the proposed strategy, three scenarios were used to fabricate parts with more complicated features and compared to the experiments from previous sections. For comparative reasons, the filler material, shielding gas, base plate, and the robotic welding system utilized in previous sections were kept the same for these case studies.

Fig.3.20 presents a 3D model of a part with an overhang structure, coloured in red. To examine the capability of depositing an inclined wall from 0˚ to 90˚, a thin quadrant wall was designed. In the deposition process, the vertical wall was firstly deposited as a substrate, with WFS and TS set at 5m/min and 0.3m/min, respectively. The process parameters were changed to WFS 1m/min and TS 0.1m/min for depositing the thin quadrant wall. The torch angle was varied accordingly so that it was parallel to the growth direction of each layer. NTWD was kept constant at 8 mm. The start of the bead alternated at each end after every deposit. Fig.3.20 also shows the final product, with a total of 32 layers deposited successfully. It demonstrates that the proposed multi-directional WAAM strategy is capable of fabricating an inclined wall from 0 to 90 degrees with proper welding settings.

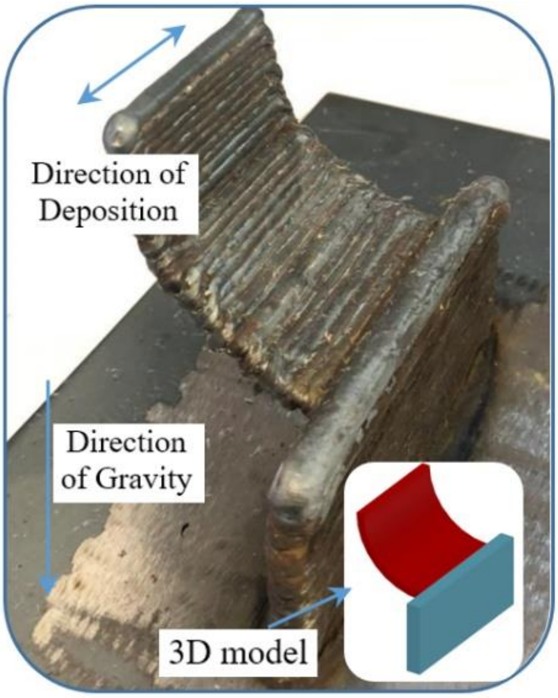

Fig.3. 20 3D model of the first sample and Deposited near-net shape.

In the second case study, the multi-directional WAAM was used to fabricate a cylinder horizontally, with the 3D model shown in Fig.3.21. Firstly, a vertical wall was produced with the WFS and TS set to 5m/min and 0.3m/min, respectively. Process parameters for the horizontal cylinder were WFS 2m/min and TS 0.3m/min. The torch angle was set to 90˚, and the NTWD was set to 8 mm. In the deposition process, the start point was selected randomly, and the welding direction (anticlockwise or clockwise) was alternated for each layer to minimise uneven joint height. A 30-layered thin-walled cylinder with an overhang feature is shown in Fig.3.21. As a result of the new strategies used, the appearance and the profile of the thin-walled cylinder is reasonably good, and the whole deposition process was quite stable. It also demonstrates the proposed multi-directional WAAM strategy is capable of depositing at any angle on the vertical surface, from horizontal to vertical.

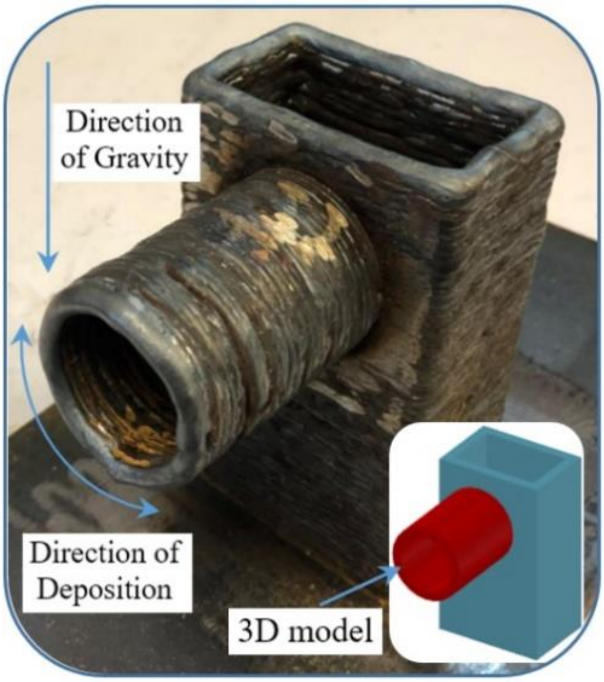

Fig.3. 21 3D model of the second case study and Deposited near-net shape.

In the third case, multi-directional WAAW was used to fabricate a horizontal wall on a curved surface, with the 3D model shown in Fig.3.22. Typically, in practice with the WAAM, the welding surface is not a flat surface. This case is designed to examine the performance of multi-directional WAAM that used to deposit on an irregular surface. In the deposition process, a thin-walled cylinder was built up vertically to create a curved surface, the WFS and TS were set to 2m/min and 0.1m/min, respectively. Subsequently, WFS and TS were changed to 1m/min and 0.1m/min. The torch angle was controlled to be perpendicular to the tangent line curved surface at all times. The start of the deposit alternated of each layer. A total of 35 layers were deposited horizontally resulting in a satisfactory flat surface, as shown in Fig.3.22.

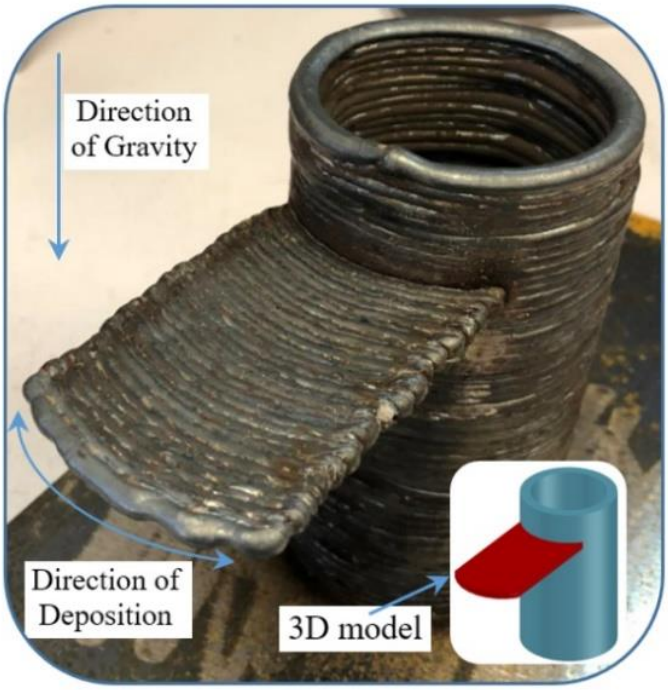

Fig.3. 22 3D model of the third sample and Deposited near-net shape.

3.6 Chapter summary

This chapter focused on a new strategy of fabricating parts with overhangs using the multi-directional WAAM. Due to the negative impact of gravitational force, it is difficult to transfer the molten droplet to the target position and form a regular bead geometry in the multi-directional deposition process. To achieve a stable deposition process, the forming mechanism of positional deposits is initially investigated. Based on the analysis, GMAW using the CMT technology was selected for the multi-directional WAAM process due to its excellent position accuracy and ability to reduce the system heat input. Subsequently, the effects of the main process parameters on positional deposition were studied and are as follows:

1) Bead geometry deteriorates with an increase in WFS due to the combined effects of reduced surface tension force, longer metal freezing time, and increased weld bead volume. However, surface quality can be improved with the increase of WFS up to 2m/min.

2) Welding torch travel speed affects the multi-directional WAAM deposition from two aspects: firstly, a discontinuous bead geometry forms with a high TS due to the insufficient material deposited. Secondly, the process stability is largely dependent on torch TS due to the humping issue. A low TS is helpful to avoid humped bead geometry.

3) In CMT welding, the voltage increases with the elongation of NTWD due to the automatic control algorithm of CMT welding power source. Thus, a shorter NTWD is recommended to reduce the heat input and prevents molten pool sagging.

4) Arc force is beneficial of improving bead geometry. The experimental results showed a suppressed sagging tendency of the molten metal when adjusting the welding torch angle.

Employing this knowledge, three samples were built to demonstrate the effectiveness and versatility of the proposed multi-directional WAAM process control strategy. Finally, practical guidelines for process control in multi-directional WAAM were summarised and provided for practical use. The proposed multi-directional WAAM method provides a new solution for fabricating overhangs without extra support and presents better process economy and time efficiency compared to the standard WAAM.

Chapter 4

Welding defect investigation and avoidance

4.1 Introduction

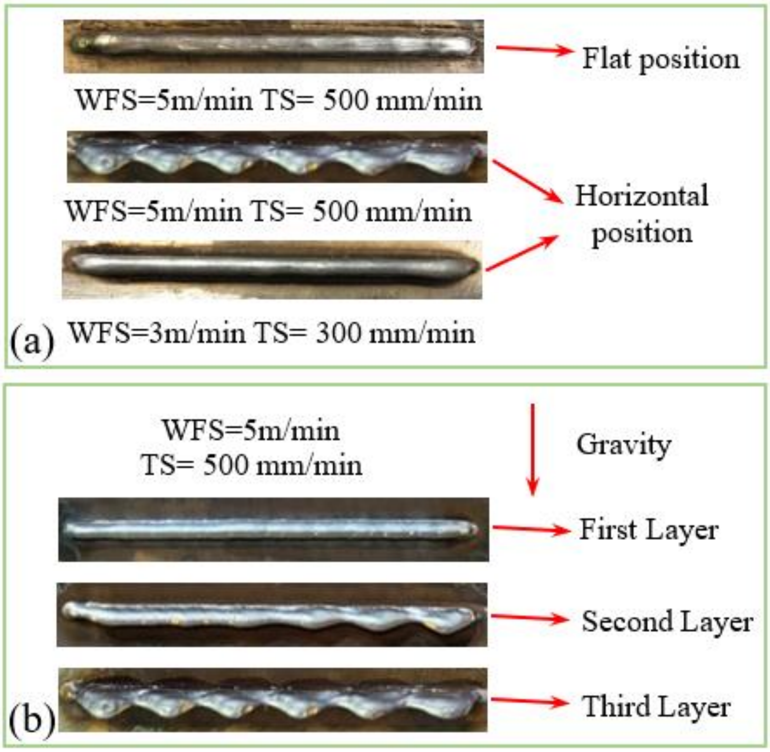

Fig.4. 1 The sagged weld bead in positional deposition.

In the positional deposition process, it was found that the humped weld bead formed when depositing in an unsupported horizontal position [34]. As shown in Fig.4.1(a), for horizontal deposition, a relatively high welding speed may result in a humped weld bead, while a good weld bead forms using the same welding parameters in the flat position. It can also be seen that the humping is suppressed with a decreased welding speed, which means that the occurrence of humping restricts the useful welding process parameter range in the positional deposition. In addition, multiple layers are required to construct a dimensional feature using the GMAW-based WAAM [111]. After depositing several layers, the severity of the humped weld becomes unacceptable, and the process stability for further deposition is significantly affected. Fig.4.1(b) demonstrates the first, second, and third layer of a thin-walled part deposited in the horizontal build direction using the CMT welding process. It can be seen that humping appears, and the bead geometry deteriorates for each successive layer, indicating that the multi-layered process has limited positional capability.

As previously mentioned, the formation of humping is a typical weld defect in conventional fusion welding processes, particularly when high travel speeds are used [79]. According to Nguyen, et al. [55], humping can be described as the series of periodic undulation of the weld bead. Over the last 35 years, a considerable amount of literature has been published on the humping phenomenon in conventional downhand welding [56]. Studies have covered several different welding processes, such as GMAW [57], GTAW [58] [59] [60] [61], laser welding [62] [63] [64] [65], electron beam [66] [67], and submerged arc welding (SAW) [68]. Bradstreet [11] reported the mechanism of humped welds using plain carbon steel in the GMAW process. He suggested that the defect was produced by surface tension force and fluid flow patterns during GMAW. Mendez [58] [59] proposed a forehand technique to enhance productivity in the GTAW process. To avoid humping occurrence, the welding torch can be rotated according to the established model. In such way, the plasma jet has a velocity component in the direction of motion of the torch. For laser welding, weld pool dynamic behaviours were investigated to gain a better understanding of humping in the study by Ai, et al. [63]; the experimental results demonstrated that humping is related to the combination of tilted angle of the keyhole, narrow and long molten pool and collision of fluid flow.

While current studies provide useful information on the humping phenomena in downhand welding process, they are not directly relevant to humping formation in the multi-layer multi-directional WAAM process. This chapter aims to investigate the humping phenomenon during multi-layer multi-directional WAAM using GMAW/CMT welding. Related works on humping formation in GMAW process was briefly reviewed. From this, the mechanism of humping phenomenon was analysed for welding in the horizontal position. Based on observing the molten pool behaviour, the proposed humping mechanism was validated for welding different process parameters in different positions. Several guidelines were proposed in order to avoid humping for the multi-layer multi-directional WAAM process.

4.2 Theoretical analysis of humping formation

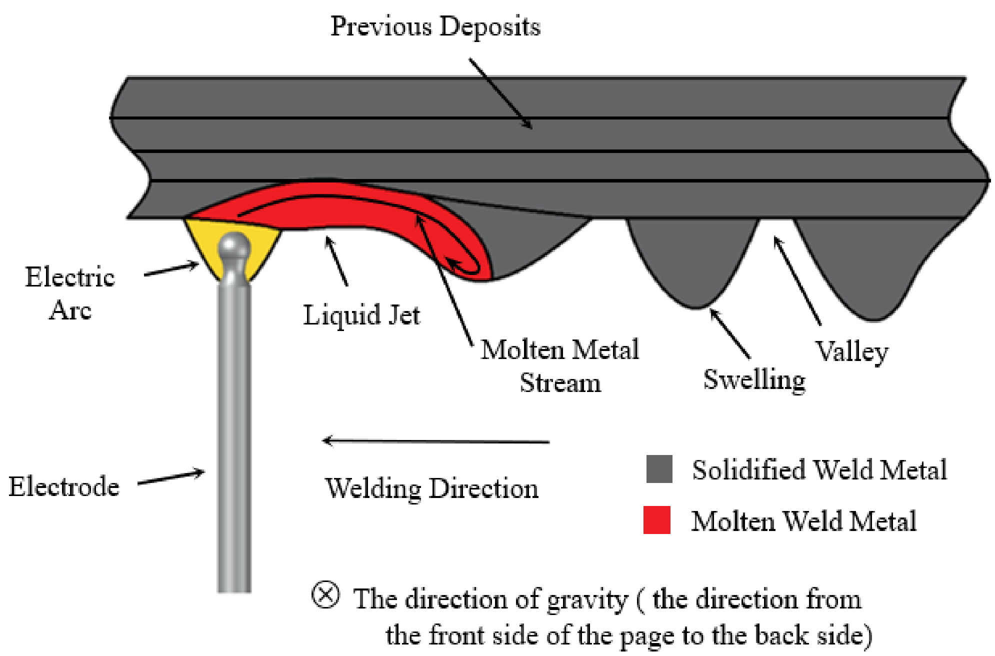

Fig.4. 2 A schematic diagram of humping phenomenon (side-view).

To further assist the analysis of the humping formation in multi-directional WAAM process, several terms of a typical metal flow based humping model are first explained. As shown in Fig.4.2, a schematic diagram is provided to illustrate the longitudinal section along the centreline of a humped weld bead in a horizontal position (the direction of gravity from the front side of the paper to the backside). The metal streamflow is created under the arc pressure, the stream continues to flow to the rear of the molten pool. The term 'liquid jet' is used to describe the metal stream flowing from underneath the electrode towards the rear of the weld pool. At the tail of the molten pool, 'swelling' appears with the accumulation of molten weld metal, and the humped weld bead forms after this hump completely solidifies. In addition, a portion of the liquid jet may become the 'valley' between adjacent humps.

During the deposition process, the molten droplet fuses into the weld pool with the forward motion of the wire electrode. Then, the wire back-drawing force and surface tension force assists the liquid bridge fracture and the metal transfer takes place when the droplet detaches from wire electrode [5]. With the high frequency of the droplet detachment, strong molten metal flow is formed from the forepart to the rear of the weld pool. The momentum of the fluid stream is mainly affected by arc pressure, electromagnetic force, and Marangoni force (a variant surface tension force). The weld pool surface in the arc cone region is depressed by the arc pressure force, which can be expressed as in (4.1) [112],

$$F_{arc} = \frac{\mu I^2}{8\pi}\left[1 + 2ln\left(\frac{R_2}{R_1}\right)\right] \tag{4.1}$$

where μ is the magnetic vacuum permeability, I mean welding current, R_1 and R_2 are the radiuses of the arc cone at the weld electrode and the previous layers, respectively. The arc pressure force increases greatly with a higher arc current.

As widely reported in [113-115], Marangoni force is one of the major driving forces of the metal convection in the weld pool. Marangoni force can be defined as a kind of surface tension force that drives the flow of the molten metal stream away from low surface tension area to the high surface tension area. The surface tension coefficient γ is considered to vary linearly with the temperature T, which is given by [32]:

$$\gamma = \gamma_m^0 - A_s(T - T_m) \tag{4.2}$$

where γ_m^0 is the surface tension coefficient of pure metal at the melting point, which is constant for filler material. T_m is the melting point of the filler material. A_s can be calculated as the negative of $\partial\gamma/\partial T$ for pure metal, which is also considered as a constant when the temperature is much greater than the melting point [116]. Since the surface tension is considered a temperature dependent coefficient, the surface tension gradient can be associated with the temperature gradient of the weld pool [115]. Thus, the metal stream flows from the high temperature region to the relatively low temperature region. In the welding process, the weld pool underneath the weld arc has the lower surface tension with the higher temperature, when compared to the tail of the weld pool. The momentum of the metal flow has been increased by the Marangoni force, which can be expressed as in (4.3) [80].

$$F_M = \frac{\partial\gamma}{\partial T}\frac{\partial T}{\partial \vec{S}} \tag{4.3}$$

where $\vec{S}$ is the vector tangential to the target molten pool surface.

With a high welding speed, the weld pool enlarges, and the temperature differences between the front and tail of the metal pool increases, resulting in a large Marangoni force and therefore increased momentum of the metal flow. This was confirmed in the studies of Wang, et al. [72] and Berger, et al. [117], where the mean velocity of the weld metal flow increases with a high welding speed. Thus, the metal stream with a high momentum keeps flowing backward, and the humping forms at the tail of the molten pool. Meanwhile, since the welding torch continues to move forward at a relatively high travel speed, an elongated liquid metal jet appears between the wire electrode and the humping. Finally, since the heat source continues to move in the welding direction, the metal flow is prevented from transferring backward to the swelling region until a portion of liquid jet solidified. The previous swelling stops growing up and a new humping starts forming. Thus, the strong molten metal flow with a high momentum is responsible for the humping formation in high speed welding.

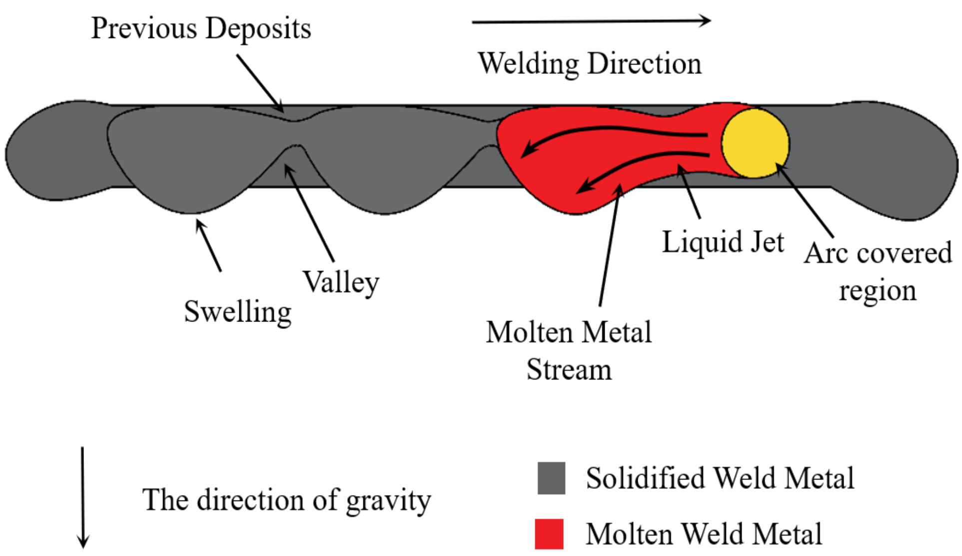

Fig.4. 3 A schematic diagram of humping phenomenon (top-view).

In addition, as show in Fig.4.1, the sagged weld bead shape indicates that the downward flow of the molten metal, induced by the gravitational force, may be another driving factor of the humping in the positional deposition. A schematic diagram of metal flow is given in Fig.4.3 to illustrate the top-view of a humped weld bead in a horizontal position. In downhand welding, it is obvious that the gravitational force helps to suppress the accumulation of weld metal [78]. However, the effect of gravitational force is different in the positional deposition, instead of driving the molten metal to backfill the gouging area, the metal flow trends downward as shown in Fig.4.3. The momentum of the backward stream of molten weld metal has been increased greatly by the influence of gravity, resulting in a poor positional capability of multi-directional WAAM.

4.3 Experimental details

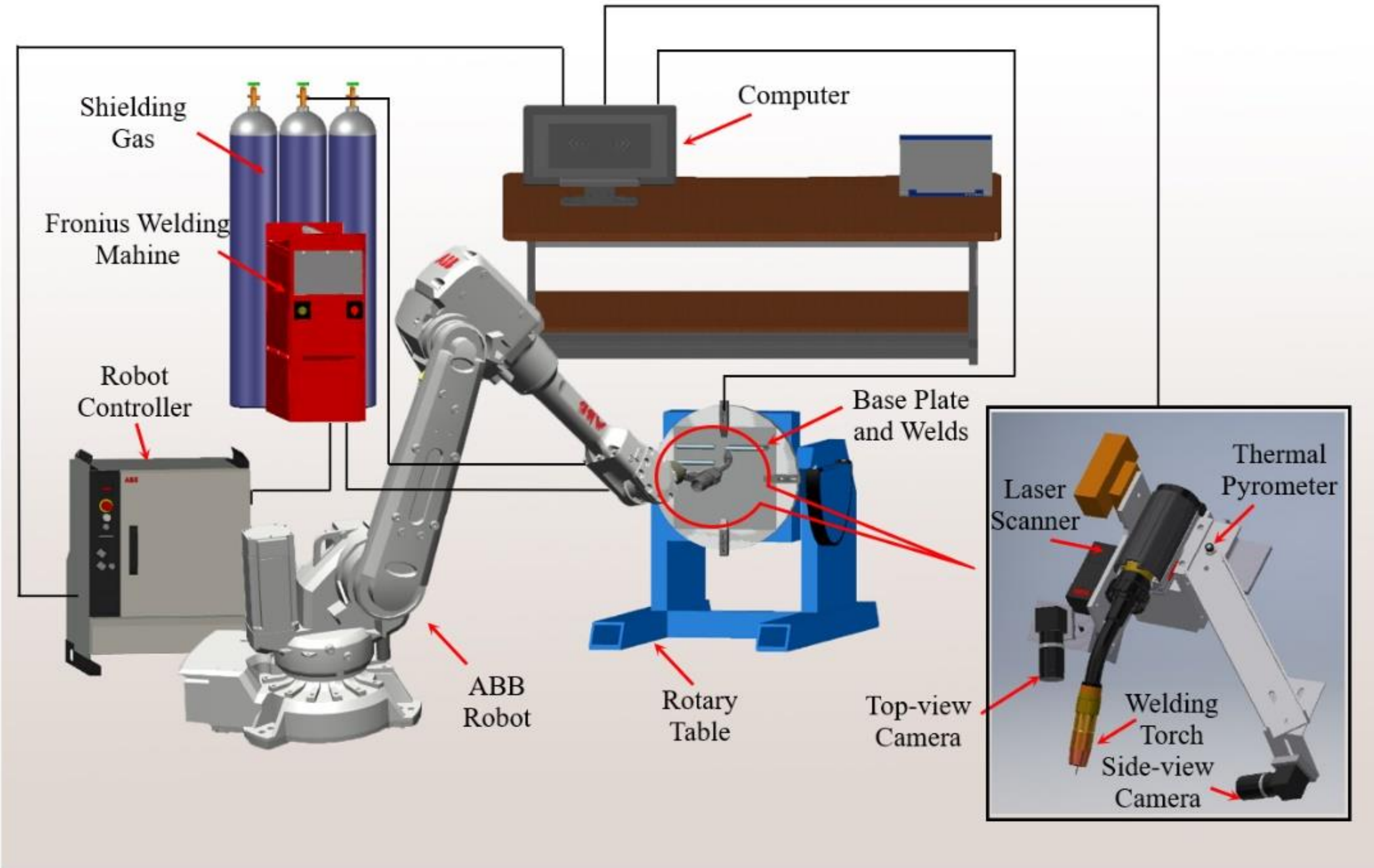

Fig.4. 4 The experimental setup.

Fig.4.4 presents the setup of the robotic WAAM system for the investigation of humping issue in a positional deposition. Its main components include a 6-axis ABB industrial robot with a positioner, a Fronius TPS 4000 CMT Advanced welding unit, a personal computer, two CCD cameras, an infrared pyrometer, and a laser scanner.

4.3.1 The robotic WAAM system

In this study, the ABB IRB 2600 industrial robot with six Degrees of Freedom (DoF) was used to hold the welding torch. A two-DoF workpiece positioner was employed to keep base plate vertical for the positional deposition. The Fronius CMT Advanced 4000 welding machine was used as a welding power supply. It consists of a welding controller and power source, coupled to a CMT wire feeder, and the welding torch. The controller of the welding power source is interfaced with the robot controller. The motion of the wire feeder can be adjusted on the robot. The RobotStudio (simulation and programming software for the ABB robot) was used to program the torch motion and coordinate the weld settings. Two CCD cameras were mounted on the welding torch to capture the molten pool formation behaviour. A structured light laser scanner was integrated into the robotic welding system to measure the height of the multi-layer thin-walled structure for updating the robot path. In addition, an infrared pyrometer was used to monitor the inter-pass temperature. A data acquisition unit and a personal computer serve as the master control for the welding machine, robot, positioner, camera, and laser scanner.

4.3.2 Monitoring methodology for the CMT process

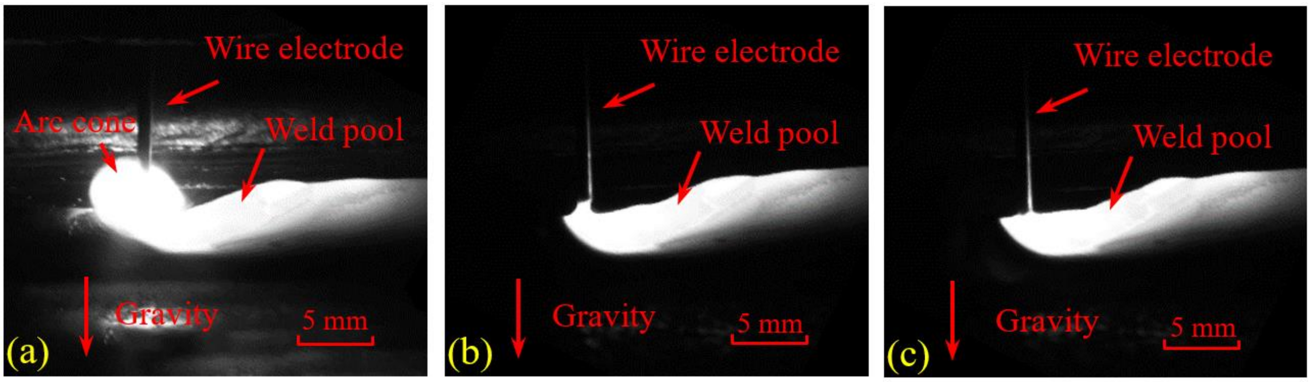

Fig.4. 5 Three steps of CMT welding (a) metal melting, (b) waiting, and (c) short-circuiting.

As shown in Fig.4.4, the vision system includes two CCD cameras mounted on the robotic arm to capture the side-view and the top-view of the weld bead separately. In addition, Fig.4.5 demonstrates the basic concept of CMT process, the detailed metal transfer process can be divided into three steps; 1) the metal melting phase Fig.4.5(a), 2) the background current phase/wait phase Fig.4.5(b), and 3) the short-circuiting phase Fig.4.5(c) [118]. In the metal melting phase, it is hard to observe the profile of the molten pool due to the illumination of the arc core when electrical arc forms. Thus, the weld pool images were presented during the waiting phase or short-circuiting phase. In addition, the forming weld pool is white in all the presented images, indicating a high temperature.

4.3.3 Materials and welding setups

This work used plain carbon steel ER70S-6 filler wire 0.9 mm in diameter for the feedstock. The experimental trials were implemented on base plates of Q235 with the dimensions of

150×150×10 mm. To eliminate the oxide layer and impurities on the surface, the substrate plates were ground before welding. The chemical composition of the ER70S-6 welding wire and Q235 plates are given in Table 4.1. The welding gas Argoshield (Gas code 566, BOC Gases Australia Ltd, Sydney, Australia) consists of 20% Carbon Dioxide and 80% Argon was used at a constant flow rate of 25 L/min.

Table 4. 1 ER70S-6 and Q235 Chemical compositions & ranges (wt.%).

Alloy	C	Mn	Si	Cu	S	P	Fe
ER70S-6	0.08	1.53	0.88	0.18	0.01	0.009	Bal
Q235	≤0.17	0.35-0.80	≤0.35	-	≤0.40	≤0.35	Bal

In this study, the welding system was a Fronius TPS 4000 CMT Advanced unit. With this system, the welding current and voltage are automatically selected based on the wire feed speed, using a synergic algorithm embedded in the Fronius welder. The arc length correction was set to -5% to have a most flat weld bead [119]. The rest of welding parameters were set to the system optimal regarding different filler material, which can be found in [120].

4.3.4 Experimental design

To investigate the humping formation under different welding settings during multi-layer multi-directional WAAM, the influence of CMT welding variables, Wire Feed Speed (*WFS*) and Travel Speed (*TS*), and welding position were examined by depositing a ten-layer 100 mm thin-walled structure. In addition, the base plates were orientated vertically, so that the welding torch is perpendicular to the base plate as shown in Fig.4.6.

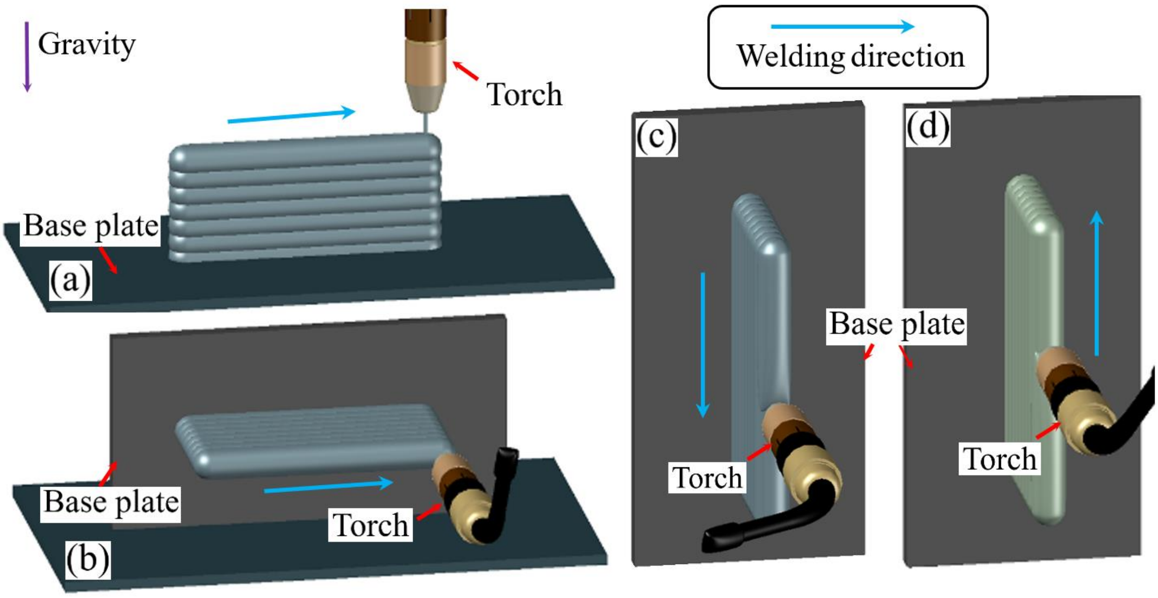

Fig.4. 6 The different deposition positions (a) downhand (flat), (b) horizontal, (c) vertical-down, and (d) vertical-up.

The experiments are divided into three subsections with five groups of tests, as shown in Table 4.2. Fig.4.6 demonstrates the deposition positions, including downhand(a), horizontal(b), vertical-down(c) and vertical-up(d). Firstly, based on the observation of molten pool behaviour, the presented mechanism of humping formation was validated through depositing horizontal walls in test 1 group A. Besides, another trial in downhand position was conducted for comparison. Secondly, the effect of *WFS* and *TS* on humping formation were investigated thorough the tests in group B and C, respectively. Finally, in the practical

WAAM process, the deposition path may be designed along multiple directions rather than just horizontally, and therefore the effects of gravitational force on metal flow may be different. A set of thin-walled structures in vertical-down (group D) and vertical-up (group E)

Table 4. 2 The design of five experiment groups.

Index		Welding parameters				Deposition Position	Humping occurrence
Group	Test	WFS (m/min)	TS (mm/min)	Current (A)	Voltage (V)		
A	1	5	500	100	13.8	Horizontal	Yes
	2	5	500	100	13.8	Downhand	No
B	3	1	100	35	12.1	Horizontal	No
	4	2	100	60	13.2	Horizontal	No
	5	3	100	77	13.6	Horizontal	No
	6	4	100	92	13.7	Horizontal	No
	7	5	100	100	13.8	Horizontal	No
C	8	1	100	35	12.1	Horizontal	No
	9	2	200	60	13.2	Horizontal	No
	10	3	300	77	13.6	Horizontal	No
	11	4	400	92	13.7	Horizontal	No
	12	5	500	100	13.8	Horizontal	Yes
D	13	1	100	35	12.1	Vertical-down	No
	14	2	200	60	13.2	Vertical-down	No
	15	3	300	77	13.6	Vertical-down	No
E	16	1	100	35	12.1	Vertical-up	No
	17	2	200	60	13.2	Vertical-up	No
	18	3	300	77	13.6	Vertical-up	Yes

positions were built to examine the impact of different deposition positions on humping occurrence.

4.4 Results and analysis

4.4.1 Validation of the proposed humping mechanism

Fig.4. 7 The side-view of molten pool behaviour (a-f), and bead appearance (g) of test 1 in group A.

To compare the humping formation between downhand and horizontal deposition, two thin-walled parts were deposited using the same process parameters, as *WFS* at 5 m/min, and the TS at 500 mm/min. (Note that humping occurs when TS was increased to 500 mm/min for the second to tenth layer. For the first layer, humped happens only when TS is over 1300 mm/min due to the relatively flat substrate surface). The images of the weld pool were captured to assist the analysis of humping formation during the metal transfer process. In the first test, a thin-walled part was deposited in the horizontal position. Fig.4.7(a) to (e) provides a series of side-view images that illustrate the sequence of events during the horizontal deposition. The variation in brightness of the molten pool makes it possible to distinguish a transitional boundary between the liquid and solidified region. Accordingly, the humping bead formation can be divided into three phases: the molten pool growth phase, the hump formation phase, and the solidification phase. In addition, since the humping is a periodic phenomenon, the start time of a cycle is set to the point when solidification of the previous humping completes.

As shown in Fig.4.7(a), the initial molten pool formed and extended in the molten pool growth phase. Due to the arc force, the molten pool surface underneath the wire electrode was depressed and a strong metal flow was produced. The fluid flow moves backward to the tail of the weld pool with high momentum, resulting in a curved and sloped profile and slight swelling, as shown in Fig.4.7(b). In the second phase, the swelling kept growing with the continuous metal stream flowing towards the rear of the molten pool. Meanwhile, since the welding torch continued to move forward at a relatively high travel speed, an elongated liquid jet appeared between the arc and the hump, as demonstrated in Fig.4.7(c) and (d). Finally, in the solidification phase, while heat source continues to move forward, the weld bead solidifies with the reduction of brightness as can be seen in Fig.4.7(e). Until a portion of liquid jet solidified, the subsequent molten metal was prevented from transferring backward to the swelling region. Despite the fact that a portion of the swelling region was fused, a new cycle of the humping formation begins, as shown in Fig.4.7(f). Therefore, the premature solidification of the liquid jet is a critical factor to explain the periodical feature of the humping formation. Once it solidifies, the previous hump stops growing, and the next swelling begins to take place. The appearance of the deposit with humping is presented in Fig.4.7(g), where the accumulation of the weld metal at the swelling forms the humped weld beads. Meanwhile, several valleys connecting swellings were formed at the positions of the liquid channel.

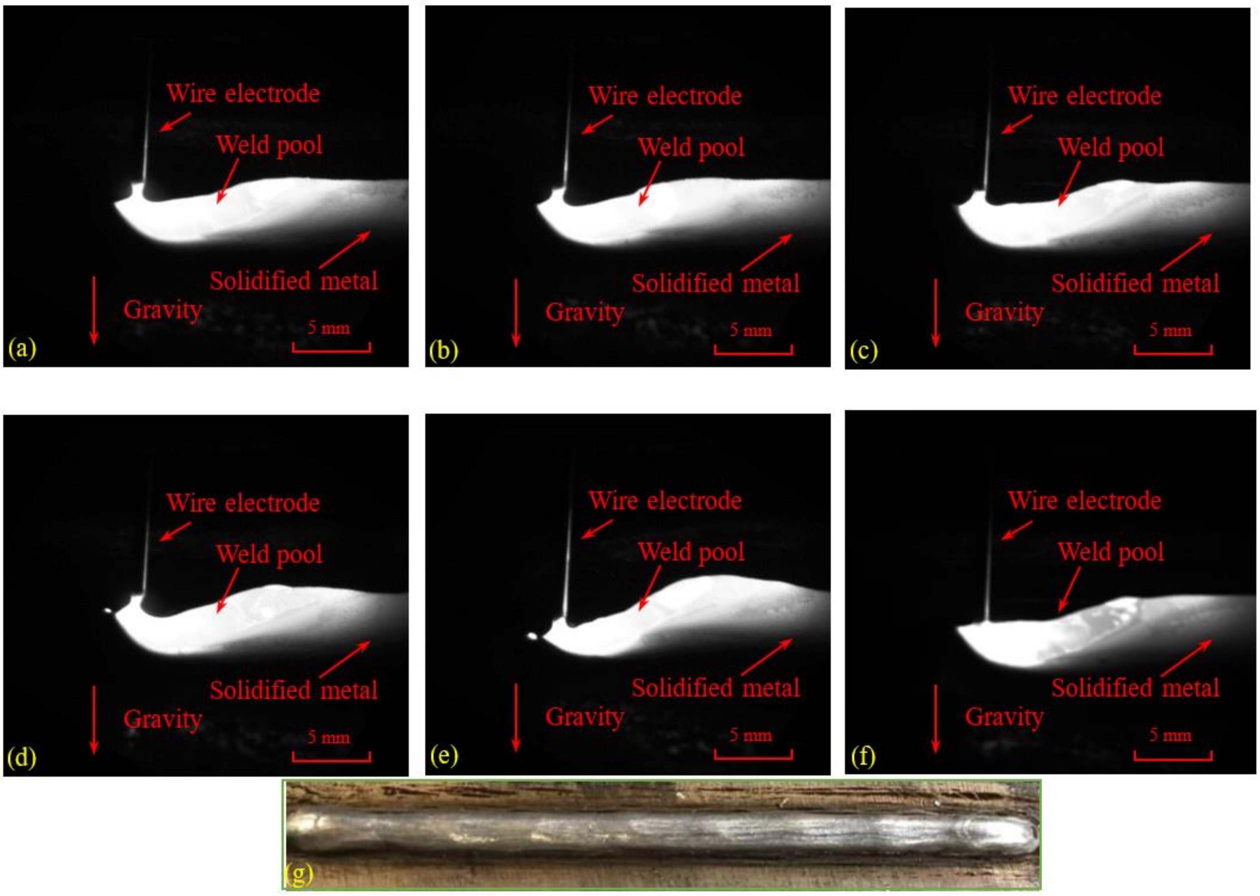

Fig.4. 8 The side-view of molten pool behaviour (a-f), and bead appearance (g) of test 2 in group A.

In the second test of downhand deposition, the entire process was stable, and no humping was observed, as shown in Fig.4.8(g). In addition to the forming appearance of the weld bead, several images of the molten pool were provided in Fig.4.8. Compared to the molten pool profile in swelling formation phase in the horizontal position (demonstrated in Fig.4.7(c) and (d)), the profile of the molten pool is almost homogenous in downhand deposition. It is evident that gravity may help suppress the accumulation of molten metal in downhand position [78], but it may be a negative influence in positional welding.

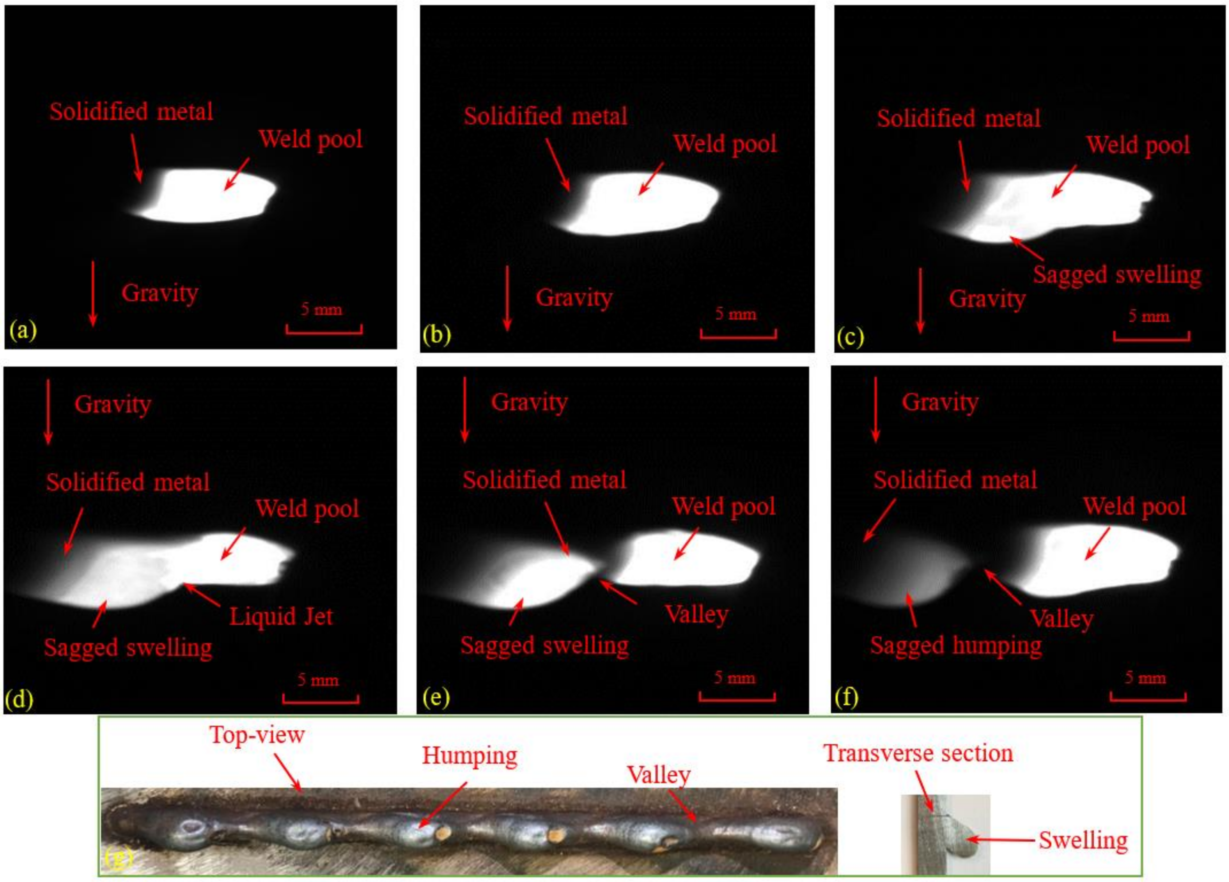

Fig.4. 9 The top-view of molten pool behaviour (a-f), and bead appearance (g) of test 1 in group A.

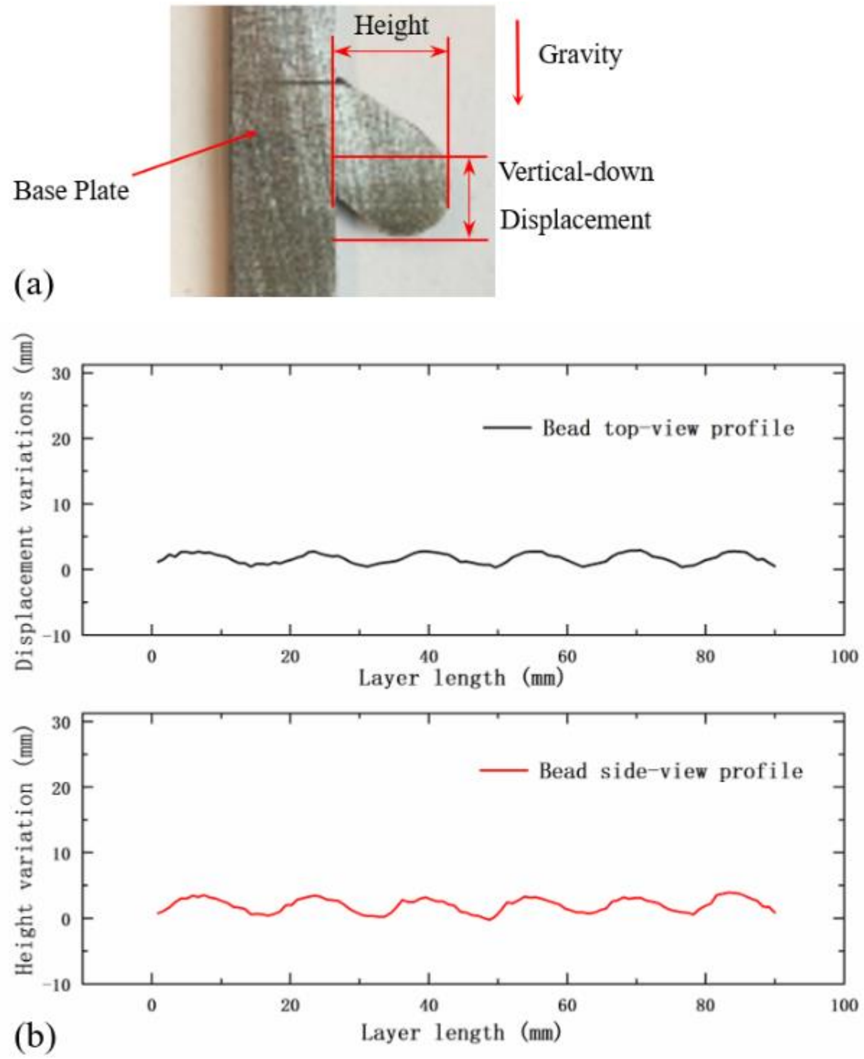

Fig.4. 10 (a) The definitions of bead dimensions, and (b) the height and vertical displacement variations.

To further investigate the behaviour of the metal flow in the horizontal deposition, a group of top-view images of the weld pool, as shown in Fig.4.9, were also captured at the same deposition time as the side-view images in Fig.9. In the molten pool growth phase, the molten pool has a slight tendency to sag downwards, as shown in Fig.4.9(a) and (b). In Fig.4.9(c) and (d), it is illustrated that when the weld metal accumulated at the rear of the weld pool, the height of the layer grew perpendicular to the base metal to form the hump. However, while under the detrimental influence of gravity, the swelling sagged downward. Finally, through the solidification phase, the sagged weld beads were formed, as shown in Fig.4.9(e)-(g). In addition, as depicted in Fig.4.10(a), the bead height *h* and vertical-down displacement *d*, were recorded using a laser scanner. The results are plotted to illustrate the bead profile variation as a function of welding distance (the welding speed was constant at 500 mm/min). As provided in Fig.4.10(b), the general trends of the bead profile variation in both horizontal and vertical direction are analogous. It can be deduced that compared to the one-dimension humping in the flat deposition, the humped weld bead formed in both directions of wall growth and gravitational force synchronously. This confirms the presented humping formation mechanism in Section 4.2.

4.4.2 The impact of process parameters on humping

Since wire feed speed (*WFS*) and travel speed (TS) are the two major input parameters in WAAM process [7], it is necessary to investigate their impacts on humping formation to further verify the proposed humping mechanism and to give guidelines for parameter selection in multi-directional WAAM. In the test group B, the *TS* was kept constant at 100 mm/min while the *WFS* was varied between 1.0 and 5.0 m/min. Fig.4.11 provides the process parameters, the molten pool geometries and the bead appearances of each test. The weld bead appearances show no periodical variation in dimensions along the welding direction, which means no humping occurred. Images of the weld pool are presented to assist the analysis of the molten pool behaviour (one representative image of each test is provided as the molten pool is analogous without humping). Note that molten pool geometry parameters (depth and length) are introduced here to help describe the molten pool geometry. The depth and the length of the molten pool are defined as the distance from the weld pool underneath wire electrode to the bottom and the tail of the molten pool, as illustrated schematically in Fig.4.12(a). As illustrated in Fig.4.11(a) to (f), the molten pool size increases in both depth and length with the increase in *WFS*. In GMAW welding, the welding current increase with the increase of *WFS* [107]. According to equation (1), the initial momentum of the metal flow increases, which may lead to humping. However, with a deeper weld pool, a portion of the metal flow momentum might be dissipated and thereby no humped weld bead forms. Based on the results, it is assumed that a long and shallow weld pool represents a high chance of humping occurrence while a short and deep weld pool means a low chance of humping occurrence. Thus, molten pool dimensional ratio r (defined as $r=l/d$) was introduced as an indicator representing the chance of humping occurrence.

With different welding parameters. Fig.12(b) presents the molten pool dimension and dimensional ratio r for each test in group B. It can be seen that r remains stable while the molten pool size increases in both depth and length with the increase in *WFS*.

The impact of *TS* on humped weld bead was investigated in the test group C. A set of tests were conducted in which the *TS* was changed from 100 to 500 mm/min while the material deposition ratio r_v ($r_v=WFS/TS$) was set to a constant value 10. The material deposition rate r_v determines the volume of the weld metal deposited in a unit time. As shown in Fig.4.13(a), with low *TS*, a short molten pool was formed which means the backward metal flow is relatively weak. Thus, it is difficult to form humped weld bead. With higher *TS*, the momentum of the metal flow increased [72, 117], the molten pool became elongated and shallow when the heat source moves away, as shown in Fig.4.13(e). Molten metal continues to transfer through the narrow channel to the rear of the weld pool, resulting in the accumulation of the weld metal. Once the thin wall jet solidified, the liquid stream was prevented flowing to the swelling area. Then, the portion of the liquid channel became the valley of the humped weld bead.

Fig.4. 11 The side-view of molten pool behaviour (a-e) of test 1 to 5 in group B.

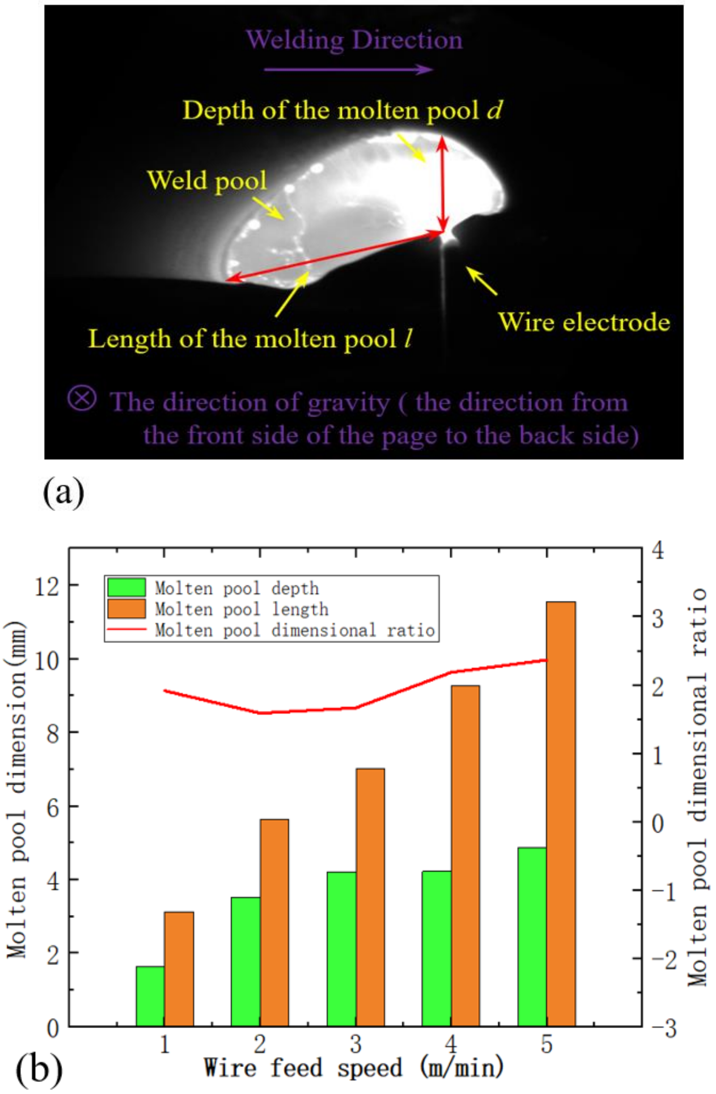

Fig.4. 12 (a) The definition of molten pool dimensions, and (b) the molten pool dimensions and molten pool dimensional ratio r of test 1 to 5 in group B.

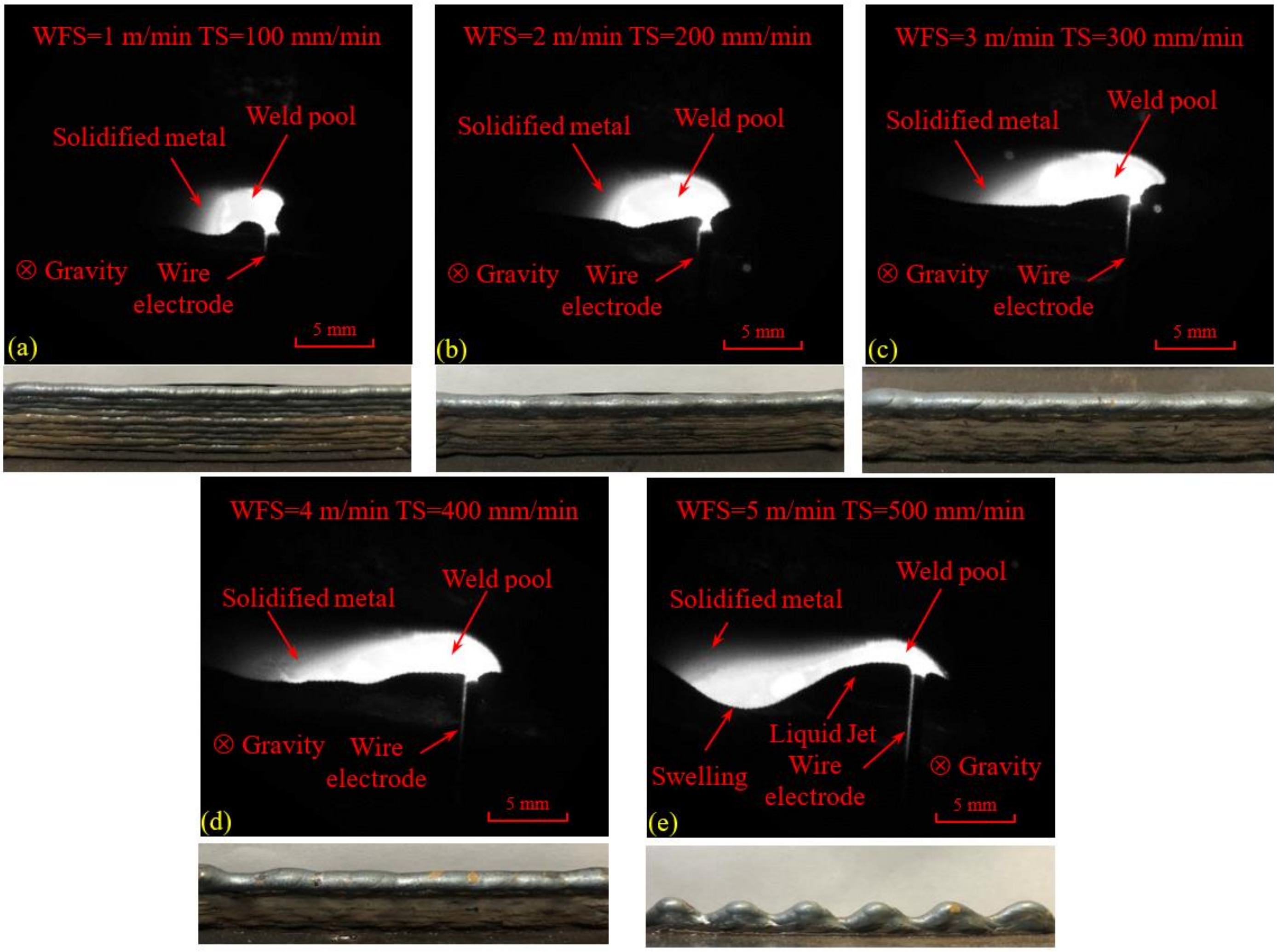

Fig.4. 13 The side-view of molten pool behaviour (a-e) of test 1 to 5 in group C.

In addition, the depth *d*, length *l*, and dimensional ratio *r* of the weld pool in group C are plotted in Fig.4.14. With the *TS* increased from 100 to 400 mm/min, the weld pool extended significantly in length while the depth of the weld pool varied slightly. However, with the *TS* increased to 500 mm/min, the molten pool continued to increase in length while decreasing in depth. As a result, humping occurred when the molten pool dimensional ratio *r* increased to 8. So, the molten pool dimensional ratio *r* may indicate the chance of humping occurrence with different welding parameters.

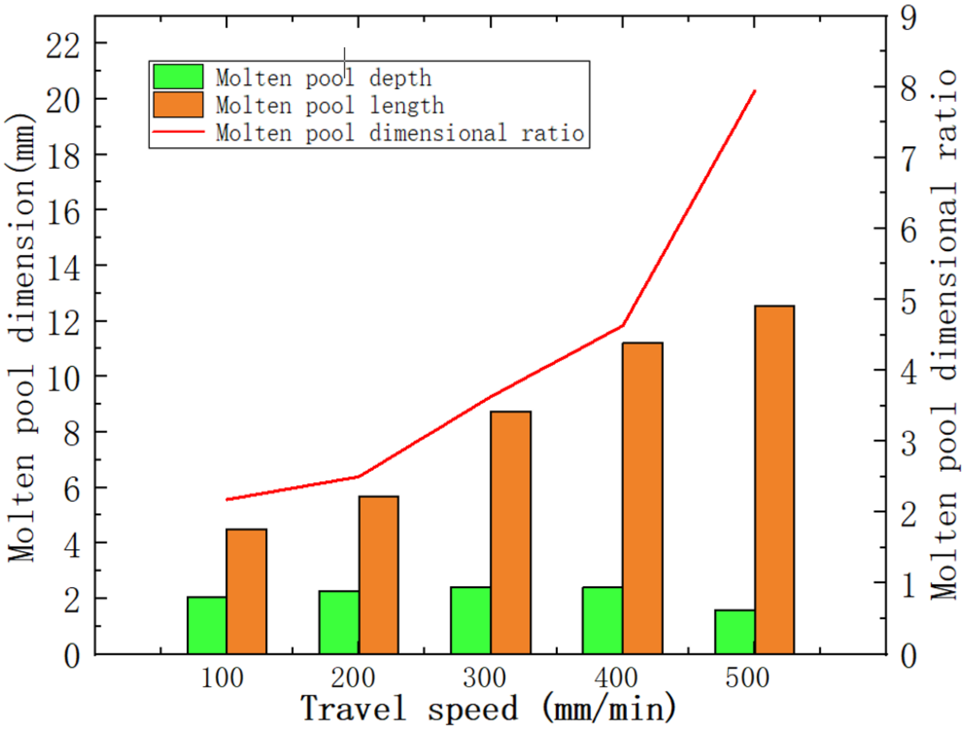

Fig.4. 14 The molten pool dimensions and molten pool dimensional ratio r of test 1 to 5 in group C.

4.5.3 The impact of welding positions on humping

The proposed mechanism for humping formation indicates that the strong backflow stream of the weld metal is responsible for the formation of humping. Different welding positions may have distinct influences on the metal flow. Fig.4.15 presents the molten pool images of vertical-down and vertical-up deposition in group D and E. In the tests, the material deposition ratio was set to 10, the *TS* varied from 100 to 300 mm/min, and *WFSs* were adjusted accordingly. In the experiment, humping occurred in vertical-up deposition when the TS is

300mm/min or higher, while no humping is observed for vertical-down deposition even when the TS is increased to 800 mm/min.

Fig.4. 15 The side-view of molten pool behaviour (a-c) of test 1 to 3 in group D, and (d-f) of test 1 to 3 in group E.

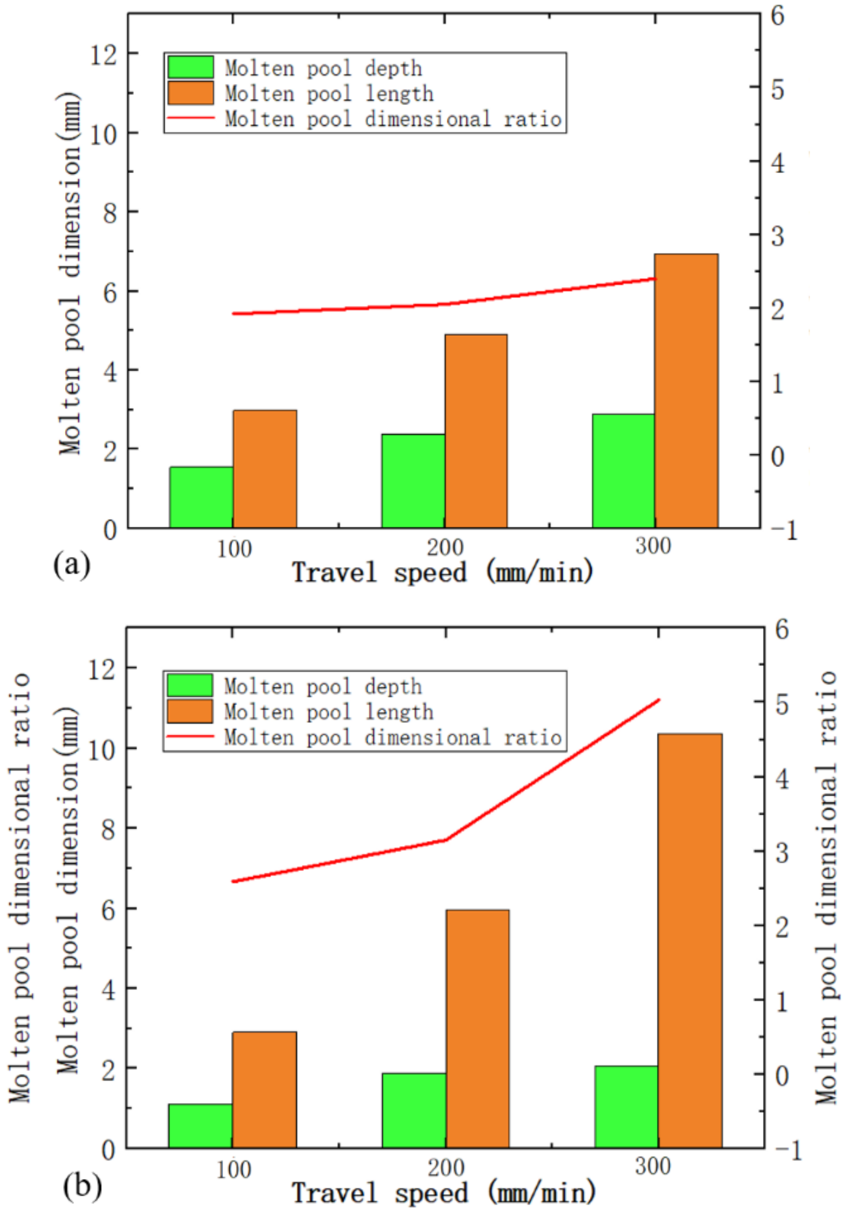

Fig.4. 16 The molten pool dimensions and molten pool dimensional ratio r of test 1 to 5 in group D (a) and E (b).

In vertical-down deposition, the molten metal flowed upward to the rear of the weld pool while the gravity pulls downward and suppressed the momentum of the upward flow. It is difficult to accumulate weld metal at the tail of the molten pool and the gouging area underneath the welding arc can be filled readily. Conversely, the downward molten flowed has been strengthened by the gravitational force during vertical-up welding, resulting in an elongated molten pool and the humps were easily formed at the tail of the molten pool. The results confirmed that the momentum of the backward molten metal flow is responsible for the humped weld bead and the gravitational force has a significant impact on humping formation when welding in different welding positions. Taking advantages of welding in vertical-down position, higher welding speed can be taken to increase the productivity of the WAAM process.

Moreover, the molten pool geometry and dimensional ratio as the function of *TS* of test group D and E are presented in Fig.4.16(a) and (b). For vertical-down deposition, both the depth and length of the molten pool increased with the increase in *TS*, resulting in a nearly constant value of *r* and thereby the humping did not occur. Conversely, when using a higher *TS* in the vertical-up deposition, *r* increased due to the increase in molten pool length is greater than its depth, indicating a higher chance of humping occurrence.

4.5 Discussion

4.5.1 The humping formation

The experimental results in Section 5 confirm the theoretical analysis in Section 3 for humping formation in positional deposition using the CMT process. Generally, a strong backward metal flow is responsible for the humping formation. Compared to welding in the flat position, the weld bead geometry deteriorates easier since the liquid metal flow is strengthened by the gravitational force in the positional deposition. The experimental results on various process parameters show that higher *TS* could produce strong backward flow to form a humped weld bead while *WFS* has little correlation with humping formation. In addition, taking advantages of gravity, the vertical-down welding allows a higher welding speed and forms weld beads with better geometries than welding in vertical-up direction.

A new concept, molten pool dimensional ratio, $r=l/d$, was identified as an indicator of humping occurrence with different welding parameters. As larger dimensional ratio represents higher momentum of the backward flow, the dimensional ratio can be used to represent the chance of humping formation in different deposition positions. The effectiveness of various humping suppression methods may be examined by calculating molten pool dimensional ratio r, which potentially can be used to systematically develop future humping suppression strategies.

4.5.2 Recommendations for multi-directional WAAM process

In addition to the analysis humping phenomenon itself, this study also aims to provide guidelines for multi-positional WAAM regarding the process parameter selection and path planning. Firstly, to enable a stable deposition process with a wide process parameter range, the selection of *TS* and deposition position are critical for humping avoidance. The welding positions are defined as the angle θ between welding direction and vertical-up direction in the vertical plane. For example, the vertical-up direction is 0°, the horizontal direction is 90°, and the vertical-down direction is 180°. The humping map, presented in Fig.4.17, describes the relationship between *TS*, θ and humping occurrence based on the experimental results. The horizontal axis represents *TS*, while the vertical axis represents θ. With additional experimental tests, the humping occurrences have been marked on the map. As shown in the graph, with the aid of the gravitational force, the maximum *TS* increases while θ increases, the welding parameters should be chosen from the left upper parts of the humping map. The humping map approach can be used to provide a database for parameter and welding position selection. If necessary, the database can be more accurate when more tests are conducted between the boundaries of humping and no humping region

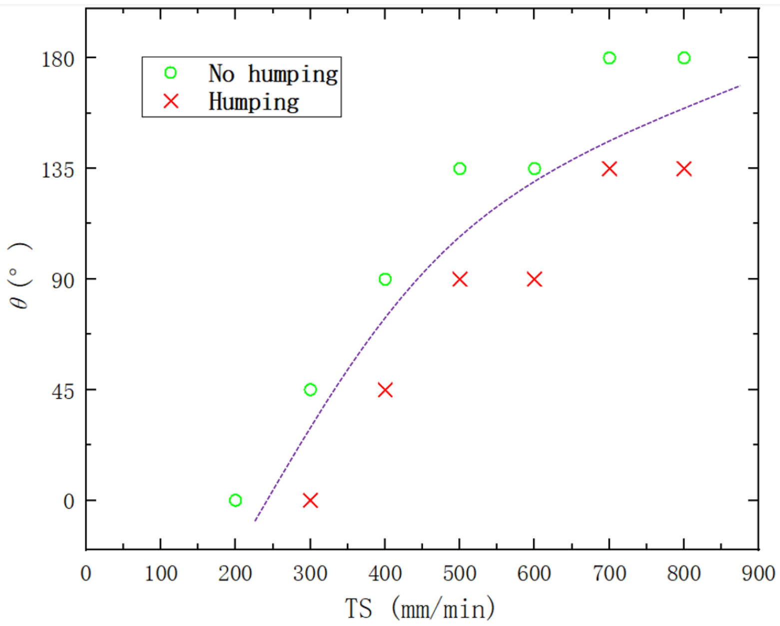

Fig.4. 17 The proposed humping map.

Secondly, a good understanding of humping formation provides guidelines for the path planning. For example, four path planning schemes are list in Fig.4.18(b) for depositing a horizontal rectangular section (yellow) parts of the workpiece in Fig.2.1. The overhanging part can be fabricated by depositing horizontally (strategy A), vertical-up (strategy B), vertical-down (strategy C), or along a contoured path (strategy D).

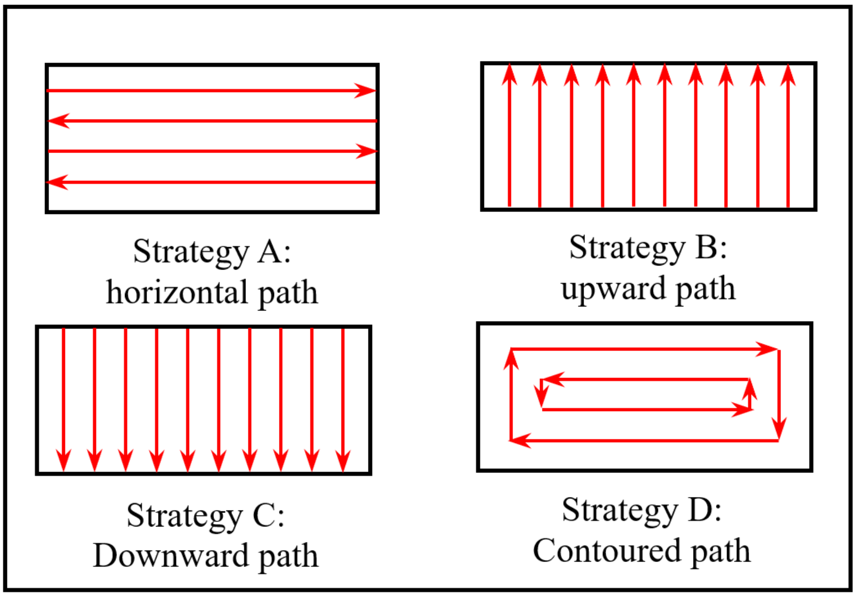

Fig.4. 18 Different path planning strategies in WAAM.

As previously analysed, taking advantages of gravity, the use of vertical-down position allows a higher welding speed than both vertical-up and flat position. From a practical WAAM perspective, some recommendations for path planning are provided as i) in the path planning stage, it is recommended to deposit overhanging parts in a vertical-down position, as strategy C in Fig.4.18. The welding process is more stable with a wider range of process parameter selection. ii) When the deposition path has multiple welding directions, for example, the contour path in strategy D in Fig.4.18, it is necessary to use the travel speed with the strictest restriction (vertical-up) to guarantee a humping free deposition.

4.5.3 Case study

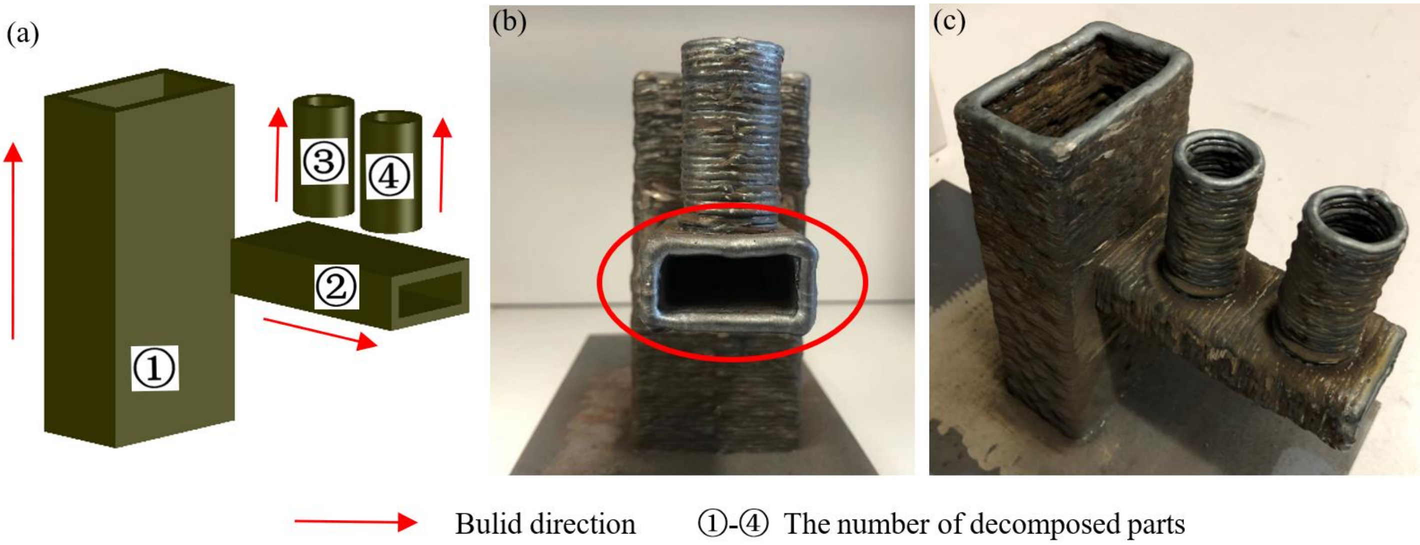

Fig.4. 19 (a) The 3D model of the part, (b) A humping free deposition, and (c) The overall appearance of the workpiece.

The effectiveness of the proposed humping avoidance strategy outlined in this study is demonstrated through the fabrication of a thin-wall workpiece with overhanging features. Fig.4.19(a) presents the 3D model of the workpiece, the sub-volumes of the workpiece are numbered and the building direction of each sub-volume are also illustrated in Fig.4.19(a). The key step for the fabrication of this workpiece is the deposition of the sub-volume two. According to the geometrical feature, a contour path is chosen to fabricate sub-volume two (Note that the start position of each deposition is designate to be different for mitigating the swellings at the connection point). Humping was observed at this situation using normal welding parameters for down-hand welding. Thus, the welding parameters must be carefully selected to avoid the occurrence of humping in positional deposition. Firstly, the weld path consists of three directions (0°, 90°, and 180°), the welding travel speed should be determined with the most restricted condition (vertical-up) to guarantee a humping free deposition. Then, according to the humping map in Fig.19, the welding travel speed is limited in the range from 0 to 200 mm/min. Finally, the wire feed speed is determined at 2 m /min to meet its cross-section dimensions. Fig.4.19(b) demonstrates a humping free surface of sub-volume which proves the effectiveness of the proposed strategy. The overall appearance of the fabricated workpiece is presented in Fig.4.19(c).

4.6 Chapter summary

This chapter investigated the humping phenomenon for multi-layer multi-directional WAAM process. Firstly, the mechanism of humping formation was analysed for positional deposition using GMAW in the CMT process mode. It was found that the backward metal flow under the effect of gravity is responsible for the sagged humps in the positional deposition. Secondly, based on the observation of molten pool behaviour, the humping formation mechanism was confirmed. A molten pool dimensional ratio r is identified as an indicator for humping occurrence and can be used to help parameter selection. Finally, a series of guidelines are summarised to assist the practical use of multi-directional WAAM, (i) humping can be avoided through planning an elaborate robot trajectory (vertical-down path is the most recommended direction). (ii) it is necessary to use the travel speed with the most restricted condition (vertical-up) to guarantee a humping free deposition.

Chapter 5

Robot path planning

5.1 Introduction

Multi-directional WAAM is a process with great potential in the manufacturing field, and is at its nascent development stage. Compared to conventional WAAM processes, which are limited to depositing parts along a fixed vertical-up direction, the programming process for a multi-directional approach becomes complicated as (i) Most existing WAAM systems plan torch trajectories based on the CAD model of the part to be fabricated, and assume the robot/machine can always perform the required trajectories. This is true when part sizes are small and the welding torch is always kept down hand. However, generation of collision-free robot motions for deposition paths featuring multiple torch orientations can be difficult, and little evidence of this consideration exists in literature related to WAAM research. (ii) The deposition sequence is no longer in a bottom-to-top configuration, as the overhanging structure can be built at different stages of the fabrication process. The optimisation of the sequence in which each layer is welded plays a critical role in avoiding collision between the torch and partially deposited component.

Path planning in robotic welding applications originally concerned problems relating to moving a welding torch along a predetermined weld trajectory without any collision. Current studies attempt to develop optimal collision-free robot motion strategies through two major steps, environment modelling and optimal path searching [85]. In the study by [86], environment obstacles and robot bodies are simulated in a Configuration Space (C-Space) environment, where the robot configuration is defined by a set of joint coordinates [87]. In this environment, an Artificial Potential Field was applied to guide the robot and generate a collision free weld path. [85] also reported a welding robot collision free path optimization strategy. The environment, including robot and obstacles, is simulated through a simple grid method. Optimized collision free robot motion is programmed based on an Ant Colony Optimization algorithm. Simulation results demonstrate that the proposed system can automatically generate the shortest robot path without collision. [88], identified that welding quality is sometimes disrupted when using traditional robot motion planning methods. This is because a welding task is inherently different from a simple point-to-point robot motion problem, which the majority of these planning algorithms were developed to address. The positional configuration of the welding torch will have various impacts on the appearance and quality of the weld bead. To improve welding quality, they present a Probabilistic Road Map motion planner, developed specifically for robotic welding applications, where control of the operational range of the welding torch angle is a primary concern [88, 89].

There are many considerations which must be made in order to apply these strategies to multi-directional WAAM. This is due to the fundamental differences between traditional welding and multi-directional WAAM. In welding processes, the geometry of the part is fixed, and motion planning is performed in a static environment. However, in a WAAM application, the volume of the grows dynamically as the deposition process proceeds, which complicates the motion planning problem, as it is now performed in a semi-dynamic environment. The collision model of the workpiece now needs to be updated after each layer of deposition is completed. Since the deposition sequence for each layer affects the collision model of the part, the layer sequence becomes critical for successfully planning a collision free deposition path [8]. In this application, deposition sequencing and single layer path planning are interwound together, which produces a complex problem to address.

The aim of this chapter is to develop a complete path planning algorithm for the multi-directional WAAM process, which enables the novel manufacturing technology to be widely adopted for practical industrial use.

5.2 Algorithm Framework Overview

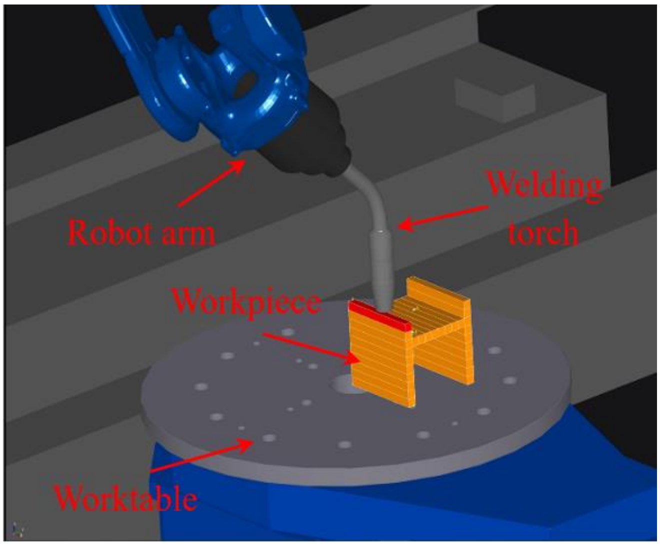

Fig.5. 1 The simulation wind of the AOLP engine.

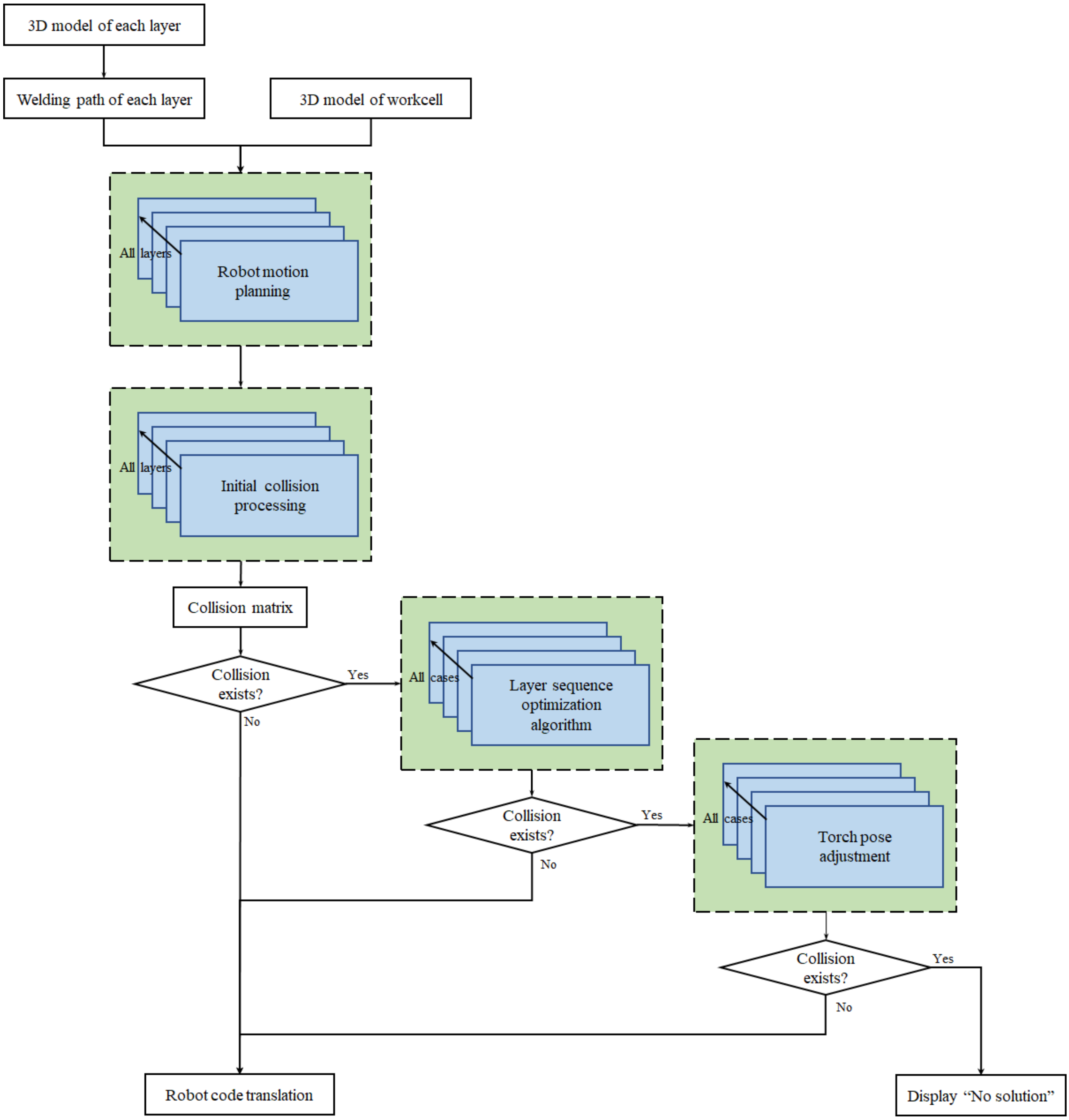

Fig.5. 2 Overall workflow of the proposed algorithm.

To generate collision free deposition paths, a number of key factors must be considered. Firstly, for each layer in the deposition sequence, a valid robot trajectory must be planned so that the robot is able to deposit the layer without exceeding its kinematic limits or colliding with the surrounding environment (including the partially manufactured component). Additionally, a valid build sequence for all layers needs to be identified. These two planning processes are interwound with each other and present a challenging optimisation problem. This planning process is supported by an automated robot offline programming (AOLP) engine [121], which provides a simulation model for the robotic WAAM system, as shown in Fig.5.1. With this offline programming engine, robot motions can be efficiently planned and simulated to test robot reachability and collision. Whilst the most straightforward method is to test all possible combinations of build sequences and robot motion options in a brute-force manner, the exceedingly large number of possible permutations, particularly for more complex parts, renders it prohibitive to do so. To find an acceptable solution in a short time-frame, an efficient search algorithm which breaks the complex search problem into multiple steps, each with much lower DoFs, was developed in this study.

The framework of the proposed robot path planning algorithm for multi-directional WAAM is presented in Fig.5.2. The framework features four key modules: a) robot motion planning, b) initial collision processing, c) layer sequence optimization, and d) weld torch pose adjustment. The first module generates nominal robot motions for each layer using the welding path and 3D model of the robot, torch and worktable. In this step, an efficient task space (T-Space) planning algorithm [89] is used to generate the required robot motions. At this stage of the process, collision free motions between the robot, torch and worktable have been generated, however, collision between the torch and previously deposited layers is not considered due to the, at this stage of the process, undetermined deposition sequence. The second step involves generating an initial collision matrix *C,* based on the nominal path of each layer. In the collision matrix *C*, all collisions occurring between the robot and a particular layer are encoded at the corresponding element. If the initial build plan is valid (i.e. collision free), we can directly generate the final robot code. Otherwise, we enter an iterative planning loop, which sorts the build order algorithmically to remove or minimize existing collisions. Finally, if collision still exists, accessibility constraints between the nozzle and workpiece can be solved by adjusting welding torch pose (within an acceptable range). Further details of these four key modules will now be presented.

5.3 Robot motion planning

In this work, AOLP engine [121] is adopted to generate valid robot motions for each weld path such that (i) the weld torch tip is able to trace the predetermined weld path with the nominal contact to work distance (CTWD), (ii) the robot does not exceed any of its kinematic limits, (iii) the robot and torch do not collide with any objects in their environment and finally (iv) the relative angles between the welding torch and the weld seam (R_x and R_y) remains at 90° (note that the 90° torch angle is default to achieve a constant weld bead geometry, however it may be adjusted in later stages of the planning process to avoid collisions, details of this are presented in Section 5.6). The above conditions allow us to create a partially constrained robot path planning problem which can be resolved by the AOLP engine.

Table 5. 1 T-Space parameters for robotic welding task (wt.%).

Variable	Definition
t	Position along the robot path
cfg	Robot configuration representing Inverse Kinematics solution.
R_x, R_y, R_z	Welding torch orientation along *x*, *y*, and *z* axis.
CTWD	Contact to work distance (CTWD)
rail	Configuration of the external robot track (if applicable)

The AOLP engine used in this work uses a Task-Space Motion Planning Decomposition (TSMPD) approach [89] to efficiently search for an optimal path in high Degree of Freedom (DoF) space. In a similar analog to Cartesian Space (C-Space), which contains all possible robot configurations, Task Space (T-Space) consists of configurations constrained to the specific task. For the WAAM process, T-Space can be defined by the parameters outlined in Table 5.1 below. The implementation details for the TSMPD are as follows.

First, a T-Space kinematic equation TK(s) is defined as below

$$TK\left(R_x, R_y, R_z, ctwd, cfg, \text{rail}, t\right) = T_0^{tool} \tag{5.1}$$

$$T_0^{tool} = T_0^{target} * T_{target}^{tool} \tag{5.2}$$

where T_0^{target} represents the tool transform at position *t* along the weld path. T_{tool}^{target} applies the local T-Space configuration parameters R_x, R_y, R_z, *CTWD* to the tool position, as shown in Eq.(5.3).

$$T_{target}^{tool} = \begin{bmatrix} Rot_x(R_x)Rot_y(R_y)Rot_z(R_z) & \begin{matrix} 0 \\ 0 \\ ctwd \end{matrix} \\ 0 \quad 0 \quad 0 & 1 \end{bmatrix} \tag{5.3}$$

The TSMPD algorithm first generates a dependency matrix, which relates the motion of each of the robot $b \in B$ to the T-Space parameters T. Eq. (5.4) is used to generate this matrix, where D_{ij} is marked true if the pose of B_i is affected by T-space parameter T_j.

$$D_{ij} = \frac{dB_i}{dT_i} \neq 0 \forall i \in [0, n], j \in [0, m] \tag{5.4}$$

Table 5. 2 TSMPD Boolean dependency matrix.

Body	Parameter						
	t	R_x	R_x	R_x	*ctwd*	*cfg*	*rail*
Base	×	×	×	×	×	×	√
J_1 - J_5	√	√	√	√	√	√	√
J_6	√	√	√	√	√	×	×
Torch	√	√	√	√	√	×	×
Nozzle	√	√	√	×	√	×	×

The resultant Boolean dependency matrix is shown in Table 5.2. With this table, each of the T-space parameters can now be ranked in order of the number of dependent bodies each has, as shown in Table 5.3. This ordering is used to structure the collision checking process; it allows the collision checker to focus its search on parts of the robot which are more likely to cause collision, creating an efficient means of solving the sampling-based motion planning problem.

Table 5. 3 Parameter ordering for WAAM task.

Order	Variable	Body
1	*t*, R_x, R_y	-
2	*ctwd*	Nozzle
3	R_z	Torch, J_6
4	*rail*	Base
5	*cfg*	$J_1 - J_5$

Due to the large number of parameters in the T-space formulation, a brute force search will be prohibitively slow for practical purposes. The TSMPD breaks the overall path planning problem into a set of sequential sub-problems that dramatically increases the overall search efficiency. For our particular formulation of T-Space (i.e. a welding task), the search takes the following approach:

a) For the welding torch nozzle, a collision free path along the weld, for the parameter subset R_x, R_y and *CTWD* is found, then
b) For the welding torch body, and robot joint 6 (wrist), a collision free path for parameter R_z, using the previously found path from a) is found, then

c) For the Base, a collision free path for the turntable is found using the path from b), then finally

d) For J_{1-5}, a collision free path for parameter *cfg*, using the previously found path c), is determined.

If one of these steps fails to find a valid path, the solution from the previous step is invalidated. We then backtrack and re-solve the problem from the previous step and continue. Each of these sub-problems is solved within a discretised T-Space, sampling-based, graph searching algorithm. T-Space is sampled randomly with many combinations of available parameter sets. Once sampled, graph-based search algorithms can find a minimum cost path through the sampled T-Space. Note that this robot motion planning method is used only on the current deposition layer. Collision between the robot/torch and other layers of the part is not considered at this stage. However, compared to the welding process, the volume of the part keeps growing dynamically in the WAAM deposition process, which may lead to more collision occurrences.

5.4 Initial collision processing

Once robot motions for each layer have been planned, the collision between the robot and other layers of the same part can be tested, as shown in Fig.5.3(a), where layers coloured in red indicate the presence of collision between the robot and/or torch while depositing a layer underneath. This information is stored and used to generate an initial collision matrix *C*, which is used as a heuristic to guide the later stages of the deposition sequence planning (Section 5.5).

To assist with explanations over the following sections, a sample part, shown in Fig.5.3(b), is provided. Firstly, the deposition path of each layer is generated from its 3D CAD model through multi-direction WAAM planning algorithm (details can be found in [122]), as shown in Fig.5.3(c). The individual layers are numbered categorically relating to their local sub-volume. Then, the collision matrix C is generated. This matrix is square, its dimensions equal to the number of layers of the part to be manufactured. As shown in Fig.5.4 rows of the C represent weld paths of each layer; columns are used to represent a geometric collision model of each deposited layer. The welding simulation feature of the robotic AOLP engine is then used to fill the elements of C. As the AOLP software searches for its solutions, the 3D model of each layer is added to the simulation system to emulate the build process.

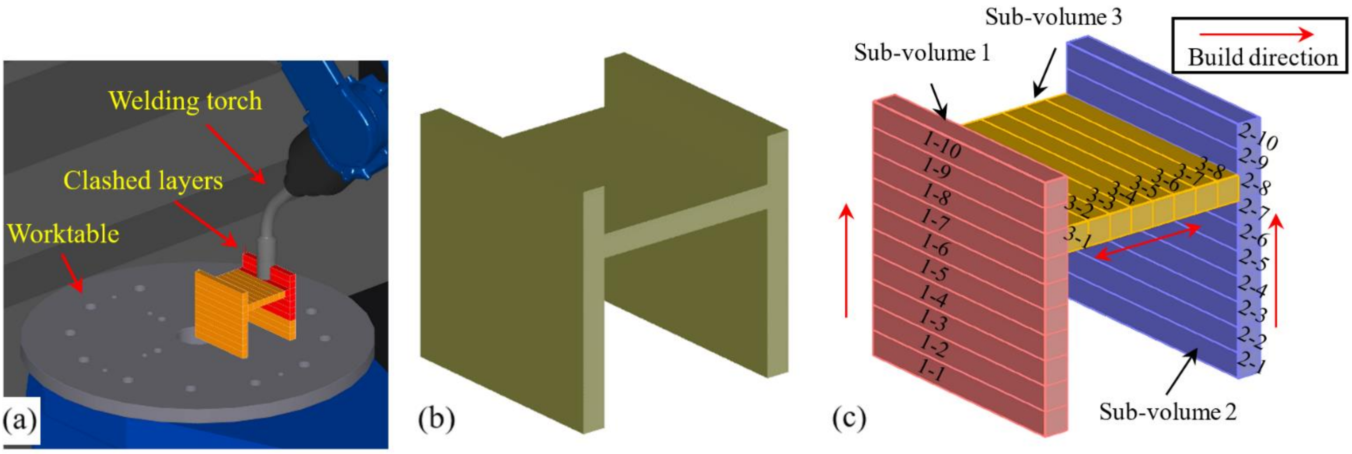

Fig.5. 3 (a) The clashed layers (in red) and other layers (in yellow), (b) the original 3D model, and (c) the processed 3D model of the part with layer number.

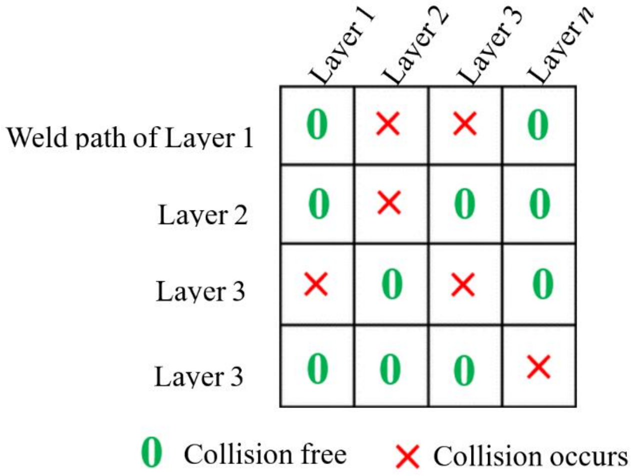

Fig.5. 4 The structure of the collision matrix *C*.

The AOLP system simulates the required robot motions for each layer, and simultaneously monitors for collision with the other layers. It is worth mentioning that many collision models exist for the detection of collision between the robot, tool, workpiece and environment models [85, 123-125]. In this work, a simplified bounding volume approach is utilised, primarily due to its fast calculation times [121]. Robot motions for each weld-path/layer are simulated. If collision is detected between the robot and a particular layer, the corresponding element in *C* is marked with an “×”, as shown in Fig.5.5. The data encoded in *C* is used in later stages to identify collision between the robot/tool and the part. It provides a rapid look-up table for potential collision, which is useful as the parts geometric model is changing as more layers are deposited. Further details of matrix *C* are explained as below,

(i). The first column of *C* is the deposition sequence determined according to the sub-volume numbers.

3D model of each layer

Weld path of each layer

		1-1	1-2	1-3	1-4	1-5	1-6	1-7	1-8	1-9	1-10	2-1	2-2	2-3	2-4	2-5	2-6	2-7	2-8	2-9	2-10	3-1	3-2	3-3	3-4	3-5	3-6	3-7	3-8
1	1-1		×	×	×	×	×	×	×	×	×	0	0	0	0	0	0	0	0	0	0	×	0	0	0	0	0	0	0
2	1-2	0		×	×	×	×	×	×	×	×	0	0	0	0	0	0	0	0	0	0	×	0	0	0	0	0	0	0
3	1-3	0	0		×	×	×	×	×	×	×	0	0	0	0	0	0	0	0	0	0	×	0	0	0	0	0	0	0
4	1-4	0	0	0		×	×	×	×	×	×	0	0	0	0	0	0	0	0	0	0	×	0	0	0	0	0	0	0
5	1-5	0	0	0	0		×	×	×	×	×	0	0	0	0	0	0	0	0	0	0	×	0	0	0	0	0	0	0
6	1-6	0	0	0	0	0		×	×	×	×	0	0	0	0	0	0	0	0	0	0	×	0	0	0	0	0	0	0
7	1-7	0	0	0	0	0	0		×	×	×	0	0	0	0	0	0	0	0	0	0	×	0	0	0	0	0	0	0
8	1-8	0	0	0	0	0	0	0		×	×	0	0	0	0	0	0	0	0	0	0	0	0	0	0	0	0	0	0
9	1-9	0	0	0	0	0	0	0	0		×	0	0	0	0	0	0	0	0	0	0	0	0	0	0	0	0	0	0
10	1-10	0	0	0	0	0	0	0	0	0		0	0	0	0	0	0	0	0	0	0	0	0	0	0	0	0	0	0
11	2-1	0	0	0	0	0	0	0	0	0	0		×	×	×	×	×	×	×	×	×	0	0	0	0	0	0	0	×
12	2-2	0	0	0	0	0	0	0	0	0	0	0		×	×	×	×	×	×	×	×	0	0	0	0	0	0	0	×
13	2-3	0	0	0	0	0	0	0	0	0	0	0	0		×	×	×	×	×	×	×	0	0	0	0	0	0	0	×
14	2-4	0	0	0	0	0	0	0	0	0	0	0	0	0		×	×	×	×	×	×	0	0	0	0	0	0	0	×
15	2-5	0	0	0	0	0	0	0	0	0	0	0	0	0	0		×	×	×	×	×	0	0	0	0	0	0	0	×
16	2-6	0	0	0	0	0	0	0	0	0	0	0	0	0	0	0		×	×	×	×	0	0	0	0	0	0	0	×
17	2-7	0	0	0	0	0	0	0	0	0	0	0	0	0	0	0	0		×	×	×	0	0	0	0	0	0	0	×
18	2-8	0	0	0	0	0	0	0	0	0	0	0	0	0	0	0	0	0		×	×	0	0	0	0	0	0	0	0
19	2-9	0	0	0	0	0	0	0	0	0	0	0	0	0	0	0	0	0	0		×	0	0	0	0	0	0	0	0
20	2-10	0	0	0	0	0	0	0	0	0	0	0	0	0	0	0	0	0	0	0		0	0	0	0	0	0	0	0
21	3-1	0	0	0	0	0	0	0	0	0	0	0	0	0	0	0	0	×	×	×	0		×	×	×	×	×	×	×
22	3-2	0	0	0	0	0	0	0	0	0	0	0	0	0	0	0	0	×	×	×	0	0		×	×	×	×	×	×
23	3-3	0	0	0	0	0	0	0	0	0	0	0	0	0	0	0	0	×	×	×	0	0	0		×	×	×	×	×
24	3-4	0	0	0	0	0	0	0	0	0	0	0	0	0	0	0	0	×	×	×	0	0	0	0		×	×	×	×
25	3-5	0	0	0	0	0	0	0	0	0	0	0	0	0	0	0	0	×	×	×	0	0	0	0	0		×	×	×
26	3-6	0	0	0	0	0	0	0	0	0	0	0	0	0	0	0	0	×	×	×	0	0	0	0	0	0		×	×
27	3-7	0	0	0	0	0	0	0	0	0	0	0	0	0	0	0	0	×	×	×	0	0	0	0	0	0	0		×
28	3-8	0	0	0	0	0	0	0	0	0	0	0	0	0	0	0	0	×	×	×	0	0	0	0	0	0	0	0	

Deposition sequence

Existing clash

Target area of the collision matrix

Fig.5. 5 Initial collision matrix C for the selected part.

(ii). Column naming conventions in *C* are listed, for example, as a-b. In our system, the 3D geometric model of the part is divided into sub-volumes, as shown in Fig.5.3(c). "a" denotes the sub-volume number and "b" represents the specific layer number within its sub-volume.

(iii). In the matrix *C*, a '0' element denotes the corresponding deposition is collision free and "×" denotes that some form of collision has been detected for that particular weld path.

(iv). The elements in the bottom-left triangle region of the matrix *C* represent the collision information obtained during the deposition process. For a particular layer, all "×" in the bottom left triangle means collision occurs between the specific layer and the layers deposited before it. On the other hand, the "×" in the upper-right triangle indicates collision occurs between the selected layer and layers deposited subsequently, which is not of concern. For example, row 23 of *C* in Fig.5.5 indicates the collision information during the deposition of path 3-3. The welding torch clashes with layer 2-7 to 2-9 and 3-4 to 3-8. However, the layer 3-3 is deposited after 2-7 to 2-9 and before layer 3-4 to 3-8, thus, it only clashes with layer 2-7 to 2-9.

5.5 Layer sequence sorting

The initial collision matrix *C* provides a useful tool to rapidly query collision between the robot/torch and deposited layers of the part. In this section, *C* is used as a heuristic to guide a sequence sorting algorithm in an attempt to determine a valid build sequence. To do this, three main steps are performed, as follows.

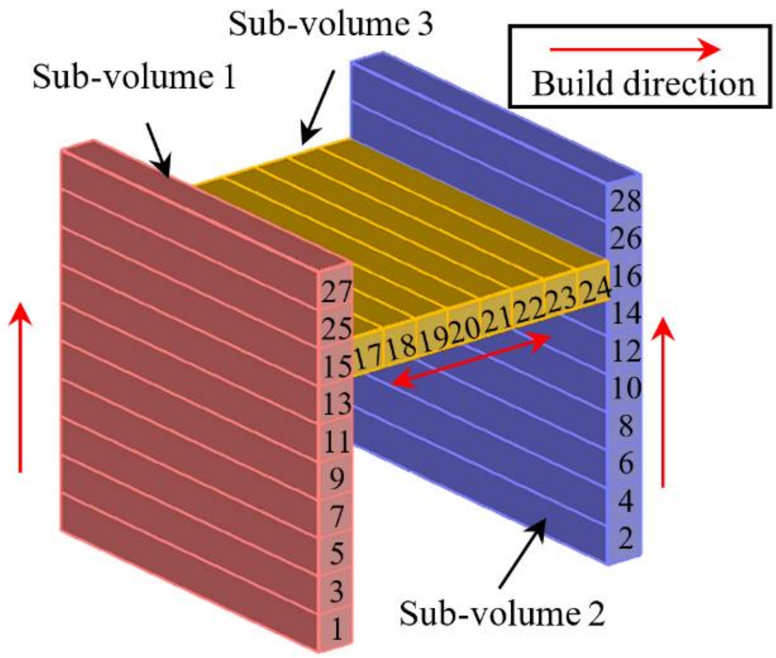

Fig.5. 6 The layer deposition sequence was reordered from bottom to top.

a) The layers are first ordered according to their height in the global z direction, i.e. all layers are ordered from the bottom to the top, as outlined in Fig 5.6.

b) Layer dependency identification. Layer dependency relates to whether a particular layer can be deposited before or after a previous layer. Layer dependency can be classified into three core types: absolute dependence, multiple dependence, and no dependence. Fig.5.7 illustrates this further, in the form of a dependency matrix *D* for the part presented in Fig.5.6. Absolute dependence and no dependence are recorded as "1" and "0" in the matrix, respectively. Absolute dependence occurs when a layer can only be deposited after the layer underneath is completed. For example, the first to the tenth layers of sub-volume 1 are deposited on the adjacent layer along the z direction. On the other hand, no dependence indicates the deposition of a layer does not depend on the completion of other layers. Multiple dependence denotes a particular layer can be deposited from more than one direction. For example, the layers in sub-volume 2 of the part in Fig.5.6 would be classified in the multiple dependency category. Two or more build scheme will be created according to the build sequence. For example, if the build direction of sub-volume three is determined from sub-volume one to sub-volume two, layer 3-1 is required to be deposited on layer 2-7, 2-8, and 2-9, as marked as "(scheme) a" in the matrix *D*. On the other hand, in the "scheme b", the build direction of sub-volume three is determined from sub-volume two to sub-volume one. Thus, layer 3-1 is deposited on layer 3-2. Note that the dependence of the rest of the layers in sub-volume three are also marked as scheme a or b based on the designated build direction. The layer dependence matrix *D* is imposed to the final optimal layer sequence searching process to ensure the robot motion is executable.

c) The goal of these sequencing operations is to avoid or minimize potential collisions. To do this, the information obtained from collision matrix C and layer dependence matrix D are combined. An A* [22] search algorithm is adapted here to search for a deposition sequence (from matrix D) with the minimum occurrences of collision (from matrix C). While the A* algorithm will search for the optimal solution, it may prove too computationally expensive for a large-scale part with a large number of layers. Thus, the proposed algorithm first focuses on adjusting the layer sequence for layers found to collide other layers. The scope of the search will then extend to their adjacent layers if no solution is obtained. In addition, the information obtained from the analysis of the layer dependence matrix D is also incorporated. By incorporating this information into the search, the number of possible the build sequence combinations is drastically reduced, which in turn will speed up the overall search. Fig.5.8 presents the final build sequence for the example part shown in Fig.5.6. The number of collision occurrences is reduced from eight (layer 3-1 to 3-8) to one (layer 2-7). Collisions which remain after this process of sequence optimisation are addressed by adjustment of welding torch pose parameters, which is covered in the next section.

3D model of each layer

Weld path of each layer

	B	1-1	1-2	1-3	1-4	1-5	1-6	1-7	1-8	1-9	1-10	2-1	2-2	2-3	2-4	2-5	2-6	2-7	2-8	2-9	2-10	3-1	3-2	3-3	3-4	3-5	3-6	3-7	3-8
1-1	1	-	0	0	0	0	0	0	0	0	0	0	0	0	0	0	0	0	0	0	0	0	0	0	0	0	0	0	0
1-2	0	1	-	0	0	0	0	0	0	0	0	0	0	0	0	0	0	0	0	0	0	0	0	0	0	0	0	0	0
1-3	0	0	1	-	0	0	0	0	0	0	0	0	0	0	0	0	0	0	0	0	0	0	0	0	0	0	0	0	0
1-4	0	0	0	1	-	0	0	0	0	0	0	0	0	0	0	0	0	0	0	0	0	0	0	0	0	0	0	0	0
1-5	0	0	0	0	1	-	0	0	0	0	0	0	0	0	0	0	0	0	0	0	0	0	0	0	0	0	0	0	0
1-6	0	0	0	0	0	1	-	0	0	0	0	0	0	0	0	0	0	0	0	0	0	0	0	0	0	0	0	0	0
1-7	0	0	0	0	0	0	1	-	0	0	0	0	0	0	0	0	0	0	0	0	0	0	0	0	0	0	0	0	0
1-8	0	0	0	0	0	0	0	1	-	0	0	0	0	0	0	0	0	0	0	0	0	0	0	0	0	0	0	0	0
1-9	0	0	0	0	0	0	0	0	1	-	0	0	0	0	0	0	0	0	0	0	0	0	0	0	0	0	0	0	0
1-10	0	0	0	0	0	0	0	0	0	1	-	0	0	0	0	0	0	0	0	0	0	0	0	0	0	0	0	0	0
2-1	1	0	0	0	0	0	0	0	0	0	0	-	0	0	0	0	0	0	0	0	0	0	0	0	0	0	0	0	0
2-2	0	0	0	0	0	0	0	0	0	0	0	1	-	0	0	0	0	0	0	0	0	0	0	0	0	0	0	0	0
2-3	0	0	0	0	0	0	0	0	0	0	0	0	1	-	0	0	0	0	0	0	0	0	0	0	0	0	0	0	0
2-4	0	0	0	0	0	0	0	0	0	0	0	0	0	1	-	0	0	0	0	0	0	0	0	0	0	0	0	0	0
2-5	0	0	0	0	0	0	0	0	0	0	0	0	0	0	1	-	0	0	0	0	0	0	0	0	0	0	0	0	0
2-6	0	0	0	0	0	0	0	0	0	0	0	0	0	0	0	1	-	0	0	0	0	0	0	0	0	0	0	0	0
2-7	0	0	0	0	0	0	0	0	0	0	0	0	0	0	0	0	1	-	0	0	0	0	0	0	0	0	0	0	0
2-8	0	0	0	0	0	0	0	0	0	0	0	0	0	0	0	0	0	1	-	0	0	0	0	0	0	0	0	0	0
2-9	0	0	0	0	0	0	0	0	0	0	0	0	0	0	0	0	0	0	1	-	0	0	0	0	0	0	0	0	0
2-10	0	0	0	0	0	0	0	0	0	0	0	0	0	0	0	0	0	0	0	1	-	0	0	0	0	0	0	0	0
3-1	0	0	0	0	0	0	0	a	a	a	0	0	0	0	0	0	0	0	0	0	0	-	b	0	0	0	0	0	0
3-2	0	0	0	0	0	0	0	0	0	0	0	0	0	0	0	0	0	0	0	0	0	a	-	b	0	0	0	0	0
3-3	0	0	0	0	0	0	0	0	0	0	0	0	0	0	0	0	0	0	0	0	0	0	a	-	b	0	0	0	0
3-4	0	0	0	0	0	0	0	0	0	0	0	0	0	0	0	0	0	0	0	0	0	0	0	a	-	b	0	0	0
3-5	0	0	0	0	0	0	0	0	0	0	0	0	0	0	0	0	0	0	0	0	0	0	0	0	a	-	b	0	0
3-6	0	0	0	0	0	0	0	0	0	0	0	0	0	0	0	0	0	0	0	0	0	0	0	0	0	a	-	b	0
3-7	0	0	0	0	0	0	0	0	0	0	0	0	0	0	0	0	0	0	0	0	0	0	0	0	0	0	a	-	b
3-8	0	0	0	0	0	0	0	0	0	0	0	0	0	0	0	0	0	b	b	b	0	0	0	0	0	0	0	a	-

Fig.5. 7 The dependence matrix D.

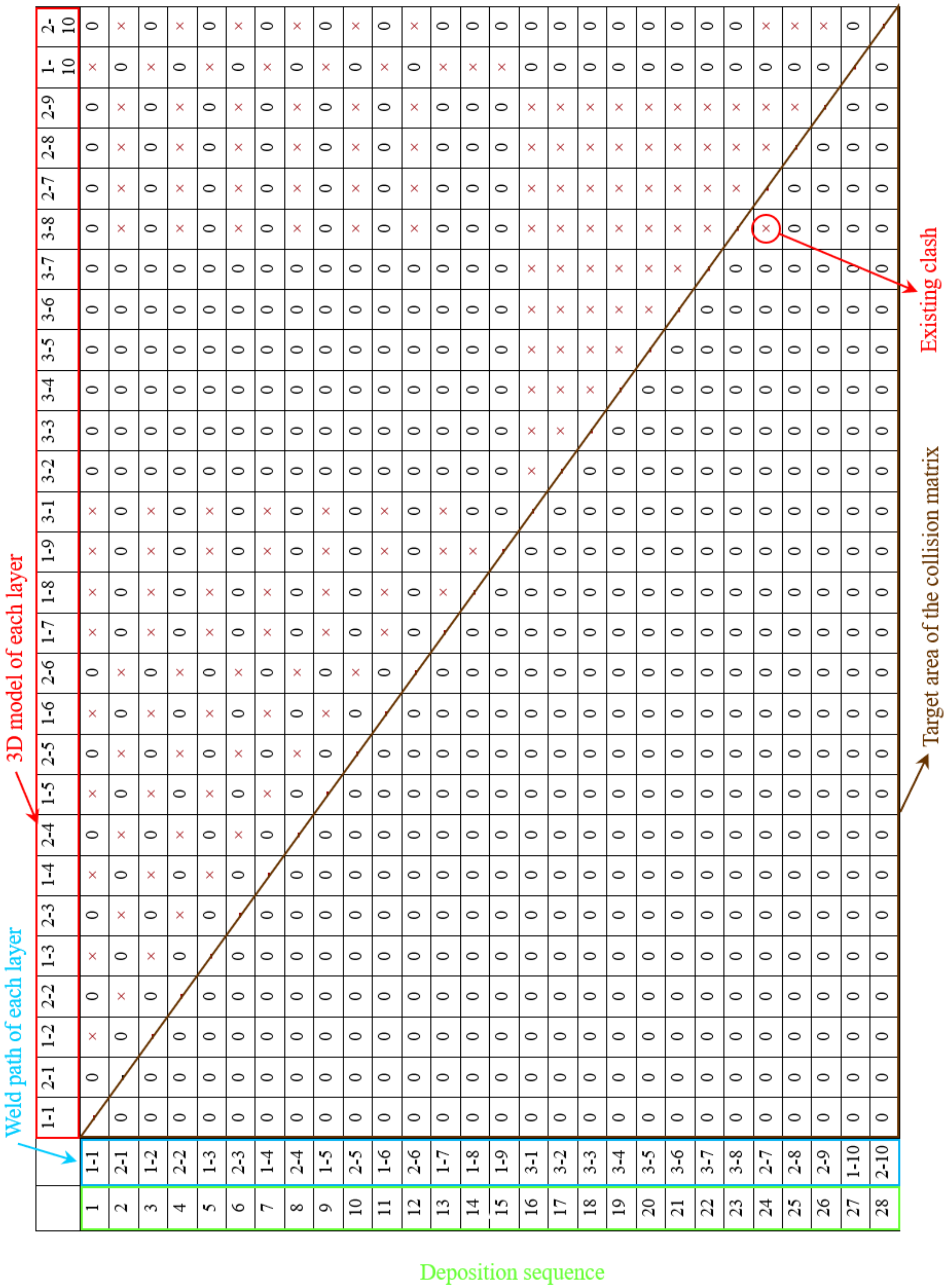

Fig.5. 8 The final collision matrix C with the optimized build sequence.

5.6 Torch pose adjustment

Adjustment of torch pose parameters is performed if the algorithm fails to find a valid build sequence through the search process outlined in section 5.5. By adjusting welding torch angles (within an allowable range), more clearance between the part and torch can be achieved, potentially removing the remaining collision. Three factors must be considered when adjusting the torch pose: (i) The tip of the wire electrode cannot deviate from the designated path during the deposition. (ii) Geometric variations in the weld bead, which can occur as a result of adjusting the torch angle, must remain in an acceptable range. (iii) For a new torch pose, the required robot trajectory must be checked again for reachability and collision.

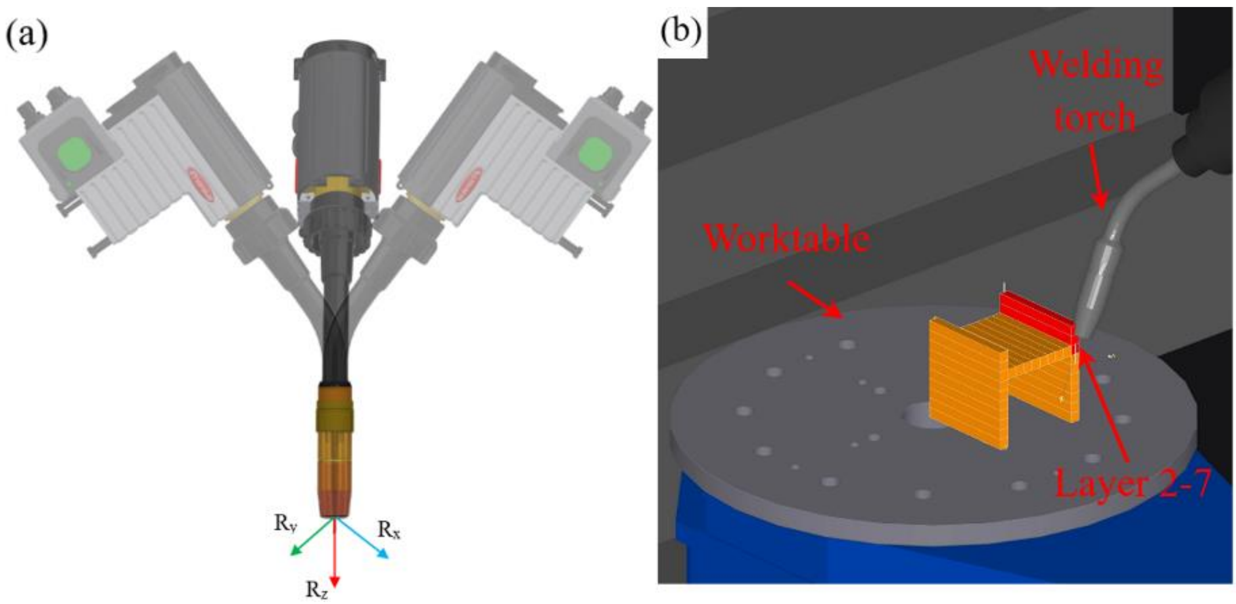

Fig.5. 9 (a) The torch rotation around Rz, and (b) The simulation results with the adjusted torch angle.

As mentioned previously, the robot motion planning algorithm used here is a discretised T-Space, sampling-based, graph searching algorithm. To maintain bead positional accuracy during the deposition process, the torch position X, Y (in the world coordinate frame) must remain constant, while *CTWD*(Z), R_x, R_y, and R_z, are redundant parameters that can be modified (within limits) for collision avoidance purposes. Thus, T-Space is sampled randomly with many combinations of available parameter sets, R_x, R_y, R_z, and *CTWD*. Correct use of the torch angles R_x and R_y are essential in achieving a high-quality weld. So experimental determination of suitable ranges for each of these variables is critical for practical applications. Note that as the tip of the welding gun is symmetric around the wire electrode, rotation around R_z will not affect the deposition process and the resultant geometry of the weld bead, as shown in Fig.5.9(a). Thus, the value of R_z can range from -180° to 180°. The other available parameter adjustment ranges are given based on our experimental tests, below. Finally, the obtained information will be sent to a code translator to generate robot code for a selected industrial robot (we have made templates for many kinds of industrial robot in the code translator for user selection).

For the example part outlined in Fig 5.6, only one collision exists when we enter the torch pose adjustment stage. As shown in collision matrix *C* shown in Fig.5.8, whilst performing the deposition process for layer 2-7, collision with layer 3-8 was detected. Torch angles were adjusted algorithmically, and the required robot motions were updated to avoid this collision. As simulation results in Fig.5.9(b) indicate, the identified collision was removed by implementing a new deposition strategy. Note that the red layers in the figure are layers 2-8 to 2-10, which will be deposited after layer 2-7, meaning they can be ignored.

5.7 Experiment and results

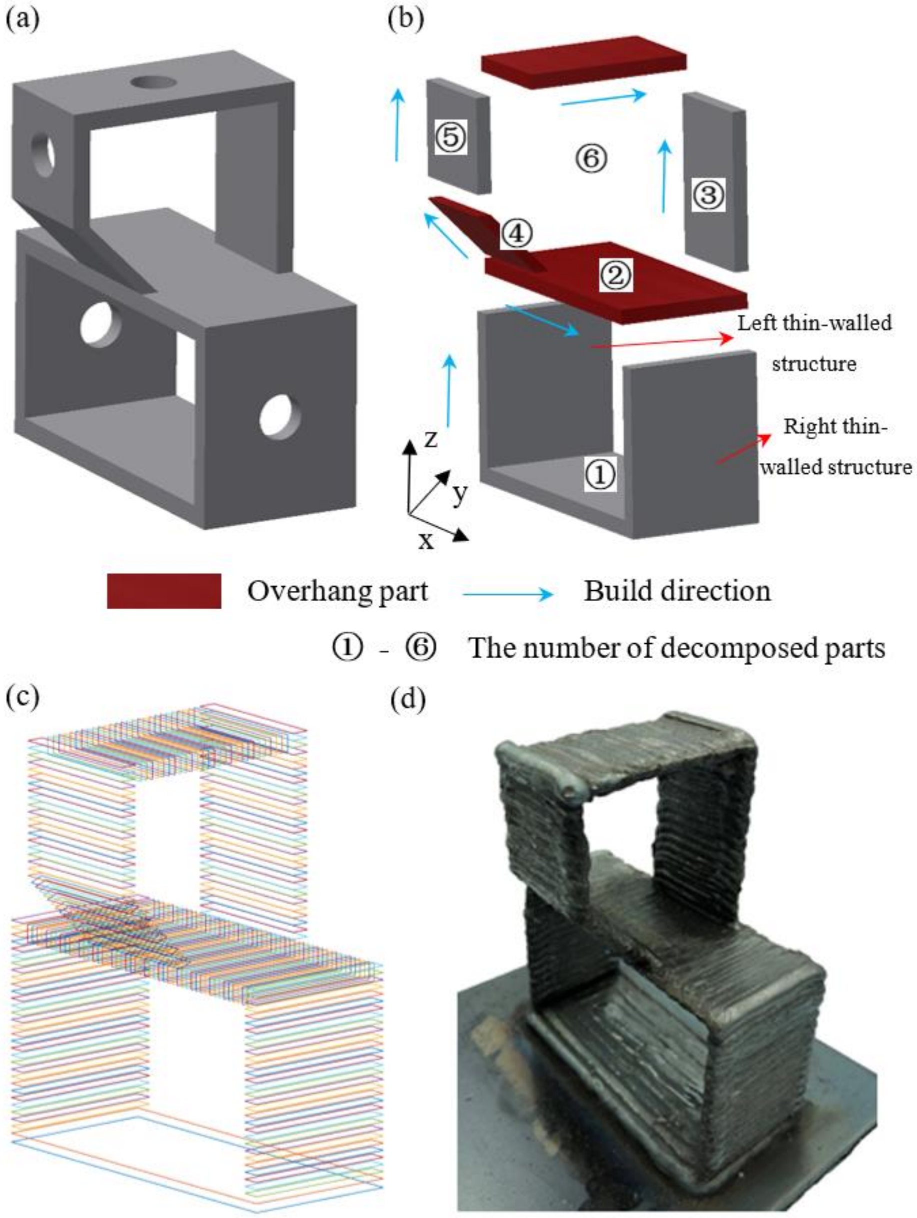

Fig.5. 10 (a) The original CAD model of the workpiece, (b) The decomposed sub-volume, the unbuildable sub-volumes are coloured in red, (c) Each sub-volume is sliced according to its optimal build direction, and (d) The fabricated near-net shape sample.

To test the proposed path planning algorithm, a sample part with overhanging features was fabricated. The CAD model of the workpiece is provided in Fig.5.10(a). The geometries of the two stacked structures indicate that collision between welding torch and previously deposited layers may occur, particularly when depositing the overhanging features. By using the multi-directional slicing algorithm presented in [122], the part was decomposed into six individual sub-volumes. Each sub-volume was identified as buildable or unbuildable sub-volumes (unbuildable sub-volume means it cannot be built along the vertical order). The results of this partitioning is labelled and illustrated in Fig.5.10(b). Note that the CAD model was modified so that the holes on sub-volume 1 were removed. As shown in Fig.5.10(c), each sub-volume is sliced along its optimal build direction, the detailed explanation of the multi-direction slicing algorithm used can be found in [29].

5.7.1 Hardware setups

Fig.5.11 provides the experimental setup for the case study. A 6-DOF ABB IRB 2600 industrial robot is used for executing the welding tasks. The Cold Metal Transfer (CMT)Advanced 4000 welding unit was employed as the welding power source for the system. The welding machine was integrated to the robot control system so that the welding variables (Wire feed speed and torch speed) can be controlled directly from the robot program. An infrared pyrometer was appended to the welding torch to ensure welds are deposited at a consistent temperature. A

LabView computer interface was used as the master control for the robot, welding machine, and infrared pyrometer.

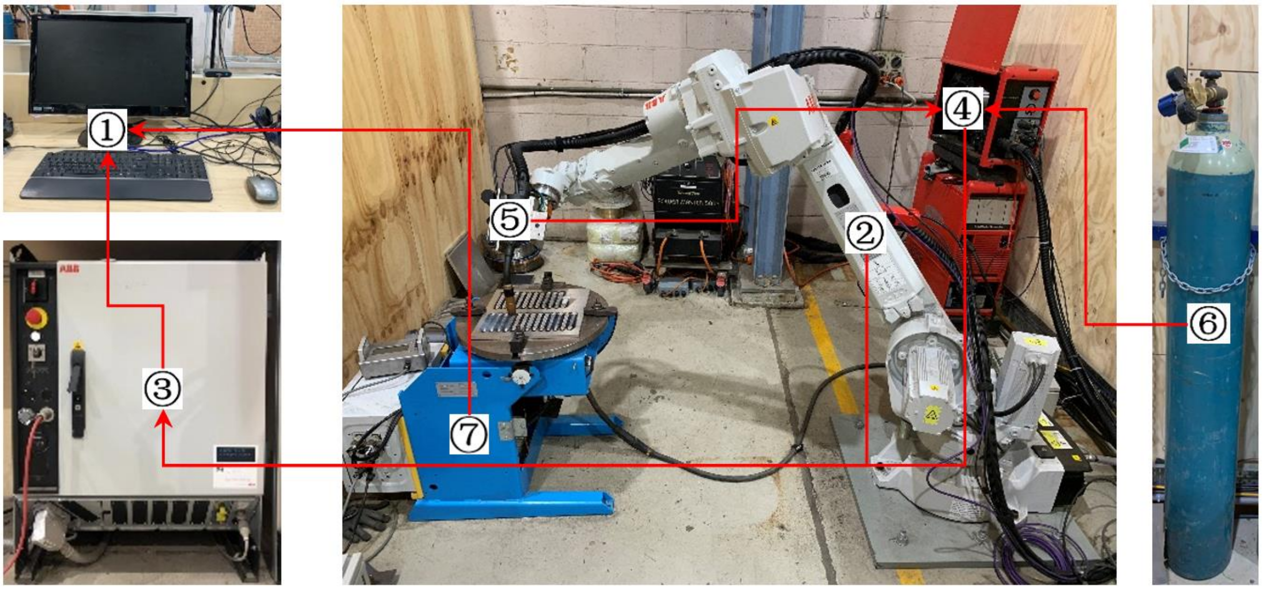

① Computer ② ABB IRB 2600 robot ③ Robot controller
④ Fronius CMT Welding unit ⑤ Welding torch ⑥ Shielding gas
⑦ 2-Axis positioner

Fig.5. 11 The experimental setup.

This work was carried out on a Q235 steel plate with the dimensions of 300×150×10 mm^3. The surface of the substrate plate was ground to remove the oxide layer and impurities. The plain carbon steel welding wire ER70S-6 with the diameter of 0.9 mm was selected as the feed stock. The welding gas Argoshield (Gas code 566, BOC Gases Australia Ltd, Sydney, Australia) consists of 20% Carbon Dioxide and 80% Argon was used at a constant flow rate of 25 L/min.

5.7.2 Implementation and results

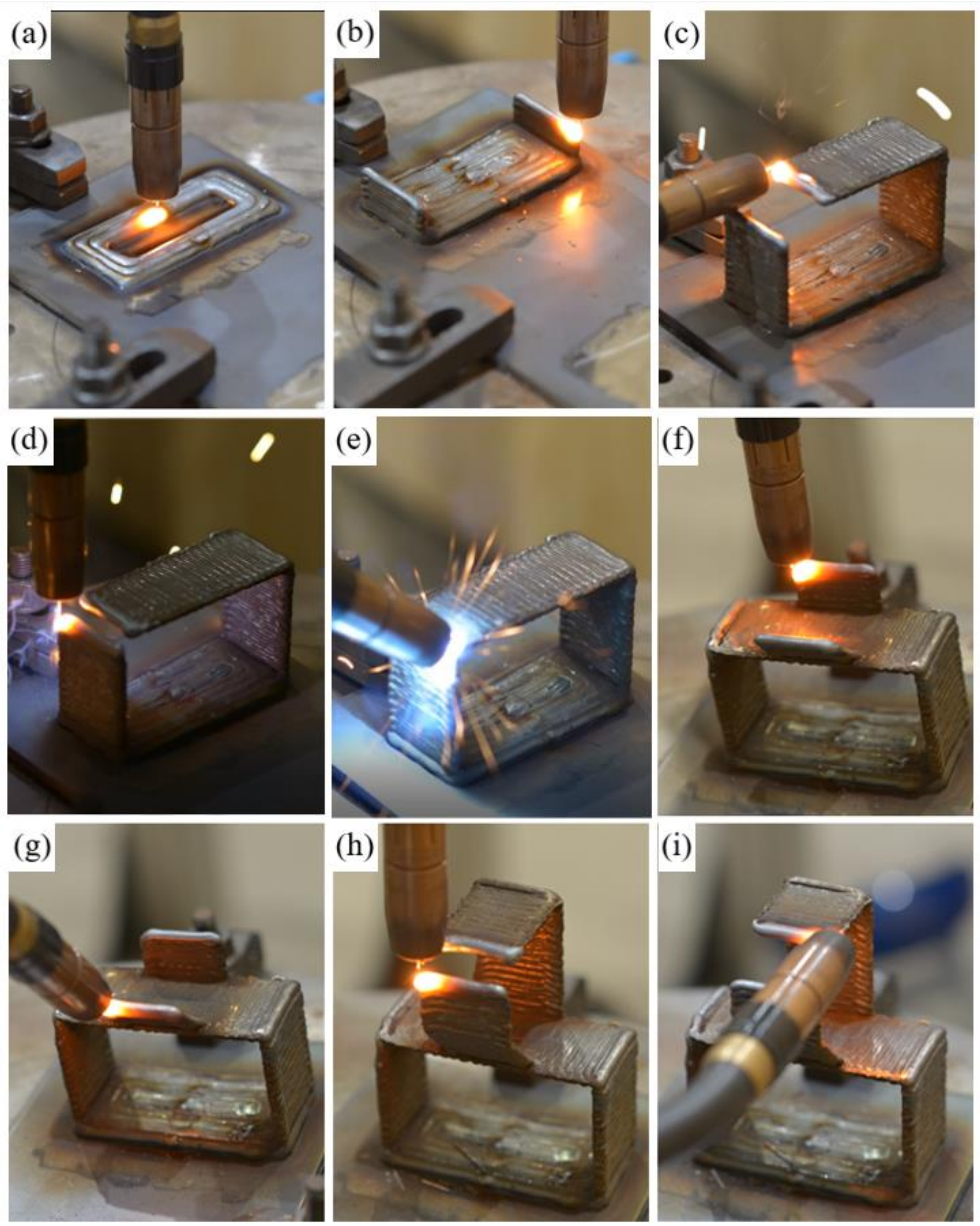

Fig.5. 12 The manufacturing process.

The multi-direction WAAM path planning strategy was implemented to guide the fabrication process. The closed structure of the part strongly indicates collision may occur if a default ‘bottom-to-top’ deposition sequence is used, making it a good test for the proposed algorithm.

Software-based robotic welding applications developed by our research group [89] were used to slice the model into layers and then generate the required robot welding motions for each layer. Following this, the robot-model collision checking module was called to create the collision matrix *C*. According to the generated collision matrix *C*, the final four layers of the sub-volume one will block the deposition of sub-volume two, and the last four layers of sub-volume three will block the deposition of sub-volume six. To address this, the deposition sequence was reordered through the proposed layer sequence optimization module. The final manufacturing process, presented in Fig.5.12(a)-(i), illustrates the optimized build strategy as generated by the overall path planning algorithm. First, the bottom of sub-volume one was built with a vertically aligned torch angle, as shown in Fig.5.12(a). The two vertical walls of sub-volume one were built synchronously, as shown in Fig.5.12(b). However, the vertical wall on the right-hand side was not built to its full extent (the last four layers were not built at this time) in order to give enough space for the welding torch when depositing wall two, as shown in Fig.5.12(c). As the deposition of sub-volume two proceeds, the welding arc gradually moves closer to the right thin-walled structure of sub-volume one. Some action must be made to ensure the welding arc is kept as far away from the other wall as possible. This will help avoid situations where the electron stream will flow (or ‘jump’) across to the other wall structure, and also help maintain a stable welding arc. Thus, in the proposed strategy, the last a few layers of this sub-volume were performed by alternating deposition between the sub-volume two and the right thin-walled structure of sub-volume one, as shown in Fig.5.12(c) and Fig.5.12(d). As the deposition progresses, the algorithm adjusted the torch angle to 45° in order to avoid collision between the torch and previously deposited weld material, as shown in Fig.5.12(e). This was also done for of sub-volumes three, four, five, and six, as shown in Fig.12(f)- Fig.12(i). Fig.5.10(d) presents the near-net shape of the final product, the successful fabrication of the part verifies the performance of the proposed system.

5.7.3 Discussion

For practical applications, some further considerations have been summarised as follows:

1) Some parent sub-volumes, such as the one highlighted in Fig.5.13, need to be extended so that the child sub-volume, which extends from it, can be properly supported. At this stage, these modifications are implemented manually in most of WAAM process. In the proposed system, an automated approach to algorithmically identify these scenarios is developed which based on the build direction of each sub-volume and dependency matrix *D*. then, the robot code can be adjusted accordingly.

2) When reaching a junction between two (or more) sub-volumes, as shown in Fig.5.13, some additional consideration is required. Experimental testing found that the connection

between the two sub-volumes is physically weak. To strengthen this connection, the torch angle should be adjusted to 45°, as shown in Fig.5.13, to allow for simultaneous bonding of both sub-volumes. In the developed algorithm, this junction is be identified through the build directions of each sub-volume, and the torch angle is set to bisect these directions.

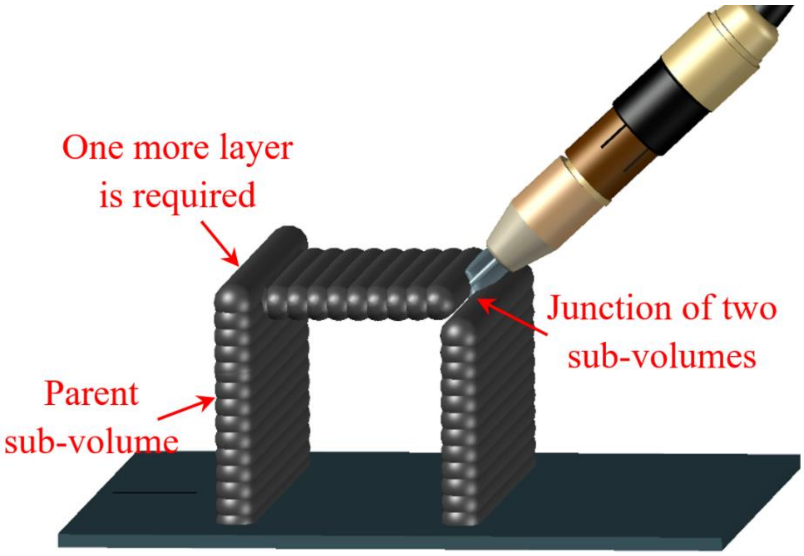

Fig.5. 13 One more layer is recommended to be deposited on parent sub-volume and the torch angle should be adjusted to deposit junction layer.

5.8 Chapter summary

In this chapter, a path planning algorithm for multi-directional WAAM was developed. Experimental tests showed that the proposed algorithm could automatically generate collision free deposition strategies for the fabrication of metallic parts which feature overhanging sections. In this paper, the overall methodology was described first, then, the by four core modules of the algorithm were presented. The function of each sub-module is summarized below.

1) Robot motion planning. An AOLP engine [15] is used to generate valid robot motions for each weld path.

2) Initial collision processing. Once robot trajectories for each layer are planned, the collision between the robot and other layers of the selected part can be tested. The information is stored in a collision matrix *C*, which is used as a heuristic to guide the later stages of the deposition sequence planning.

3) Layer sequence planning. According to the identified collisions in *C*, a series of optimisation routines are used to determine the best available sequence to deposit each layer of the part while minimising collision between the robot, torch, part and environment.

4) Torch pose adjustment. If any collision still exits, the last module of the system will adjust welding torch pose (within a reasonable range) to avoid the remaining collision.

Finally, the developed algorithm was validated through a physical case-study, where a part with complex geometry (i.e. overhangs) was fabricated. The successful manufacturing process demonstrates that the proposed planning system is effective, and it enables the wide industrial use of multi-directional WAAM on manufacturing metallic components.

Chapter 6

Application of multi-directional mobotic wire Arc additive manufacturing process

6.1 Introduction

In the previous chapters, the capability of depositing part at any direction was primarily testified. However, a comprehensive WAAM based positional deposition system has yet to be developed for practical fabrication. In this chapter, a process planning algorithm for multi-directional WAAM based positional process is presented.

6.2 The architecture of the multi-directional WAAM system

Fig.6.1 illustrates architecture of the proposed multi-directional WAAM system from CAD model to the final near-net product. It consists of several essential modules including positional bead modelling, multi-direction slicing, and deposition process optimization which are distinct in multi-directional WAAM process and will be introduced in detail.

Weld bead modelling is the first step in WAAM process establishing the relationship between the process parameters and the weld bead geometry. It provides a database for slicing procedure to select a reasonable layer thickness, for path planning procedure to control the offset distance between adjacent beads, and deposition process to adopt the optimum welding parameters. Several methods, linear regression, second-order regression, artificial neural network, and Taguchi method have been adopted to establish a bead geometry model. Some studies focus on the optimal model for the bead profile in WAAM process [7, 16, 126]. It is found that the weld bead geometry is largely dependent on the selection of wire feed speed and torch travel speed. Although weld bead modelling methods are widely reported in the literature [14, 127, 128], the positional bead modelling regarding the deposition in an arbitrary direction is not developed.

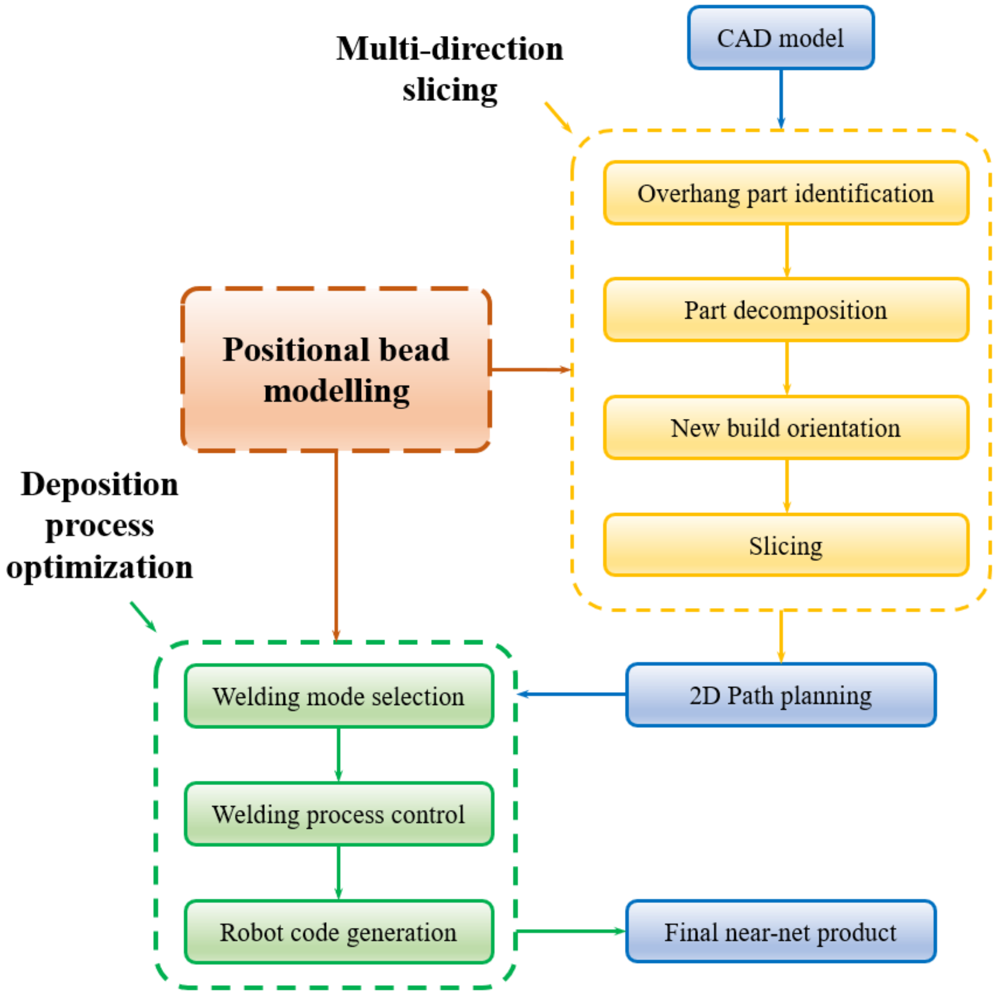

Fig.6. 1 Architecture of the multi-directional WAAM process.

In slicing module, the 3D model in STL format is firstly imported into our in-house MATLAB based WAAM programming software. Multi-direction slicing of a CAD model is another challenge associated with multi-direction deposition process. Ding, et al. [29] developed a new decomposition-regrouping method for multi-direction slicing. After decomposing the CAD model into sub-volumes, a depth-tree structure based on the topology information is introduced to regroup them into new orders for slicing. The proposed method is also proven to be simple and efficient on various tests parts with a large number of holes. More multi-direction slicing methods can be found in Ruan, et al. [30] (Centroid Axis Extraction Method), Yang, et al. [18] (Transition Wall Method), and Dwivedi and Kovacevic [31] (Skeleton Method), etc. The proposed algorithm for obtaining a set of 2.5D layers through a multi-direction slicing method, as shown in Fig.6.1, consists of four steps, including a) Overhanging part identification, the 3D model is divided into buildable and unbuildable sub-volumes according to the user determined initial build direction. b) Determination of build direction for overhangs, the optimal build direction for each overhang is selected. c) Repeat Step 1 to Step 3, all decomposed sub-volumes are buildable along one certain direction. d) Slice all sub-volumes according to their calculated build directions.

In process optimization module, the process control strategy is developed for the welding setups and robot motion planning. The welding setup is the most important step in multi-directional WAAM to form a regular weld bead under unfavorable downward gravitational force, this includes the selection of proper welding mode and welding process parameters. In addition, the robot code generation module is provided to optimize the deposition sequence and collision avoidance during the deposition process.

6.3 Bead modelling system

This section proposes a novel Computer Aided Manufacturing (CAM) system for bead modelling process using arc welding-based AM technology. Weld beads are deposited side by side, as demonstrated in Fig. 6.2, the sliced layer height and offset distance are the same as the desired bead high (BH) and overlapping distance (OD). The proposed system aims to generate optimal welding parameters and setups to produce the user preferred bead geometry.

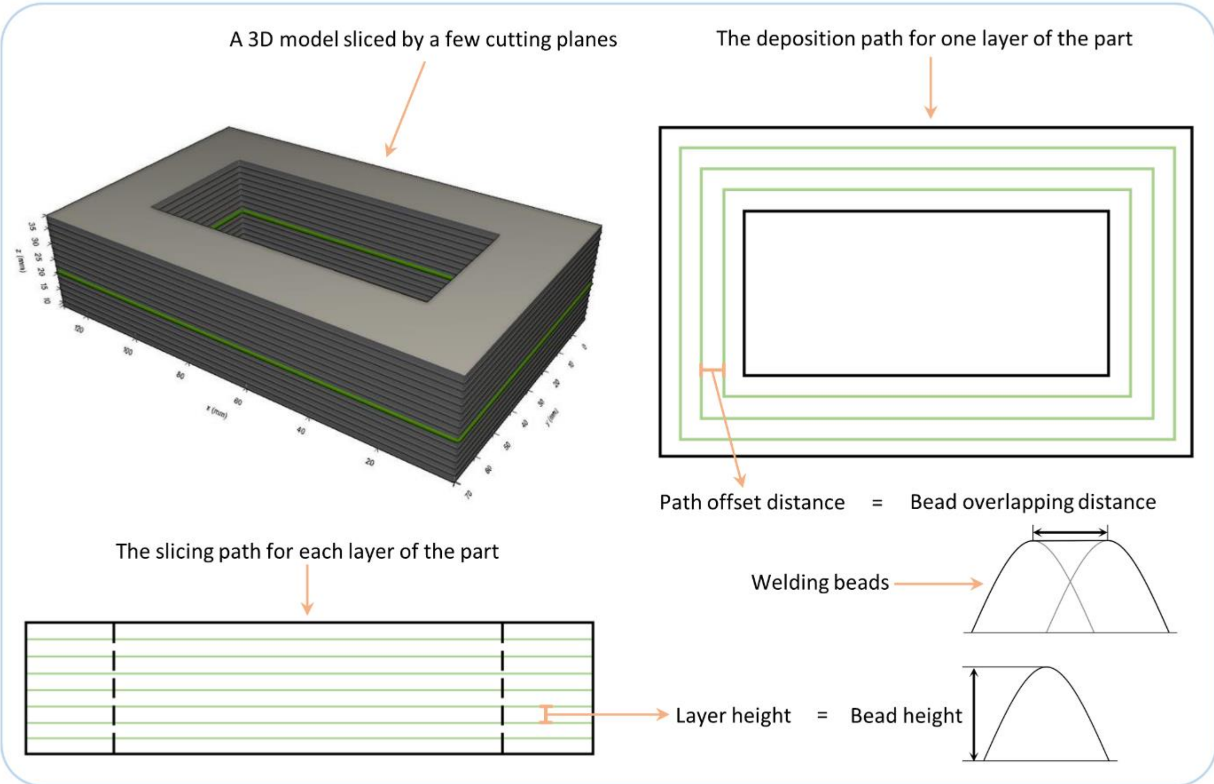

Fig.6. 2 The requirement of overlapping distance and bead height in path planning process

6.3.1 The operation procedure

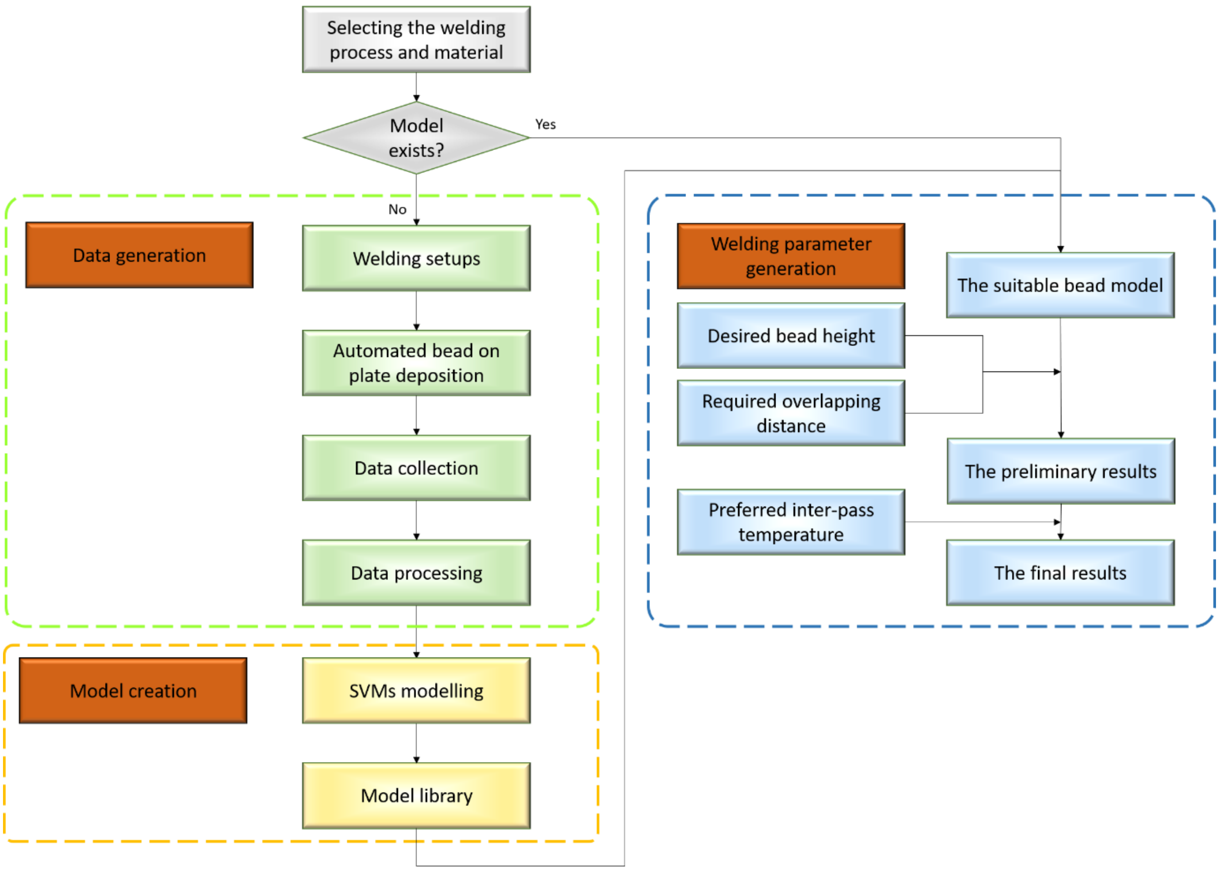

Fig.6. 3 The steps of automated bead modelling process.

The overall workflow of an automated bead modelling process for WAAM system is presented in Fig. 6.3. It consists of three essential modules including, data generation, model creation, and welding parameter generation. All three modules will be called when the weld bead model for selected operation welding mode and filler material does not exist in the current model library. This is because the weld bead morphology indicates that the weld bead geometry is different with different welding methods and filler materials, a new bead model is required to be created. Otherwise, only the welding parameter generation module will be called. The detailed workflow of the system is described as follows:

The Data generation module is used to provide data for model creation, four steps are included from depositing weld beads to obtaining bead geometry information. Firstly, the welding setup, including the range of welding parameters, the length of a single bead, the substrate plate dimensions, etc, are required as user input for the system. Secondly, according to the welding setup, our software can provide an optimal deposition plan for the bead on plate process and then the bead on plate process can be executed automatically. In this step, the user only needs to place the base plate to the predetermined location and start the deposition. Thirdly, the bead profiles are scanned and recorded with a laser scanner. Finally, the raw data of the bead profiles are processed to generate the bead height and optimal overlapping distance with their welding parameters for model creation.

The Model creation module builds bead models based on the obtained data. An Support Vector Machines (SVM) algorithm is used to build up the relationship between welding parameters and bead geometries. Once a model is created, it will be saved and labelled in the model library for use.

The Welding parameter generation module is used to provide the optimal welding process parameters for the deposition process. Firstly, the correct model is selected according to the welding method and filler material. Then, a set of combinations of welding variables for producing the optimal bead geometries can be generated. In addition, in the arc welding based AM process, the optimal inter-pass temperature can improve residual stress and deformation of the deposits [129]. In the developed system, the information of inter-pass temperature can be input to the system for a better quality of the final product.

6.3.2 The hardware of the system

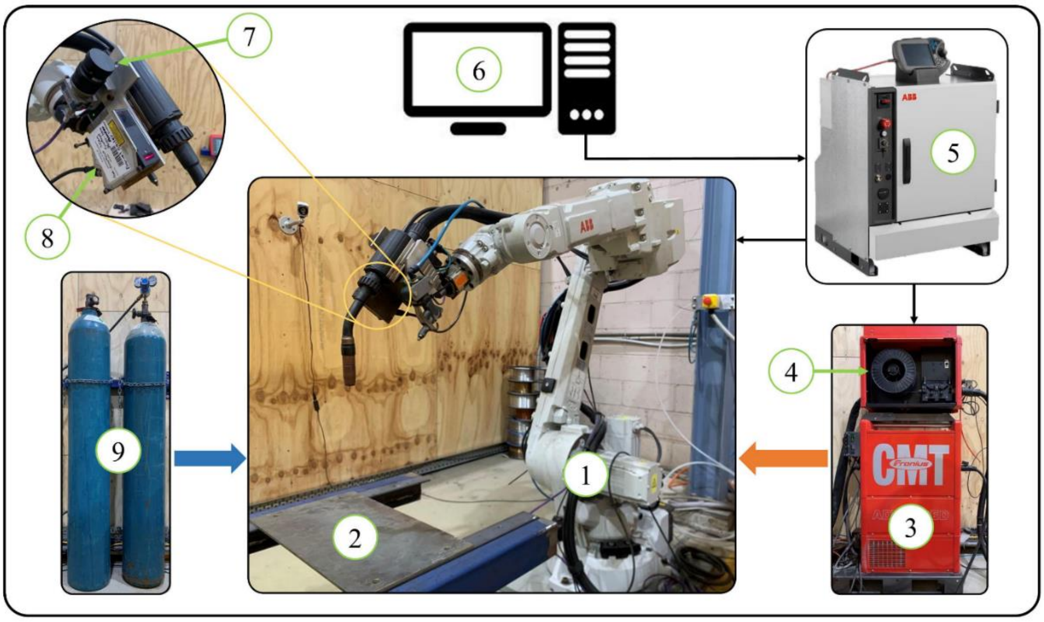

① ABB IRB 2600 industrial robot, ② 2-DoF worktable, ③ Fronius CMT Advanced 4000 welding machine, ④ CMT wire feeder, ⑤ robot controller cabinet, ⑥ control computer, ⑦ camera, ⑧ 3D laser scanner, ⑨ shielding gas.

Fig.6. 4 The WAAM system setup.

The basic hardware of the automated bead modelling system includes an industrial robot, a worktable, a welding machine, a computer, an infrared pyrometer, and a laser scanner. Fig. 6.4 displays the hardware setup for this study. An ABB IRB 2600 industrial robot with six Degrees of Freedom (DoF) is used to hold and move the welding torch along the preprogramed the deposition path. The welding power source is a Fronius CMT Advanced 4000 welding machine with a number of GMAW based welding modes to select from. Robot Studio (simulation and programming software for the ABB robot) was used to program the torch motion and coordinate the weld settings. The base plate is placed on a 2-DoF worktable, note that the position of the worktable is fixed and calibrated carefully to ensure an accurate weld bead position for scanning. A structured light laser scanner is integrated into the robotic welding system to measure the bead profile. An infrared pyrometer was used to monitor the inter-pass temperature. A data acquisition unit and a personal computer serve as the master control for the welding machine, robot, laser scanner, and infrared pyrometer.

6.3.3 Software and user's graphical interface

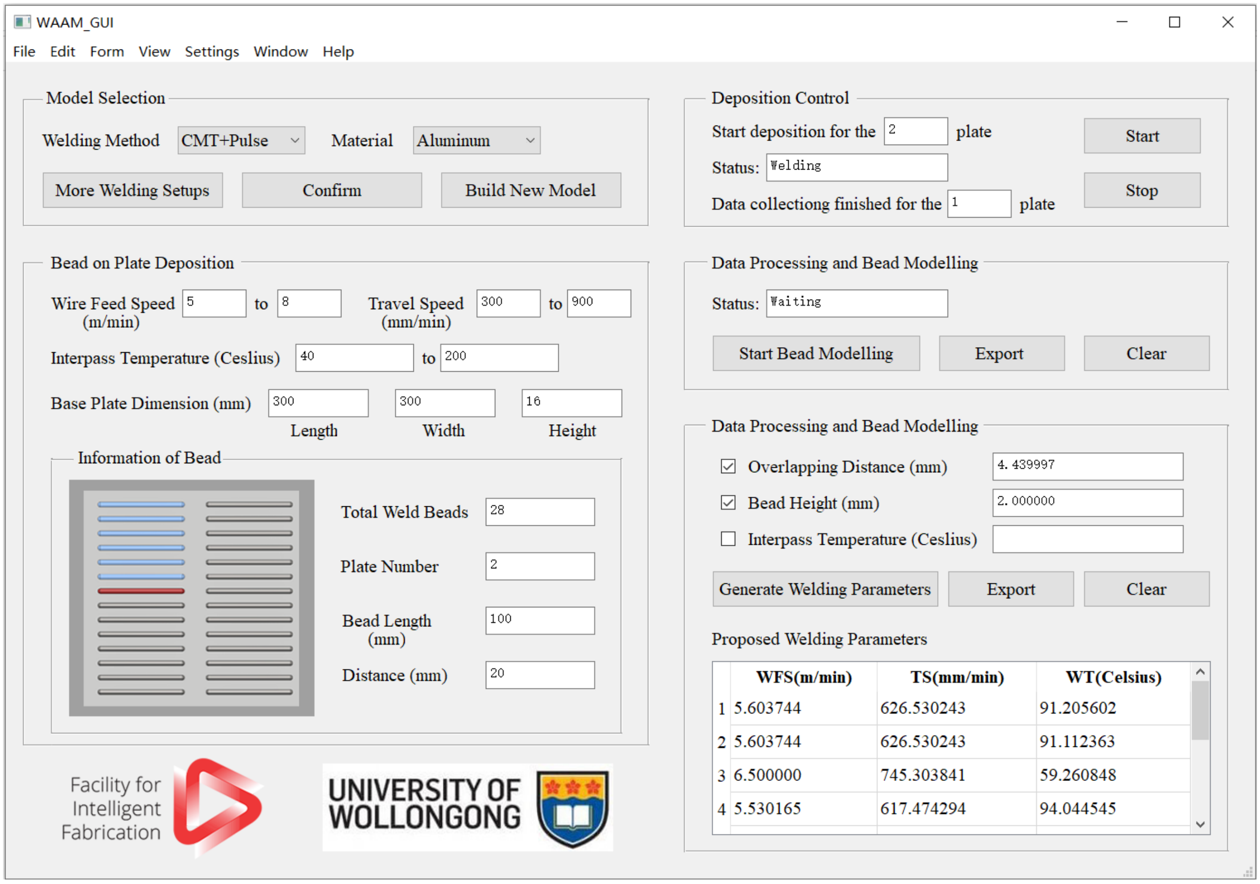

Fig.6. 5 WAAM rapid bead modelling graphical user interface.

Based on the presented workflow in Section 6.3.1, software has been developed for a non-expert operator to monitor and control the bead modelling process, the user-friendly interface is shown in Fig. 6.5. The programming language Python was used to develop the software. Five steps are included as described below.

Step 1, model selection: the user needs to input welding method and filler material to see if the bead model for the selected welding process exists. If the required model exists, the then welding parameters generation model will be loaded and the welding parameters can be generated directly. On the other hand, if the model does not exist, a new model can be saved and named with the welding method and filler material.

Step 2, bead on plate deposition: in this step, the information of the welding setups is required for the bead on plate deposition, including welding parameters range (Wire Feed Speed (WFS), Travel Speed of the torch (TS), and inter-pass temperature (WT)), and dimensions of the base plate. With the inputs, a preview image of the distribution of weld beads on plate process is shown. More detailed information, the total number of weld beads and base plate, length of each weld bead, and offset distance of the adjacent bead, can be provided automatically.

Step 3, deposition control: this step is used to monitor and control the bead deposition and data collection process. Once the operator places the plate on the working table, the entire deposition and data collection process will be executed automatically.

Step 4, data processing and bead modelling: the OD and BH of each weld bead can be generated by processing the raw data of the weld bead profile. Then, the bead model is trained using the SVM based algorithm and it is saved to the model library to the system.

Step 5, welding parameter generation: Once a new model is exported to the library for a specific welding task, the user can obtain the optimized welding parameters by inputting the required bead overlapping distance, bead height, and inter-pass temperature.

6.3.4 Data collection

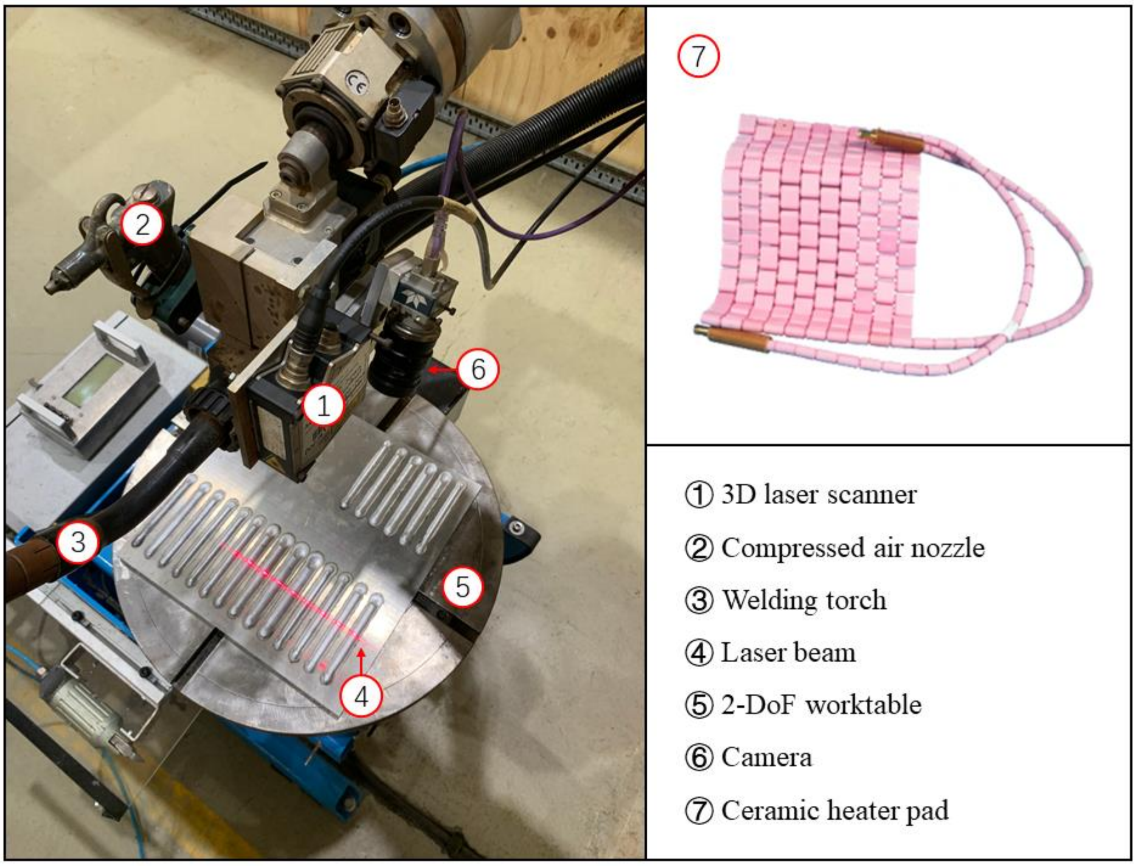

Fig.6. 6 Weld bead profiles collection using the laser scanner.

Firstly, a set of weld beads are deposited with the designated welding parameters. According to the dimensions of the base plate, the length of each bead is 100mm. The distances between adjacent beads and columns are set to 30 mm and 40 mm. The detailed arrangement of bead locations is presented in Fig. 6.5. In the deposition process, movements of the welding torch are automatically programmed in the robot controller. The welding parameters, such as WFS and TS, are automatically set to the designated values for each deposit. It is worth mentioning that a temperature control system is used in the deposition process, a thermal pyrometer is used to monitor the inter-pass temperature. A ceramic heater pad and compressed air nozzle are applied to heat up or cool down the base plate to the designate inter-pass temperature. A laser scanner is used to measure the profile of beads, as illustrated in Fig. 6.6. It scans the weld beads along the weld path and records the transverse bead profile of each weld bead.

6.3.5 Data processing

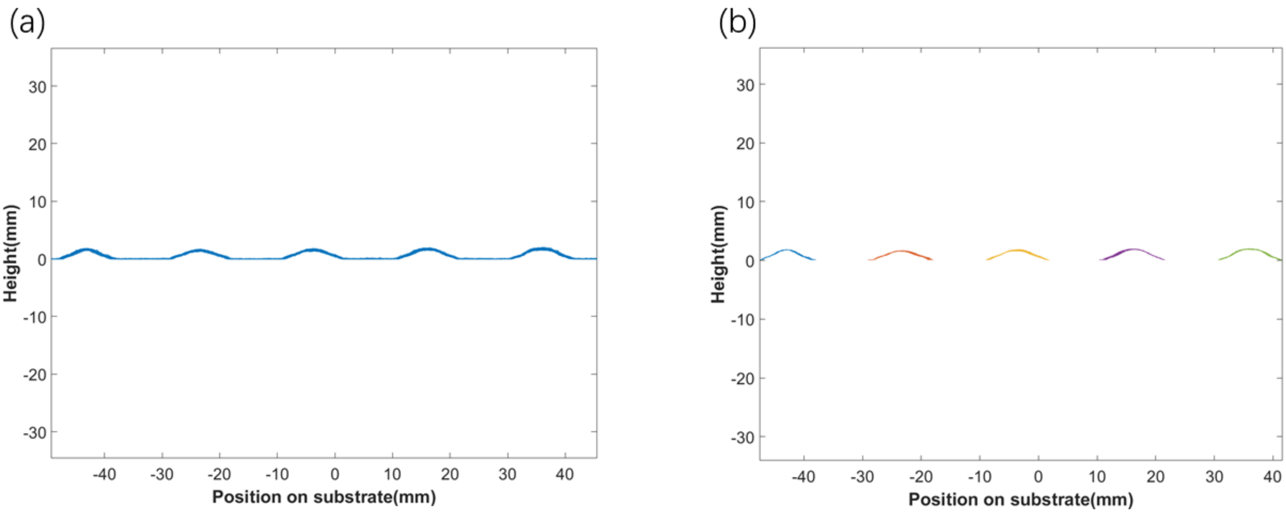

Fig.6. 7 Bead profile denoise and extraction.

The target of the data processing is to obtain the OD and BH through the raw data of weld bead profile. In order to depict the geometry of weld beads accurately, a data processing algorithm was proposed. It includes: (i) a signal denoising filter, (ii) bead profile extraction, (iii) Curve fitting process, and (iv) Generation of the OD and BH.

Step 1, signal denoising. As noise is inevitably recorded by the laser scanner, a moving average filter is used for smoothing raw data. The moving average filter is a type of low pass finite impulse response filter (LPF) which can be used for regulating an array of sampled data. The LPF uses Hamming window with the sampling frequency and cut-off frequency were set to *10000Hz* and *400Hz* respectively. Most of the noise points in the data set are removed after filtering. The processed data after denoising is presented in Fig. 6.7(a).

Step 2, bead profile extraction. As a number of weld beads are scanned simultaneously by the laser scanner as shown in Fig. 6.7(a), a boundary detection program was developed to extract single bead profile in each data set. Firstly, the boundaries of each weld bead are identified by calculating the change rate of slope in the y-axis. Points between the left and right boundary are saved to represent the weld bead profiles, as shown in Fig. 6.7(b).

Step 3, curve fitting process. To obtain OD and BH accurately, accurate weld bead profiles are required. Thus, the weld bead profile data from the laser scanner needs to be further processed. Commonly, various functions are used to fit the cross-section of the weld bead. In the research by Xiong, et al. [130], the parabola, arc, and cosine functions can be applied to build the profile of the weld bead. In our previous study [131], a number of curve fitting methods were used to create bead profile models. Through the comparison of the developed model, the experimental results reveal both parabola and cosine functions accurately represent the bead profile. In our study, the parabola function was chosen to fit the cross-section of weld bead. The fitted parabola function can be represented by

$$y_1 = -ax^2 + c \tag{6.1}$$

Step 4, generation of the bead overlapping distance. In the practical deposition process, the BH and OD are used to determine the layer height and offset distance between adjacent weld path. The BH can be obtained by searching the vertex coordinates of each parabolas function directly. Fig. 6.8(a)-(c) illustrate the principle of generating OD. As described in Fig. 6.8(a), two identical welding beads are deposited next to each other with the offset distance *d*. Based on the polynomial fitting result in Step 3, the parabola function which can represent the adjacent bead profile is shown as below

$$y_2 = -a(x-d)^2 + c \tag{6.2}$$

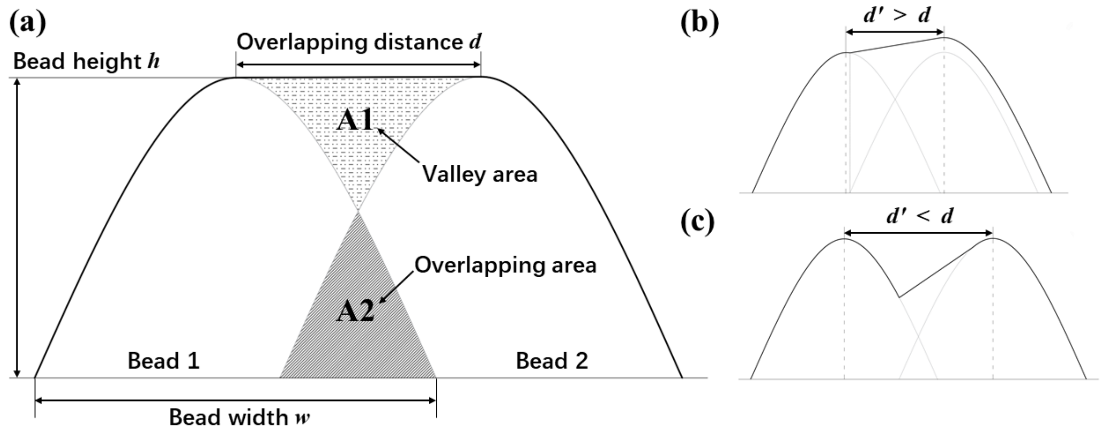

Fig.6. 8 Schematic diagrams of the tangent overlapping model (TOM).

To generate a flat layer surface, an optimal value of $d=d'$ should be selected so that the critical valley area A_1 equals to the overlapping area A_2. A_1 and A_2 can be calculated as:

$$A_1 = cd - \int_0^{\frac{d}{2}}(-ax^2+c)\,dx - \int_{\frac{d}{2}}^{d}[-a(x-d)^2+c]\,dx = \frac{ad^3}{12} \tag{6.3}$$

$$A_2 = \int_{\frac{d}{2}}^{\sqrt{\frac{c}{a}}}(-ax^2+c)\,dx + \int_{d-\sqrt{\frac{c}{a}}}^{\frac{d}{2}}[-a(x-d)^2+c]\,dx$$

$$= \frac{ad^3}{12} + ad^2\sqrt{\frac{c}{a}} - a\sqrt{\frac{c}{a}} + \frac{4}{3}c\sqrt{\frac{c}{a}} - cd \tag{6.4}$$

when $A_1 = A_2$, d' is

$$d' = \frac{\sqrt{ac} \pm \sqrt{4a^2 - \frac{13}{3}ac}}{2a} \tag{6.5}$$

Fig. 6.8(b) and (c) illustrate that swellings valleys and valleys form when $d' > d$ and $d' < d$. Finally, d' will be recorded into the library as the OD for the selected weld bead profile. A set of ODs and BHs with their corresponding welding parameters will be sent to SVR based model creation process.

Table 6. 1 The process parameters and geometry information of weld bead with mild steel ER70s-6.

Process parameters				Measured geometry		Predicted geometry		Modelling error	
Index	WFS (m/min)	TS (m/min)	Ratio	h (mm)	w (mm)	h' (mm)	w' (mm)	e_h (%)	e_w (%)
1	1	0.1	10	2.23	3.13	2.22	3.16	-0.45	0.95
2	2	0.1	20	2.35	5.32	2.40	5.28	2.13	-0.75
3	3	0.1	30	2.60	6.53	2.55	6.57	-1.92	0.61
4	4	0.1	40	2.68	7.07	2.69	7.03	0.37	-0.56
5	1	0.2	5	-	-	-	-	-	-
6	2	0.2	10	1.61	3.65	1.59	3.60	-1.24	-1.37
7	3	0.2	15	1.88	5.05	1.89	5.03	0.53	-0.40
8	4	0.2	20	2.14	5.57	2.16	5.63	0.93	1.08
9	1	0.3	3.33	-	-	-	-	-	-
10	2	0.3	6.67	-	-	-	-	-	-
11	3	0.3	10	1.58	4.06	1.60	4.16	1.26	2.46
12	4	0.3	13.3	2.04	4.91	2.02	4.85	-0.98	-1.22

6.4 Multi-direction slicing strategy

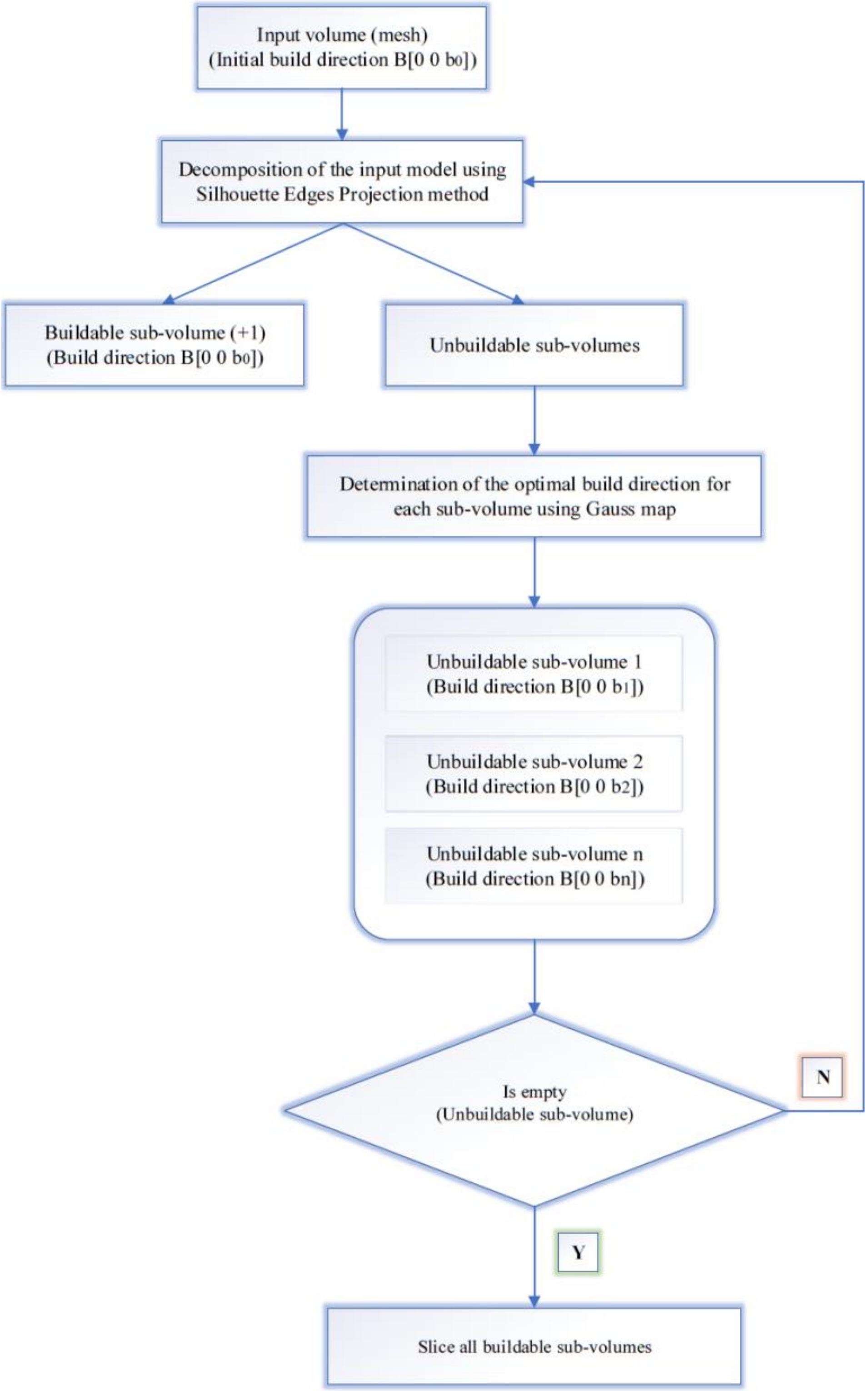

Fig.6. 9 The flowchart of the multi-direction slicing method.

One of the critical steps of multi-directional WAAM process is multi-direction slicing algorithm. Primarily, the slicing method should be able to decompose 3D model into a set of optimal sub-volumes and generate sliced layers along the most suitable deposition directions of the sub-volumes. Based on our previous study [29], a modified multi-direction slicing strategy is developed for fabricating complex structures. Main steps of the slicing strategy are presented in Fig.6.9 and introduced as follows.

Step 1, Creation of the build direction. The initial build direction (or orientation) of the model is determined manually according to the user experiences. The build direction B [0 0 1] is adopted for the input model as shown in Fig.6.10(a).

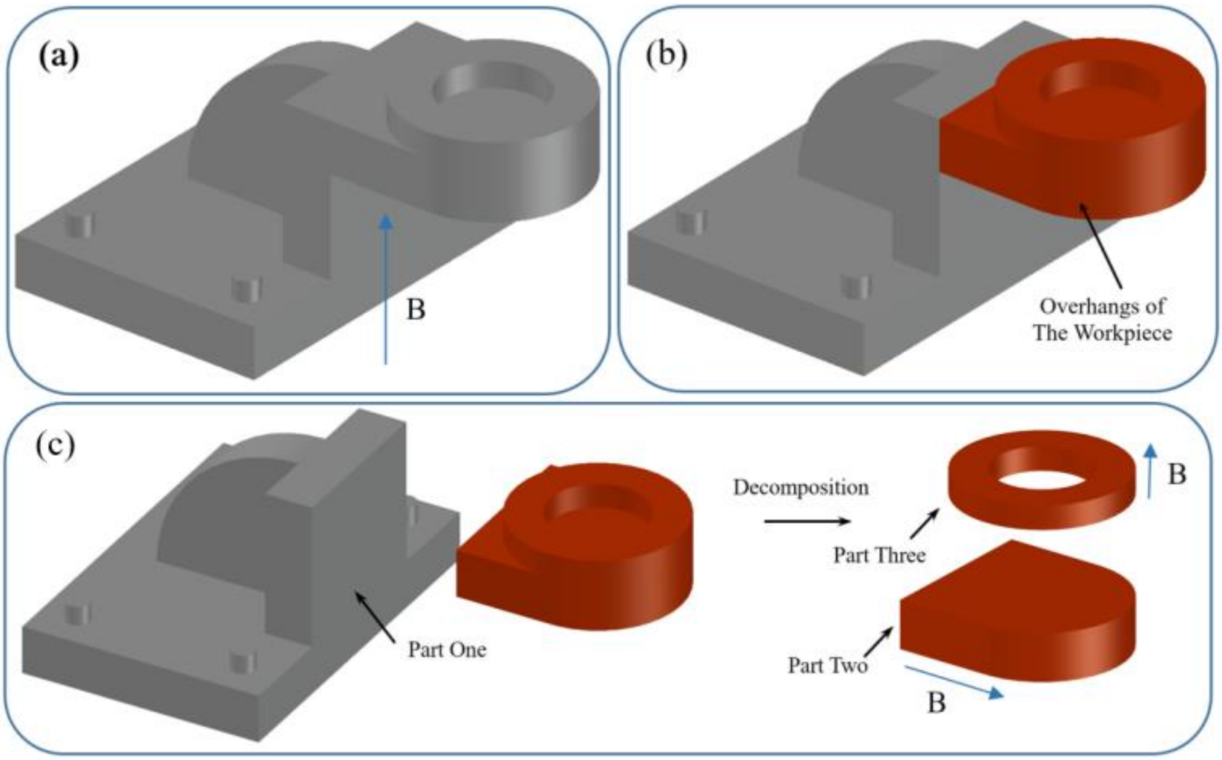

Fig.6. 10 (a) the overall build direction, (b)The unbuildable sub-volume of the model, and (c) The decomposed unbuildable sub-volumes and their new build directions.

Step 2, Overhangs identification. Overhangs of the input model along the build direction are identified using the Silhouette Edges Projection method [19]. Through the silhouette edges projection method, the input model can be divided into buildable and unbuildable parts along a certain build direction. Fig.6.10(b) shows the unbuildable sub-volume (in red) of the input 3D model. The unbuildable part is identified as the overhanging part and therefore decomposed from the input model as shown in Fig.6.10(c).

Step 3, Determination of build direction for overhangs. Gauss Map method is adopted to identify the optimal build directions for sub-volumes (overhangs). For the unbuildable sub-volumes, the optimal build orientation can be determined using Gauss map. The Gauss map method provides normal vectors from all points on a curve or a surface to a corresponding point on a unit sphere [117, 132]. A spherical crown with a minimum radius bottom surface that contains all the points can be found on the sphere surface, the unit vector from the center of the sphere to the center of the bottom circle of the spherical crown C is the desired optimal build direction. The detailed description of the Gauss mapping procedure can be found in [117, 132]. Fig.6.10(c) demonstrates the ideal build orientation for the overhanging parts.

Step 4, Repeat Step 1 to Step 3, in this step the overhangs is used as input model. The

Step 4 stops unless all decomposed sub-volumes are buildable along certain directions.

Step 5, Slice all sub-volumes according their build directions. In the slicing procedure, the in-house MATLAB based is used to slice each sub-volume along its identified orientation using facet-plane slicing method [133]. Normally, the intersection line between the facet and cutting plane can be calculated along vertical-up direction or z [0 0 1] axis. Note that the distance between adjacent slicing planes is also called layer thickness. The layer thickness information obtained from previous bead modelling process is considered as a user input for 3D model slicing. Fig.6.11(a) shows the sliced layers of the substrate sub-volumes along vertical-up direction with the input layer thickness. To slice other sub-volumes in their optimal build direction, the normal vector of the cutting plane needs to be rotated parallel to the build direction. Rotation matrices are used to transfer normal vector of the cutting plane P, as expressed in (6.6) to (6.8), three 3-by-3 matrices M_x, M_y, and M_z are used to represent plane rotations by angles α, θ, and γ about the x-, y-, and z-axis, respectively. With the help of rotation matrices, the cutting plane P is transformed to the new cutting plane $P_{new}=M_xM_yM_zP$ for the slicing of the volume along the corresponding new direction. Finally, the rest of the sub-volumes are sliced according to their identified build orientations, as presented in Fig.6.11(b).

$$M_x = \begin{pmatrix} 1 & 0 & 0 \\ 0 & \cos(\alpha) & -\sin(\alpha) \\ 0 & \sin(\alpha) & \cos(\alpha) \end{pmatrix} \tag{6.6}$$

$$M_y = \begin{pmatrix} \cos(\theta) & 0 & \sin(\theta) \\ 0 & 1 & 0 \\ -\sin(\theta) & 0 & \cos(\theta) \end{pmatrix} \tag{6.7}$$

$$M_z = \begin{pmatrix} \cos(\gamma) & -\sin(\gamma) & 0 \\ \sin(\gamma) & \cos(\theta) & 0 \\ 0 & 0 & 1 \end{pmatrix} \tag{6.8}$$

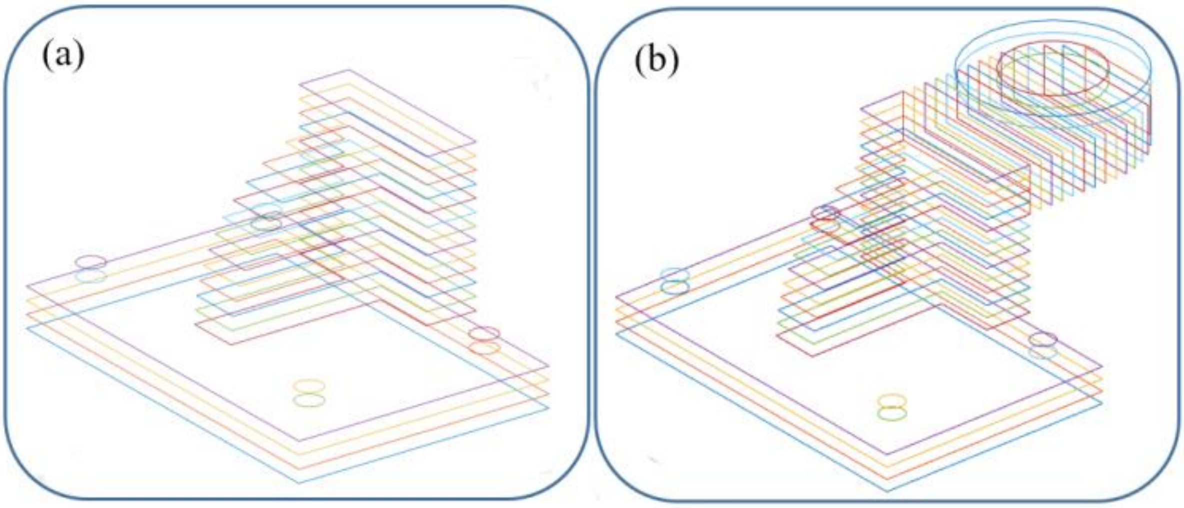

Fig.6. 11 (a) The buildable sub-volume sliced in vertical-up direction and (b) The entire 3D model sliced in multi-direction.

6.5 Robot code generation

The robot code generation module generates collision-free robot motions from 3D model of the robotic system, torch and work piece. Fig.6.12 presents the overall flowchart of the robot motion planning in multi-directional WAAM. The input of the system is the position information and its build direction obtained from the multi-direction slicing process. Layers of each sub-volume are placed into an original layer pool according to their z coordinates. The collision between the welding torch and the previous deposited layers can be resolved through layer sequence sorting and/or torch pose adjustment. To help understand the workflow, the major steps of the algorithm are as follow:

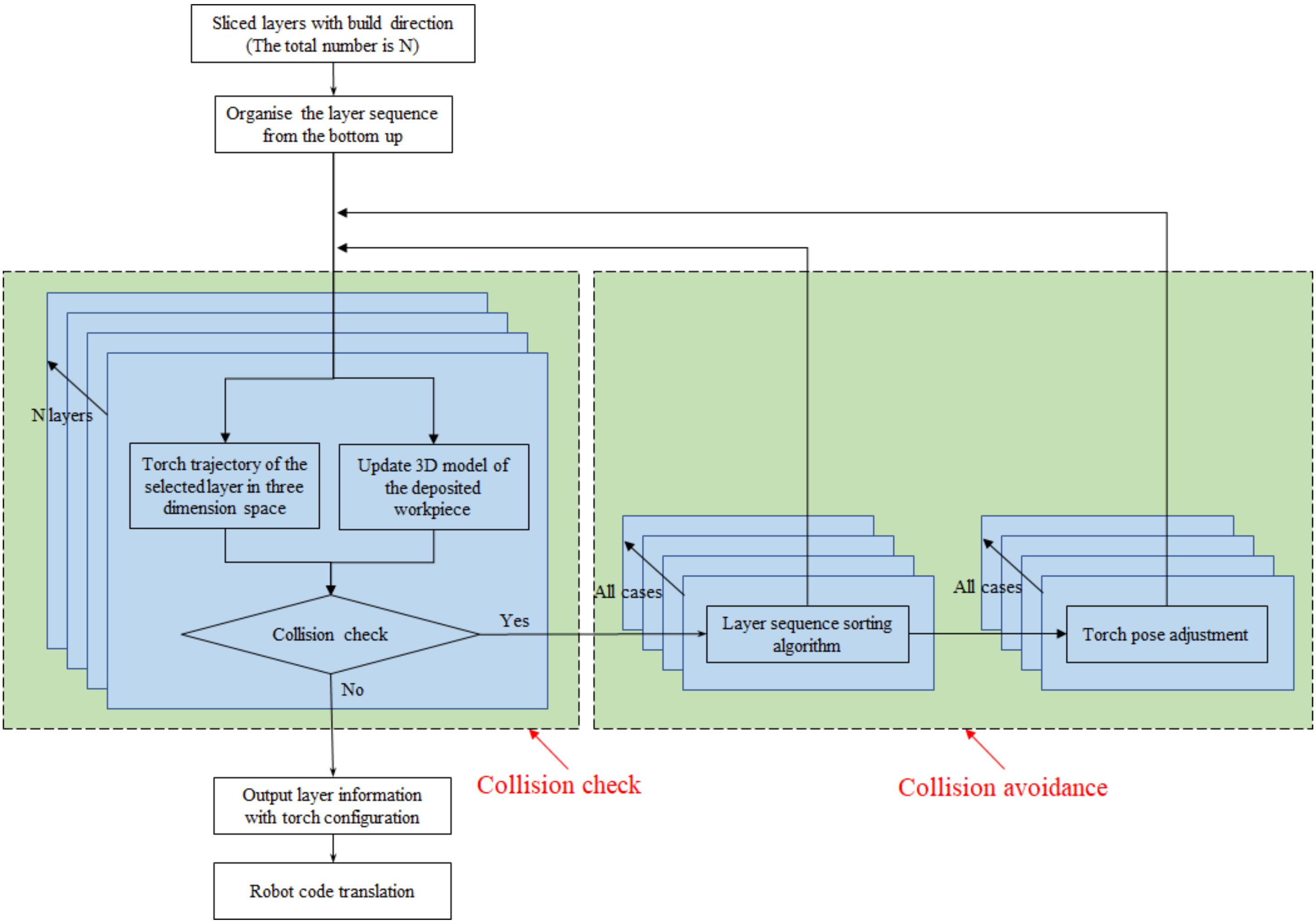

Fig.6. 12 Flowchart of the robot motion planning.

1) *The collision check module*. The collision mainly happens between robot, the welding torch and the workpiece. The 3D model of the robot and torch are readily available and

imported to robot motion planning program. The trajectory of the welding torch is the same as the welding path with a distance offset of contact tip to work distance (CTWD) and the orientation is the same as the build direction. At each torch position, the robot joint angles can be obtained from inverse kinematics. After each deposition, the 3D model of the deposited workpiece is updated with newly deposited layer through 3D re-construction from 2D sliced layer. If no collision is detected, the next layer will be tested, otherwise the collision avoidance module will be called, which includes layer sequence sorting and torch pose adjustment module.

2) *Layer sequence sorting module*. When collision is detected, the layer sequence will be reorganised and send back to collision check module. As the layers are added from the bottom to the top and welding torch are approaching from the top (worst case horizontal direction), the collision will only occur at the top few layers during the collision check, there is only a few combinations for the layer sequence of clashed layers.

3) *Torch pose adjustment*. If collision still exist after checking all the combinations of clashed layers, torch pose can be adjusted to avoid the collision. The collision problem in multi-direction WAAM is formulated as a T-space motion planning problem as the path has workspace constraints such as the actual desired weld path and the weld gun angles specified in the weld procedure. The details of T-space motion planning problem can be found in [134]. As introduced in [88], the torch position X, Y, determine the bead positional accuracy, while Z (CTWD), and torch orientation, R_x, R_y, and R_z, are redundant Degree of Freedoms (DOFs) that can be adjusted without affecting the welding accuracy. A set of new torch poses parameters can be generated by our

software, and the optimal solution with the minimum change will be selected to update the layer pool.

4) *Robot code translation*. Finally, the path positions and torch poses of each layer pool are translated to ABB robot language as subroutines. A main routine calls subroutines according to the updated layer sequence to deposit the input model without collision.

6.6 Case study

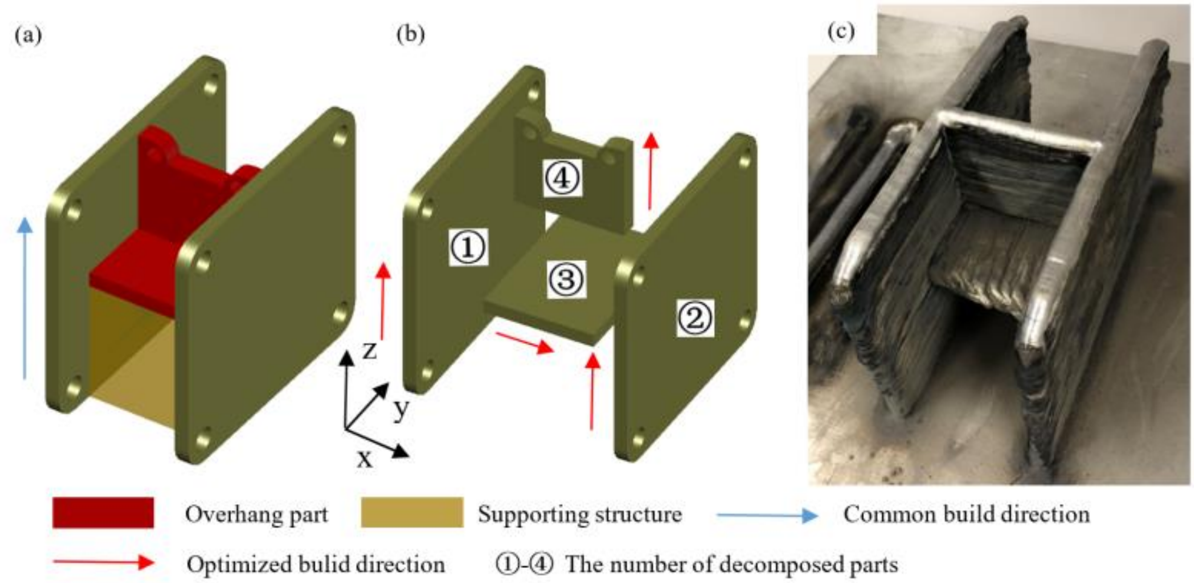

Fig.6. 13 (a) 3D model of workpiece and its overhang part and required supports in vertical-up build direction, (b) The optimal build direction of each sub-volume, and (c) The final near-net product.

The performance of the proposed multi-directional WAAM strategy is demonstrated through fabricating a thin-walled workpiece with overhangs. The 3D model of the workpiece and the necessary supports for conventional vertical-up deposition are illustrated in Fig.6.13(a). The component is identified as buildable and unbuildable sub-volumes first, and the unbuildable sub-volume is further decomposed into two parts as shown in Fig.6.13(b). Based on the proposed multi-direction slicing strategy, the build orientations are identified as vertical-up direction along z axis [0 0 1] for sub-volume one, two, and four, while the horizontal direction along x axis [1 0 0] is identified for the sub-volume three.

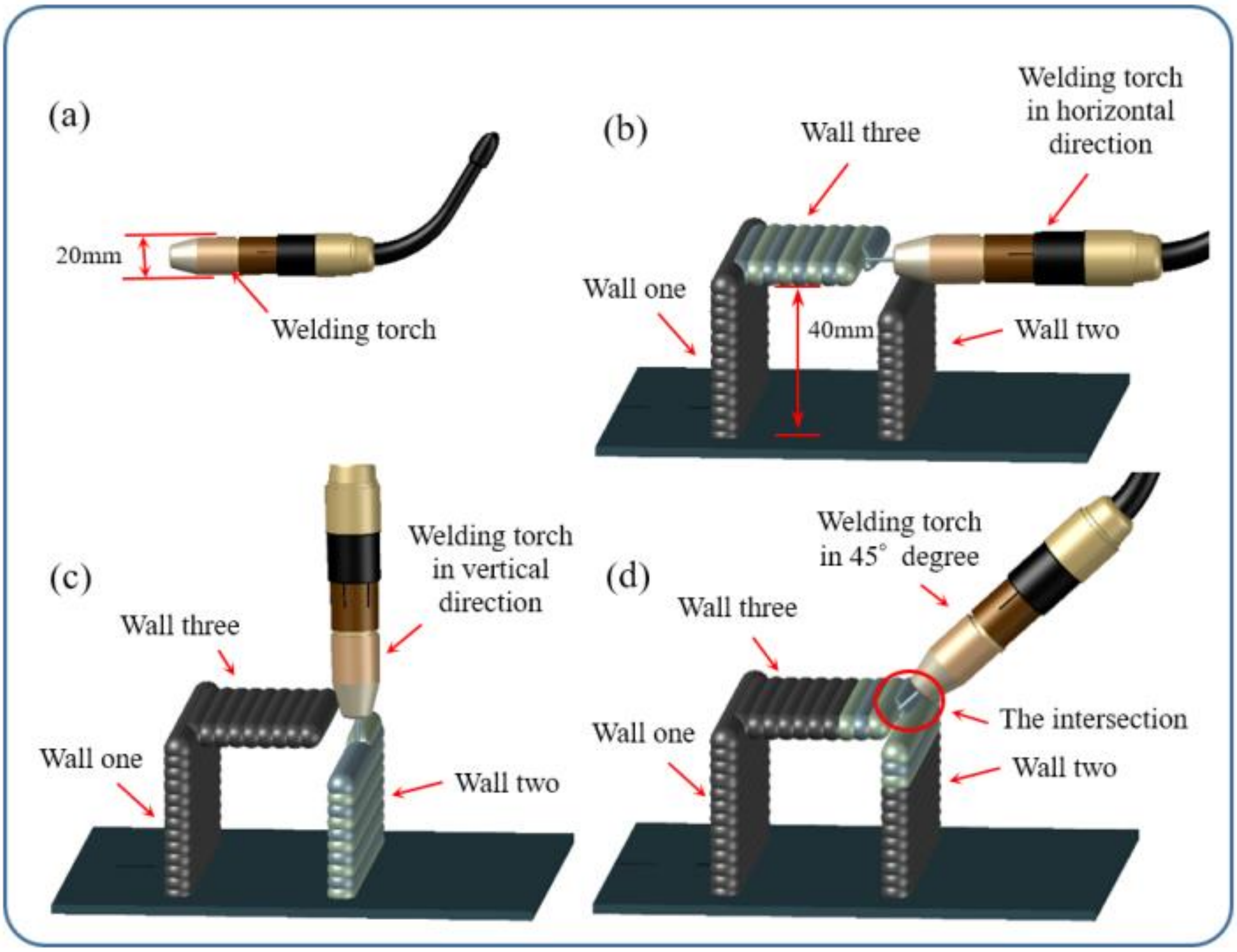

Fig.6. 14 The building sequence of the third component (a) the dimension of welding torch, (b) the diagram of horizontal deposition, (c) the diagram of vertical deposition, and (d) the connection between wall two and three.

Table 6. 2 The manufacturing information of case study.

Material		Wire diameter		Shielding gas		Flow rate
Aluminum 4043		1.2mm		Pure argon		20L/min
Process parameters				Geometry information		
Part No.	WFS (m/min)	TS (m/min)	Ratio	Layer height (mm)	Bead width (mm)	No. of layers
1	6.0	0.2	30	3.0	7.8	35
2	6.0	0.2	30	3.0	7.8	35
3	2.0	0.1	20	2.6	4.5	21
4	6.0	0.2	30	3.0	7.8	18

The key step of the deposition process is to bridge the gap between the wall one and the wall two. An overhanging horizontal wall is required to build such a part. To reduce the manufacturing time, a high travel speed is selected for depositing sub-volume one, two, and four while a relatively low travel speed is selected for a more stable horizontal deposition. According to the optimal build directions and deposition sequence, the vertical wall one and two were built first while the torch angle was maintained vertically. However, as illustrated in the Fig.6.14(b), the wall one was initially built to the vertical height of the wall three and the wall two was built to a little bit lower height than that for the wall one in order to give enough space for the welding torch when depositing the wall three. For the same accessibility reason, the wall three was not built to its full size, as shown in Fig.6.14(c). In addition, since the electron flow tends to the closer metal conducts electricity in welding. To avoid electron flow transferring through the wrong location and maintain a stable welding arc, it was required to keep alternating deposition between horizontal and vertical wall and the torch angle kept alternating between vertical and horizontal directions as well, as shown in Fig.6.14(b) and Fig.6.12(c). Subsequently, the last bead was deposited with the torch rotated to 45° for a good connection between wall two and three, as show in Fig.6.14(d). Finally, the wall four and the rest of the wall one and two were fabricated, the successful creation of the enclosed shape is shown in Fig.6.14(c). The detailed information of the experiments is provided in Table 6.2.

Table 6. 3 The comparation between conventional WAAM and proposed strategy.

Part No.	Time (s)	Path length (m)	Mass (kg)	Material cost (AUD)
1	1575	5.25	0.48	13.69
2	1575	5.25	0.48	13.69
3	1260	2.1	0.13	3.65
4	297	0.99	0.09	2.58
Support	5100	17	1.56	44.34
Total (proposed strategy)	4707	13.59	1.18	33.61
Total (conventional strategy)	9807	30.59	2.74	77.95
Reduction	52%	56%	57%	57%

Table 6.3 lists the experimental results of multi-directional WAAM in comparison with conventional WAAM. As shown in Fig.6.13(a), extra supporting structure is required for fabricating the part with overhangs by conventional WAAM, resulting in additional manufacturing time and cost (the cost is calculated based on the price of BOC 4043 Aluminum MIG Wire, BOC Ltd, Australia). The production time and cost of the supporting structure are calculated based on its 3D model, the extra built for supporting structure costs more than the part itself. It can be seen that reductions of 52%, 57%, and 57% in manufacturing time, material use, and material cost were achieved through using the proposed multi-directional deposition strategy. In addition, it needs to be mentioned that all data summarized in Table 6.4 is calculated based on the deposition process only, without considering the post-machining process required for removing the supporting structure in conventional WAAM process. Thereby, the actual efficiency of the proposed strategy is higher.

In addition, the provided case study poses significant challenges for the traditional WAAM process. For positional WAAM of complex structures, some suggestions have been summarized for optimum results:

1) Due to the influence of downward gravitational force, the process parameters of multi-directional WAAM is limited compared to WAAM in a flat position. For positional deposition, it is suggested that relatively low power in combination with low

WFS and TS are employed for better welds whilst a relative higher WFS and TS can be used for a higher productivity.

2) The surface tension force is major holding force in multi-directional WAAM process. According to (6.9), the surface tension coefficient can be expressed as [32],

$$\gamma = \gamma_m^0 - A_s(T - T_m) \tag{6.9}$$

where γ_m^0 is the surface tension coefficient of pure metal at the melting point which should be constant for filler material. A_s is the negative of $\partial\gamma/\partial T$ for pure metal which is also considered as a constant when the temperature is much above the melting point. T_m is the melting point of filler material. Besides, the temperature variation which can be suppressed by optimal deposition process control strategy. γ_m^0 is another fact that affects the surface tension force, it is the inherent character of the filler material, so we named it inherent surface tension (IST) in this study. For example, Table 6.4 provides surface tension values of several pure metals in the liquid state at the melting temperature [135]. It reveals that the IST is different for various metallic materials. The larger IST can provide a more stable deposition process with a relative high material deposition ratio.

Table 6. 4 surface tension values for pure metals in the liquid state at the melting temperature.

Metal	Al	Be	Fe	Ti	Re
Temperature (K)	870±10	1760±40	1730±40	1890±40	3270±80
Liquid state surface tension (mJ/m^2)	914	1390	1872	1650	2700

6.7 Chapter summary

This chapter presents an innovative multi-directional WAAM strategy for fabricating complex metal components without supporting structures. Compared to conventional WAAM process, the proposed multi-directional WAAM process would significantly reduce manufacturing time and cost. In this study, the overall process planning algorithm for multi-directional WAAM system from CAD model inputs to final near-net shape products is firstly introduced. Three critical parts of the process are explained and summarized here:

1) Positional bead modelling. The parabola model is used in multi-directional WAAM process. The optimum welding parameters corresponding to the desired bead geometry can be obtained using the developed parabola bead model.

2) Multi-direction slicing strategy. A multi-direction slicing strategy is described step by step through a 3D model of a bearing seat. In the slicing process, a complex input CAD model is decomposed into a set of sub-volumes along the corresponding optimal build directions. Each of the sub-volumes is therefore sliced along its optimal build direction.

3) Deposition process optimization. CMT is selected as welding machine for the positional WAAM due to its short arc transfer mode and low heat input. A relatively

low WFS and TS are recommended for preventing sagged weld bead. A collision free robot motion is achieved through the presented robot code generation module.

The process planning algorithm has been validated to be effective through fabricating the metallic part with complex geometry. The case study also shows a great reduction of material usage compared to traditional WAAM process. The better buy-to-fly ratio makes multi-directional WAAM ideal for industrial using expensive metallic materials, such as titanium alloys from aerospace industrial.

Chapter 7

Summary and future work

7.1 Summary

This study initially carried out the novel conception of true 3D printing which uses the proposed multi-directional WAAM process. Firstly, the forming mechanism of positional deposits is initially investigated to develop a stable deposition process. The effects of the main process parameters on positional deposition were studied. Secondly, the mechanism of humping formation was analyzed for positional deposition using GMAW. It was found that the backward metal flow under the effect of gravity is responsible for the sagged humps in the positional deposition. Based on this, a series of guidelines are summarized to assist the practical use of multi-directional WAAM. Thirdly, a path planning algorithm for multi-directional WAAM was developed. Then, the overall process planning algorithm for multi-directional WAAM system from CAD model inputs to final near-net shape products was firstly carried out for practical industrial use. Finally, a number of parts was fabricated to validate the proposed method and the results showed a great reduction of material usage and manufacturing time compared to traditional WAAM process.

7.2 Future work

This study has made progress in successfully carrying out the concept of ture 3D printing and realizing in by developing the multi-directional WAAM process. As it is still at its nascent stage, the further study on Research and development of multi-directional WAAM process were recommended and summarized below.

1) The optimization of the practical multi-directional WAAM system.

The multi-dictional WAAM system has been initially carried out in this study, however, it needs to be kept improving to adopt the manufacturing industrial requirements. To enhance the current system, more samples with different geometrical features are expected to be fabricated. In this process, imperfections of the system can be found and improved. Thus, the update of the software is priority for the widely use of multi-directional WAAM system.

2) Process control and monitoring system

Generally, the control and monitoring modules are important for most of automated manufacturing systems. For multi-directional WAAM, the welding process has been demonstrated to be sensitive as the process varies, which may affect the process stability and thereby quality of the final products. An on-line monitoring and control system is helpful to improve the system performance, by correcting the process errors at onset of the deposition process.

3) Investigation of material quality

The multi-directional WAAM is considered as an interdisciplinary process, material science is very important for the future development of it. For example, with a high deposition rate, the heat input of the WAAM is relatively high which comes up with residual stresses and distortion of final products. Thus, the suppression of residual stresses and distortion of the metallic components is critical for widely use of the proposed method. Currently, many studies focused on improving the material performance during WAAM process [129, 136, 137]. However, the martial properties of the metallic parts made by the proposed multi-directional WAAM method still lacks investigation. Significant effects should be paid on how material property in influenced by the process patterns, the welding setups and process variables to identify the optimal strategy for improving the material properties of the fabricated parts.

4) Investigation on molten pool behavior in positional deposition

As stated in this study, the molten pool is unstable in the multi-directional deposition due to downward flow of the molten metal, induced by the force of gravity. Thus, the improvement of molten pool behavior is beneficial for forming weld beads without defects. In chapter 4, to avoid humped weld beads, the molten pool behavior was investigated experimentally to improve the molten pool behavior. More research attention may be paid on improving molten pool behavior by applying the simulation method investigate the thermal behavior of the molten pool. Taking advantages of characteristics the molten pool, more guidelines maybe given to optimize process parameters and welding setups to improve the proposed system performance.

Publication

This section lists the publications of Lei Yuan as first author, corresponding author, and other authorship. Note that only publications during the PhD study are presented in this section.

First author

[1] **Lei Yuan**, Zengxi Pan, Donghong Ding Ziping Yu, Stephen van Duin, Huijun, Li, Weihua Li, John Norrish. Fabrication of metallic parts with overhanging structures using the robotic wire arc additive manufacturing. *Journal of Manufacturing Processes*, (in press). – from **Chapter 3**.

[2] **Lei Yuan,** Zengxi Pan, Donghong Ding, Fengyang He, Stephen van Duin, Huijun, Li, Weihua Li. Investigation of humping phenomenon for the multi-directional robotic wire and arc additive manufacturing, Robotics and Computer-Integrated Manufacturing, 63 (2020) 251-263. – from **Chapter 4**.

[3] **Lei Yuan,** Zengxi Pan**,** Joseph Polden**,** Donghong Ding**,** Stephen van Duin. Integration of a multi-directional wire arc additive manufacturing system with an automated process planning algorithm. Journal of Industrial Information Integration. – from **Chapter 5**.

[4] **Lei Yuan**, Donghong Ding, Zengxi Pan, Ziping Yu, Bintao Wu, Stephen van Duin, Huijun Li, Weihua Li, Application of Multidirectional Robotic Wire Arc Additive Manufacturing Process for the Fabrication of Complex Metallic Parts, IEEE Transactions on Industrial Informatics, Industrial Informatics, IEEE Transactions on, IEEE Trans. Ind. Inf., 16 (2020) 454-464.. -**from Chapter 6**.

Corresponding author

[5] Donghong Ding, Fengyang He, **Lei Yuan**, Zengxi Pan, Lei Wang, Montserrate Ros. First steps towards an intelligent wire and arc additive manufacturing: an automatic bead modelling system using machine learning, Journal of Industrial Information Integration. from **Chapter 6**.

[6] Junyi Cui, **Lei Yuan**, Philip Commins, Fengyang He, Jun Wang, Zengxi Pan. A new wire and arc additive manufacturing process for metal block structure parts based on mixed heat input, The International Journal of Advanced Manufacturing Technology.

Other authorship

[7] Ziping Yu, **Lei Yuan**, Fengyang. He, Donghong. Ding, Joseph Polden and Zengxi Pan, "The Strategy for Fabricating Wire-Structure Parts Using Robotic Skeleton Arc Additive Manufacturing," 2019 IEEE 9th Annual International Conference on CYBER

Technology in Automation, Control, and Intelligent Systems (CYBER), Suzhou, China, 2019, pp. 119-124.

Reference

[1] E. Sachs, M. Cima, P. Williams, D. Brancazio, J. Cornie, Three dimensional printing: rapid tooling and prototypes directly from a CAD model, Journal of Engineering for Industry, 114 (1992) 481-488.

[2] G. Posch, K. Chladil, H. Chladil, Material properties of CMT—metal additive manufactured duplex stainless steel blade-like geometries, Welding in the World, 61 (2017) 873-882.

[3] J. González, I. Rodríguez, J. Prado-Cerqueira, J. Diéguez, A. Pereira, Additive manufacturing with GMAW welding and CMT technology, Procedia Manufacturing, 13 (2017) 840-847.

[4] T. Wohlers, T. Gornet, History of additive manufacturing, Wohlers report, 24 (2014) 118.

[5] P. Almeida, S. Williams, Innovative process model of Ti–6Al–4V additive layer manufacturing using cold metal transfer (CMT), in: Proceedings of the twenty-first annual international solid freeform fabrication symposium, University of Texas at Austin, Austin, TX, USA, 2010.

[6] D. Clark, M. Bache, M.T. Whittaker, Shaped metal deposition of a nickel alloy for aero engine applications, journal of materials processing technology, 203 (2008) 439-448.

[7] D. Ding, Z. Pan, D. Cuiuri, H. Li, A multi-bead overlapping model for robotic wire and arc additive manufacturing (WAAM), Robotics and Computer-Integrated Manufacturing, 31 (2015) 101-110.

[8] D. Ding, Z. Pan, D. Cuiuri, H. Li, Wire-feed additive manufacturing of metal components: technologies, developments and future interests, The International Journal of Advanced Manufacturing Technology, 81 (2015) 465-481.

[9] E. Brandl, V. Michailov, B. Viehweger, C. Leyens, Deposition of Ti–6Al–4V using laser and wire, part I: Microstructural properties of single beads, Surface and Coatings Technology, 206 (2011) 1120-1129.

[10] Y. Zhang, Z. Wei, L. Shi, M. Xi, Characterization of laser powder deposited Ti–TiC composites and functional gradient materials, journal of materials processing technology, 206 (2008) 438-444.

[11] D.-H. Ding, Z.-X. Pan, C. Dominic, H.-J. Li, Process planning strategy for wire and arc additive manufacturing, in: Robotic Welding, Intelligence and Automation, Springer, 2015, pp. 437-450.

[12] S. Suryakumar, K. Karunakaran, A. Bernard, U. Chandrasekhar, N. Raghavender, D. Sharma, Weld bead modeling and process optimization in hybrid layered manufacturing, Computer-Aided Design, 43 (2011) 331-344.

[13] B. Cong, J. Ding, S. Williams, Effect of arc mode in cold metal transfer process on porosity of additively manufactured Al-6.3% Cu alloy, The International Journal of Advanced Manufacturing Technology, 76 (2015) 1593-1606.

[14] S.W. Williams, F. Martina, A.C. Addison, J. Ding, G. Pardal, P. Colegrove, Wire+ arc additive manufacturing, Materials Science and Technology, 32 (2016) 641-647.

[15] J. Jiang, J. Stringer, X. Xu, R.Y. Zhong, Investigation of printable threshold overhang angle in extrusion-based additive manufacturing for reducing support waste, International

Journal of Computer Integrated Manufacturing, (2018) 1-9.

[16] J.S. Panchagnula, S. Simhambhatla, Inclined slicing and weld-deposition for additive manufacturing of metallic objects with large overhangs using higher order kinematics, Virtual and Physical Prototyping, 11 (2016) 99-108.

[17] J. Jiang, X. Xu, J. Stringer, Support Structures for Additive Manufacturing: A Review, Journal of Manufacturing and Materials Processing, 2 (2018) 64.

[18] Y. Yang, J. Fuh, H. Loh, Y. Wong, Multi-orientational deposition to minimize support in the layered manufacturing process, Journal of manufacturing systems, 22 (2003) 116.

[19] P. Singh, D. Dutta, Multi-direction slicing for layered manufacturing, Journal of Computing and Information Science in Engineering, 1 (2001) 129-142.

[20] S. Allen, D. Dutta, Wall thickness control in layered manufacturing for surfaces with closed slices, Computational Geometry, 10 (1998) 223-238.

[21] J. Ding, P. Colegrove, J. Mehnen, S. Ganguly, P.M. Sequeira Almeida, F. Wang, S. Williams, Thermo-mechanical analysis of Wire and Arc Additive Layer Manufacturing process on large multi-layer parts, Computational Materials Science, 50 (2011) 3315-3322.

[22] P. Dickens, M. Pridham, R. Cobb, I. Gibson, G. Dixon, Rapid prototyping using 3-D welding, in, DTIC Document, 1992.

[23] J. Spencer, P. Dickens, C. Wykes, Rapid prototyping of metal parts by three-dimensional welding, Proceedings of the Institution of Mechanical Engineers, Part B: Journal of Engineering Manufacture, 212 (1998) 175-182.

[24] J. Norrish, Advanced Welding Processes: Technologies and Process Control (Woodhead Publishing in Materials), Woodhead Publishing, 2006.

[25] B. Wu, Quality improvement in wire arc additive manufacturing, School of Mechanical, Materials, Mechatronic and Biomedical Engineering, 2018.

[26] F. Liou, K. Slattery, M. Kinsella, J. Newkirk, H.-N. Chou, R. Landers, Applications of a hybrid manufacturing process for fabrication of metallic structures, Rapid Prototyping Journal, 13 (2007) 236-244.

[27] Y. Ding, R. Dwivedi, R. Kovacevic, Process planning for 8-axis robotized laser-based direct metal deposition system: a case on building revolved part, Robotics and Computer-Integrated Manufacturing, 44 (2017) 67-76.

[28] J.S. Panchagnula, S. Simhambhatla, Manufacture of complex thin-walled metallic objects using weld-deposition based additive manufacturing, Robotics and Computer-Integrated Manufacturing, 49 (2018) 194-203.

[29] D. Ding, Z. Pan, D. Cuiuri, H. Li, N. Larkin, S. Van Duin, Automatic multi-direction slicing algorithms for wire based additive manufacturing, Robotics and Computer-Integrated Manufacturing, 37 (2016) 139-150.

[30] J. Ruan, T.E. Sparks, A. Panackal, F.W. Liou, K. Eiamsa-Ard, K. Slattery, H.-N. Chou, M. Kinsella, Automated slicing for a multiaxis metal deposition system, Journal of manufacturing science and engineering, 129 (2007) 303-310.

[31] R. Dwivedi, R. Kovacevic, Process planning for multi-directional laser-based direct metal deposition, Proceedings of the Institution of Mechanical Engineers, Part C: Journal of Mechanical Engineering Science, 219 (2005) 695-707.

[32] J. Xiong, Y. Lei, H. Chen, G. Zhang, Fabrication of inclined thin-walled parts in multi-layer single-pass GMAW-based additive manufacturing with flat position deposition,

Journal of Materials Processing Technology, 240 (2017) 397-403.

[33] Y. Li, X. Huang, I. Horváth, G. Zhang, GMAW-based additive manufacturing of inclined multi-layer multi-bead parts with flat-position deposition, Journal of Materials Processing Technology, 262 (2018) 359-371.

[34] P. Kazanas, P. Deherkar, P. Almeida, H. Lockett, S. Williams, Fabrication of geometrical features using wire and arc additive manufacture, Proceedings of the Institution of Mechanical Engineers, Part B: Journal of Engineering Manufacture, 226 (2012) 1042-1051.

[35] D. Ding, Z. Pan, D. Cuiuri, H. Li, A practical path planning methodology for wire and arc additive manufacturing of thin-walled structures, Robotics and Computer-Integrated Manufacturing, 34 (2015) 8-19.

[36] D. Ding, Z. Pan, D. Cuiuri, H. Li, N. Larkin, Adaptive path planning for wire-feed additive manufacturing using medial axis transformation, Journal of Cleaner Production, 133 (2016) 942-952.

[37] Y. Zhang, Y. Chen, P. Li, A.T. Male, Weld deposition-based rapid prototyping: a preliminary study, Journal of Materials Processing Technology, 135 (2003) 347-357.

[38] S. Sun, H. Chiang, M. Lee, Adaptive direct slicing of a commercial CAD model for use in rapid prototyping, The International Journal of Advanced Manufacturing Technology, 34 (2007) 689-701.

[39] D. Ding, Z.S. Pan, D. Cuiuri, H. Li, A tool-path generation strategy for wire and arc additive manufacturing, The international journal of advanced manufacturing technology, 73 (2014) 173-183.

[40] M.R. Dunlavey, Efficient polygon-filling algorithms for raster displays, ACM

Transactions on Graphics (TOG), 2 (1983) 264-273.

[41] S.C. Park, B.K. Choi, Tool-path planning for direction-parallel area milling, Computer-Aided Design, 32 (2000) 17-25.

[42] V. Rajan, V. Srinivasan, K.A. Tarabanis, The optimal zigzag direction for filling a two-dimensional region, Rapid Prototyping Journal, (2001).

[43] H. Wang, P. Jang, J.A. Stori, A metric-based approach to two-dimensional (2D) tool-path optimization for high-speed machining, J. Manuf. Sci. Eng., 127 (2005) 33-48.

[44] F. Ren, Y. Sun, D. Guo, Combined reparameterization-based spiral toolpath generation for five-axis sculptured surface machining, The international journal of advanced manufacturing technology, 40 (2009) 760-768.

[45] M. Bertoldi, M. Yardimci, C. Pistor, S. Guceri, Domain decomposition and space filling curves in toolpath planning and generation, in: 1998 International Solid Freeform Fabrication Symposium, 1998.

[46] T. Wasser, A.D. Jayal, C. Pistor, Implementation and evaluation of novel buildstyles in fused deposition modeling (FDM), in: 1999 International Solid Freeform Fabrication Symposium, 1999.

[47] R. Dwivedi, R. Kovacevic, Automated torch path planning using polygon subdivision for solid freeform fabrication based on welding, Journal of Manufacturing Systems, 23 (2004) 278-291.

[48] R. Farouki, T. Koenig, K. Tarabanis, J. Korein, J. Batchelder, Path planning with offset curves for layered fabrication processes, Journal of Manufacturing Systems, 14 (1995) 355-368.

[49] Y. Yang, H.T. Loh, J. Fuh, Y. Wang, Equidistant path generation for improving scanning efficiency in layered manufacturing, Rapid Prototyping Journal, (2002).

[50] H. Li, Z. Dong, G.W. Vickers, Optimal toolpath pattern identification for single island, sculptured part rough machining using fuzzy pattern analysis, Computer-Aided Design, 26 (1994) 787-795.

[51] G. Jin, W.D. Li, L. Gao, An adaptive process planning approach of rapid prototyping and manufacturing, Robotics and Computer-Integrated Manufacturing, 29 (2013) 23-38.

[52] A. Shirali, K. Mills, The effect of welding parameters on penetration in GTA welds, WELDING JOURNAL-NEW YORK-, 72 (1993) 347-s.

[53] S. Radel, A. Diourte, F. Soulié, O. Company, C. Bordreuil, Skeleton arc additive manufacturing with closed loop control, Additive Manufacturing, (2019).

[54] W.H. Hager, Wilfrid noel bond and the bond number, Journal of Hydraulic Research, 50 (2012) 3-9.

[55] T. Nguyen, D. Weckman, D. Johnson, H. Kerr, High speed fusion weld bead defects, Science and Technology of Welding and Joining, 11 (2006) 618-633.

[56] T. DebRoy, S.A. David, J.N. DuPont, T. Koseki, H.K. Bhadeshia, Trends in Welding Research 2012: Proceedings of the 9th International Conference, ASM International, 2013.

[57] B. Bradstreet, Effect of surface tension and metal flow on weld bead formation, Welding journal, 47 (1968) 314s-322s.

[58] P.F. Mendez, T.W. Eagar, Penetration and defect formation in high-current arc welding, Welding Journal, 82 (2003) 296.

[59] P.F. Mendez, K.L. Niece, T.W. Eagar, Humping formation in high current GTA welding, in:

Proceedings of the International Conference on Joining of Advanced and Specialty Materials II, 2000, pp. 151-158.

[60] W. Savage, E. Nippes, K. Agusa, Effect of arc force on defect formation in GTA welding, Welding journal, 58 (1979) 212.

[61] A. Kumar, T. DebRoy, Toward a unified model to prevent humping defects in gas tungsten arc welding, WELDING JOURNAL-NEW YORK-, 85 (2006) 292.

[62] J. Xie, Dual beam laser welding, Welding journal, 81 (2002) 223s-230s.

[63] Y. Ai, P. Jiang, C. Wang, G. Mi, S. Geng, W. Liu, C. Han, Investigation of the humping formation in the high power and high speed laser welding, Optics and Lasers in Engineering, 107 (2018) 102-111.

[64] M. Cai, C. Wu, X. Gao, Research on Humping Tendency in High Speed Laser Welding of SUS304 Austenitic Stainless Steel, in: 2017 International Conference on Material Science, Energy and Environmental Engineering (MSEEE 2017), Atlantis Press, 2017.

[65] C.E. Albright, S. Chiang, High-Speed Laser Welding Discontinuities, Journal of Laser Applications, 1 (1988) 18-24.

[66] S. Tsukamoto, H. Irie, M. Inagaki, T. Hashimoto, Effect of beam current on humping bead formation in electron beam welding, Trans. Natl. Res. Inst. Met.(Jpn.), 26 (1984) 133-140.

[67] M. Tomie, N. Abe, Y. Arata, Tandem Electron Beam Welding (Report IX): High Speed Tandem Electron Beam Welding (Physics, Process, Instrument & Measurement), Transactions of JWRI, 18 (1989) 175-180.

[68] S. Sakaguchi, T. Yamaguchi, Y. Nakano, Behaviour of molten metal and optimum welding conditions for high heat input submerged-arc welding with flux containing iron powder,

Welding international, 10 (1996) 282-287.

[69] A. Adebayo, J. Mehnen, X. Tonnellier, Limiting travel speed in additive layer manufacturing, (2013).

[70] L. Wang, C. Wu, J. Gao, Suppression of humping bead in high speed GMAW with external magnetic field, Science and Technology of Welding and Joining, 21 (2016) 131-139.

[71] L. Wang, C. Wu, J. Chen, J. Gao, Influence of the external magnetic field on fluid flow, temperature profile and humping bead in high speed gas metal arc welding, International Journal of Heat and Mass Transfer, 116 (2018) 1282-1291.

[72] L. Wang, J. Chen, C. Wu, J. Gao, Backward flowing molten metal in weld pool and its influence on humping bead in high-speed GMAW, Journal of Materials Processing Technology, 237 (2016) 342-350.

[73] J.W.S.B. Rayleigh, The theory of sound, Macmillan, 1896.

[74] U. Gratzke, P. Kapadia, J. Dowden, J. Kroos, G. Simon, Theoretical approach to the humping phenomenon in welding processes, Journal of Physics D: Applied Physics, 25 (1992) 1640.

[75] B. Paton, S. BG, M. SL, CERTAIN SPECIAL FEATURES OF FORMATION OF WELDS MADE AT HIGH SPEEDS, Automatic Welding USSR, 24 (1971) 1-&.

[76] T. Yamamoto, W. Shimada, A study on bead formation in high speed TIG arc welding at low gas pressure, in: Proceedings of the Advanced Welding Technology, The Second International Symposium of the Japan Welding Society on Advanced Welding Technology, 1975, pp. 321-326.

[77] W. Shimada, S. Hoshinouchi, Study of bead formation by low pressure TIG arc and

prevention of under-cut bead, Journal of the Japan Welding Society, 51 (1982) 280-286.

[78] T. Nguyen, D. Weckman, D. Johnson, H. Kerr, The humping phenomenon during high speed gas metal arc welding, Science and Technology of Welding and Joining, 10 (2005) 447-459.

[79] D. Wu, X. Hua, D. Ye, F. Li, Understanding of humping formation and suppression mechanisms using the numerical simulation, International Journal of Heat and Mass Transfer, 104 (2017) 634-643.

[80] G. Xu, Q. Cao, Q. Hu, W. Zhang, P. Liu, B. Du, Modelling of bead hump formation in high speed gas metal arc welding, Science and Technology of Welding and Joining, 21 (2016) 700-710.

[81] J. Chen, C.-S. Wu, Numerical analysis of forming mechanism of hump bead in high speed GMAW, Welding in the World, 54 (2010) R286-R291.

[82] M.H. Cho, D.F. Farson, Understanding bead hump formation in gas metal arc welding using a numerical simulation, Metallurgical and materials transactions B, 38 (2007) 305-319.

[83] J. Chen, C. Wu, Effect of droplet heat content distribution on humping formation in high speed GMAW, Acta Metallurgica Sinica(English Letters), 24 (2011) 457-465.

[84] Z. Pan, J. Polden, N. Larkin, S. Van Duin, J. Norrish, Recent progress on programming methods for industrial robots, in: ISR 2010 (41st International Symposium on Robotics) and ROBOTIK 2010 (6th German Conference on Robotics), VDE, 2010, pp. 1-8.

[85] X. Wang, L. Xue, Y. Yan, X. Gu, Welding robot collision-free path optimization, Applied Sciences, 7 (2017) 89.

[86] S.N. Gai, R. Sun, S.J. Chen, S. Ji, 6-DOF Robotic Obstacle Avoidance Path Planning

Based on Artificial Potential Field Method, in: 2019 16th International Conference on Ubiquitous Robots (UR), IEEE, 2019, pp. 165-168.

[87] B. Faverjon, Obstacle avoidance using an octree in the configuration space of a manipulator, in: Proceedings. 1984 IEEE International Conference on Robotics and Automation, IEEE, 1984, pp. 504-512.

[88] N. Larkin, A. Short, Z. Pan, S. van Duin, Automatic program generation for welding robots from CAD, in: 2016 IEEE International Conference on Advanced Intelligent Mechatronics (AIM), IEEE, 2016, pp. 560-565.

[89] N. Larkin, A. Short, Z. Pan, S. Van Duin, Task Space Motion Planning Decomposition, in: 2018 IEEE International Conference on Robotics and Automation (ICRA), IEEE, 2018, pp. 1688-1694.

[90] Y. Wang, D. Mulvaney, I. Sillitoe, Genetic-based mobile robot path planning using vertex heuristics, in: 2006 IEEE Conference on Cybernetics and Intelligent Systems, IEEE, 2006, pp. 1-6.

[91] L. Lei, Q. Shiru, Path planning for unmanned air vehicles using an improved artificial bee colony algorithm, in: Proceedings of the 31st Chinese Control Conference, IEEE, 2012, pp. 2486-2491.

[92] H. Randhawa, P. Ghosh, S. Gupta, Geometrical Characteristics of Pulsed Current Positional GMA Weld, ISIJ international, 38 (1998) 276-284.

[93] P.K. Ghosh, S.R. Gupta, H.S. Randhawa, Characteristics of a pulsed-current, vertical-up gas metal arc weld in steel, Metallurgical and Materials Transactions A, 31 (2000) 2247-2259.

[94] D.W. Cho, S.J. Na, M.H. Cho, J.S. Lee, A study on V-groove GMAW for various welding

positions, Journal of Materials Processing Tech., 213 (2013) 1640-1652.

[95] X. Guoxiang, L. Lin, W. Jiayou, Z. Jie, L. Pengfei, Study of weld formation in swing arc narrow gap vertical GMA welding by numerical modeling and experiment, International Journal of Advanced Manufacturing Technology, 96 (2018) 1905-1917.

[96] N. Guo, M. Wang, W. Guo, J. Yu, J. Feng, Study on forming mechanism of appearance defects in rotating arc narrow gap horizontal GMAW, The International Journal of Advanced Manufacturing Technology, 75 (2014) 15-20.

[97] N. Guo, M.R. Wang, W. Guo, J.B. Yu, J.C. Feng, Effect of rotating arc process on molten pool control in horizontal welding, Science and Technology of Welding and Joining, 19 (2014) 385-391.

[98] X.Y. Cai, S.B. Lin, C.L. Fan, C.L. Yang, W. Zhang, Y.W. Wang, Molten pool behaviour and weld forming mechanism of tandem narrow gap vertical GMAW, Science and Technology of Welding and Joining, 21 (2016) 124-130.

[99] E. Soderstrom, P. Mendez, Humping mechanisms present in high speed welding, Science and Technology of Welding and joining, 11 (2006) 572-579.

[100] M. Motta, A.G. Demir, B. Previtali, High-speed imaging and process characterization of coaxial laser metal wire deposition, Additive Manufacturing, (2018).

[101] H. Randhawa, Investigation into positional welding of structural steel using pulse current GMAW process, (1999).

[102] R. Eötvös, Ueber den Zusammenhang der Oberflächenspannung der Flüssigkeiten mit ihrem Molecularvolumen, Annalen der Physik, 263 (1886) 448-459.

[103] M. Webster, definitions-surface tension report a problem.

[104] A. Magnitis, K. Kennedy, J. Zajic, D. Gerson, Surface tension by the ring method (Du Nouy method), Dev. Ind. Micrbiol, 20 (1979) 623-630.

[105] W. Moore, Physical Chemistry 3rd Ed Prentice-Hall Inc, New York, (1962).

[106] Z. Li, K. Mukai, M. Zeze, K. Mills, Determination of the surface tension of liquid stainless steel, Journal of materials science, 40 (2005) 2191-2195.

[107] J. Norrish, D. Cuiuri, The controlled short circuit GMAW process: a tutorial, Journal of Manufacturing Processes, 16 (2014) 86-92.

[108] L. Yuan, S. Sun, Z. Pan, D. Ding, O. Gienke, W. Li, Mode coupling chatter suppression for robotic machining using semi-active magnetorheological elastomers absorber, Mechanical Systems and Signal Processing, 117 (2019) 221-237.

[109] A. Gomez Ortega, L. Corona Galvan, F. Deschaux-Beaume, B. Mezrag, S. Rouquette, Effect of process parameters on the quality of aluminium alloy Al5Si deposits in wire and arc additive manufacturing using a cold metal transfer process, Science and Technology of Welding and Joining, (2017) 1-17.

[110] B. Cong, R. Ouyang, B. Qi, J. Ding, Influence of cold metal transfer process and its heat input on weld bead geometry and porosity of aluminum-copper alloy welds, Rare Metal Materials and Engineering, 45 (2016) 606-611.

[111] J. Xiong, Z. Yin, W. Zhang, Forming appearance control of arc striking and extinguishing area in multi-layer single-pass GMAW-based additive manufacturing, The International Journal of Advanced Manufacturing Technology, 87 (2016) 579-586.

[112] C. Zhang, Y. Li, M. Gao, X. Zeng, Wire arc additive manufacturing of Al-6Mg alloy using variable polarity cold metal transfer arc as power source, Materials Science and

Engineering: A, 711 (2018) 415-423.

[113] M.R. Ahsan, M. Cheepu, R. Ashiri, T.-H. Kim, C. Jeong, Y.-D. Park, Mechanisms of weld pool flow and slag formation location in cold metal transfer (CMT) gas metal arc welding (GMAW), Welding in the World, 61 (2017) 1275-1285.

[114] P. Sahoo, T. DebRoy, M. McNallan, Surface tension of binary metal—surface active solute systems under conditions relevant to welding metallurgy, Metallurgical transactions B, 19 (1988) 483-491.

[115] S. Kou, C. Limmaneevichitr, P. Wei, Oscillatory Marangoni flow: a fundamental study by conduction-mode laser spot welding, Weld. J, 90 (2011) 229-240.

[116] C.S. Wu, Welding thermal processes and weld pool behaviors, CRC Press, 2011.

[117] P. Berger, H. Hügel, A. Hess, R. Weber, T. Graf, Understanding of humping based on conservation of volume flow, Physics Procedia, 12 (2011) 232-240.

[118] S. Selvi, A. Vishvaksenan, E. Rajasekar, Cold metal transfer (CMT) technology-An overview, Defence Technology, (2017).

[119] M. Cai, C. Wu, X. Gao, The Influence of Arc Length Correction on Welding in CMT Welding, in: IOP Conference Series: Earth and Environmental Science, IOP Publishing, 2018, pp. 042106.

[120] Fronius, Fronius CMT 4000 Advanced Manuals, in, 2012.

[121] Z. Pan, J. Polden, N. Larkin, S. van Duin, J. Norrish, Automated offline programming for robotic welding system with high degree of freedoms, in: Advances in Computer, Communication, Control and Automation, Springer, 2011, pp. 685-692.

[122] L. Yuan, D. Ding, Z. Pan, Z. Yu, B. Wu, S.v. Duin, H. Li, W. Li, Application of

Multi-directional Robotic Wire Arc Additive Manufacturing Process for The Fabrication of Complex Metallic Parts, IEEE Transactions on Industrial Informatics, (2019) 1-1.

[123] D. Hsu, L.E. Kavraki, J.-C. Latombe, R. Motwani, S. Sorkin, On finding narrow passages with probabilistic roadmap planners, in: Robotics: the algorithmic perspective: 1998 workshop on the algorithmic foundations of robotics, 1998, pp. 141-154.

[124] Z. Hou, S. Ma, Q. Zeng, A. Li, Kinematics analysis and self-collision detection of Truss type multi-robot cooperative welding platform, Procedia CIRP, 81 (2019) 488-493.

[125] N. Basit, Tool holders for robotic systems having collision detection, in, Google Patents, 2018.

[126] J. Xiong, G. Zhang, J. Hu, L. Wu, Bead geometry prediction for robotic GMAW-based rapid manufacturing through a neural network and a second-order regression analysis, Journal of Intelligent Manufacturing, 25 (2014) 157-163.

[127] R. Urbanic, S. Saqib, K. Aggarwal, Using predictive modeling and classification methods for single and overlapping bead laser cladding to understand bead geometry to process parameter relationships, Journal of Manufacturing Science and Engineering, 138 (2016) 051012.

[128] S. Meco, G. Pardal, A. Eder, L. Quintino, Software development for prediction of the weld bead in CMT and pulsed-MAG processes, The International Journal of Advanced Manufacturing Technology, 64 (2013) 171-178.

[129] B. Wu, Z. Pan, D. Ding, D. Cuiuri, H. Li, J. Xu, J. Norrish, A review of the wire arc additive manufacturing of metals: Properties, defects and quality improvement, Journal of Manufacturing Processes, 35 (2018) 127-139.

[130] J. Xiong, G. Zhang, H. Gao, L. Wu, Modeling of bead section profile and overlapping beads with experimental validation for robotic GMAW-based rapid manufacturing, Robotics and Computer-Integrated Manufacturing, 29 (2013) 417-423.

[131] D. Ding, C. Shen, Z. Pan, D. Cuiuri, H. Li, N. Larkin, S. van Duin, Towards an automated robotic arc-welding-based additive manufacturing system from CAD to finished part, Computer-Aided Design, 73 (2016) 66-75.

[132] B. Lowekamp, P. Rheingans, T.S. Yoo, Exploring surface characteristics with interactive Gaussian images: a case study, in: Proceedings of the conference on Visualization'02, IEEE Computer Society, 2002, pp. 553-556.

[133] S. Choi, K. Kwok, A tolerant slicing algorithm for layered manufacturing, Rapid Prototyping Journal, 8 (2002) 161-179.

[134] Z. Yao, K. Gupta, Path planning with general end-effector constraints, Robotics and Autonomous Systems, 55 (2007) 316-327.

[135] V. Kumikov, The measurement of the surface tension of some pure metals in the solid state, Materials science and engineering, 60 (1983) L23-L24.

[136] D. Ding, Z. Pan, S. van Duin, H. Li, C. Shen, Fabricating superior NiAl bronze components through wire arc additive manufacturing, Materials, 9 (2016) 652.

[137] S. Juang, Y. Tarng, Process parameter selection for optimizing the weld pool geometry in the tungsten inert gas welding of stainless steel, Journal of materials processing technology, 122 (2002) 33-37.